Modeling of bearing currents and voltages in inverter-fed electric motors

Elie Kopaly

School of Electrical Engineering

Thesis submitted for examination for the degree of Master of Science in Technology.

Espoo 22.05.2017

Thesis supervisor:

Prof. Anouar Belahcen

Thesis advisor:

M.Sc. Juha Kaksonen

Aalto University
School of Electrical
Engineering

AALTO UNIVERSITY
SCHOOL OF ELECTRICAL ENGINEERING

ABSTRACT OF THE
MASTER'S THESIS

Author: Elie Kopaly

Title: Modeling of bearing currents and voltages in inverter-fed electric motors

Date: 22.05.2017 Language: English Number of pages: 8+79

Department of Electrical Engineering and Automation

Professorship: Computational Electromechanics

Supervisor: Prof. Anouar Belahcen

Advisor: M.Sc. Juha Kaksonen

The possible bearing damages in inverter-fed AC motors are nowadays an important issue in the industrial scope. These motors are known to experience bearing voltages and currents. The root causes for the bearing voltages and currents are common-mode voltages produced by the inverter. However, no cost-effective solution for large AC motors, especially in Azipod ® systems, has been found to mitigate these problematic voltages and currents. The existing solution is to insulate the non-drive end bearing shield, which takes a large amount of space, is expensive and challenging to manufacture. In addition, no high-frequency model of large AC motors has been created for the purpose of the analysis of bearing voltages and currents.

The work presented in this thesis identifies the common factors that lead to these harmful voltages and currents, and from a consideration of these factors, a high-frequency model of the AC motor is created. This model is then adapted to the Azipod system. Simulations are carried out showing the interdependence of different components in the system. In order to complete the simulations, extraction of model parameters that involves analytical calculations and measurements are shown in detail.

The model presented in this work can be connected to an appropriate electric drive in order to predict the bearing voltages and currents with a simulator such as OrCAD. The results of the simulations show that the present mitigation techniques can be simplified, with certain precautions, without increasing the bearing voltages and currents to dangerous levels.

Keywords: high-frequency model, bearing voltage, bearing current, common-mode, voltage-source inverter, bearing shield insulation, parameter extraction, simulation, Azipod

AALTO-YLIOPISTO
SÄHKÖTEKNIIKAN KORKEAKOULU

DIPLOMITYÖN
TIIVISTELMÄ

Tekijä: Elie Kopaly

Työn nimi: Laakerivirtojen ja -jännitteiden mallintaminen taajuusmuuttajaohjatuissa sähkömoottoreissa

Päivämäärä: 22.05.2017 Kieli: Englanti Sivumäärä: 8+79

Sähkötekniikan ja automaation laitos

Professuuri: Laskennallinen Sähkömekaniikka

Työn valvoja: Prof. Anouar Belahcen

Työn ohjaaja: DI Juha Kaksonen

Mahdolliset laakerivauriot taajuusmuuttajasyötetyissä vaihtovirtamoottoreissa ovat merkittävä haaste teollisuudessa. Kyseisten moottorien tiedetään altistuvan laakerijännitteille ja -virroille, joiden on havaittu aiheutuvan taajusmuuttajan tuottamasta yhteismuotoisesta jännitteestä. Toistaiseksi ei ole löydetty kustannustehokasta ratkaisua pienentämään näitä ongelmallisia jännitteitä ja sähkövirtoja suurissa vaihtovirtamoottoreissa, varsinkaan Azipod ® -järjestelmissä. Nykyinen ratkaisu on trustipään laakerikilven eristäminen, mikä vie paljon tilaa ja on kallista sekä haastavaa toteuttaa. Toistaiseksi ei ole kehitetty suurtaajuusmallia isoille vaihtovirtamoottoreille laakerijännitteiden ja –virtojen analysointia varten.

Tässä työssä on esitetty yleiset tunnistetut tekijät, jotka johtavat näihin haitallisiin jännitteisiin ja virtoihin vaihtovirtamoottoreissa. Työssä on luotu nämä tekijät huomioon ottaen suurtaajuusmalli vaihtovirtamoottoreille. Mallia on kehitetty niin, että sitä voidaan käyttää Azipod-järjestelmässä. Simulaatioiden perusteella voidaan osoittaa eri komponenttien keskinäiset riippuvuudet järjestelmässä. Simulaatioiden suorittamiseksi työssä on esitetty yksityiskohtaisesti mallin parametrien ekstraktoiminen, mikä sisältää analyyttista tarkastelua ja mittauksia.

Työssä esitetyn mallin voi yhdistää sopivaan sähkökäyttöön, jolloin laakerijännite ja –virta ovat ennustettavissa piirisimulaattorilla, kuten OrCAD:lla. Työn simuloinnit osoittavat, että nykyisiä käytettyjä laakerivirtojen lieventämistekniikoita voidaan yksinkertaistaa tietyllä varauksella ilman laakerivirtojen ja -jännitteiden nousua vaarallisille tasoille.

Avainsanat: suurtaajuusmalli, laakerijännite, laakerivirta, yhteismuotoinen, jännitelähde invertteri, laakerikilven eristys, parametrien ekstraktoiminen, simulaatio, Azipod

Preface

It was a privilege to carry out the research work for this thesis with the support of ABB Marine on bearing currents and their insulations in Azipod systems. This work was written to fulfill the graduation requirements of the Electrical Engineering Program at the Aalto University. I was engaged in writing and researching from October 2016 until May 2017. No one becomes a bearing current phenomenon expert in such a short time, and it is no exaggeration to state that during this research I have learned the most during my time studying at the university. With the difficulty of this project in mind, I was fortunate enough to have my university professor and supervisors at ABB always available and ready to answer my questions.

To begin with, I would like to thank prof. Anouar Belahcen, who was always willing to support and encourage me throughout this project. I was extremely lucky to have him as my professor for both my Bachelor's and Master's theses. I am also thankful to my supervisor, Juha Kaksonen, who motivated me, challenged me, and answered my queries about the topic. Thank you for your guidance. Additionally, Petri Pellinen, my co-supervisor, deserves a huge thank you. I am grateful to have had the chance to work with such an expert on bearings, who was exceedingly helpful with the work and respectful of my ideas. I would also like to thank Jukka Putaansuu for spending several hours on helping me with the measurements. Additionally, I would like to recognise the effort of Harri Lipponen and prof. Jorma Kyyrä in answering my questions about the drives. In addition, I am grateful to Sami Palokangas, Piia Karjalainen, Petri Mäkikyrö and Kai Karila from ABB Marine whom entrusted me with this project.

I would also like to thank my family Georges, Maarit, Maya, Antoni and Tomi, for supporting me with everything. I owe all my success and hard work to my family. I would also like to thank my friends. My dear friend Tuukka Mattila deserves a huge credit for supporting me throughout my university studies. Last but not least, I want to thank my friend Markus Muurimäki, who introduced me to ABB Marine.

And, finally, thank you reader. You have already read one page. I hope you enjoy the rest.

Otaniemi, 22.05.2017

Elie G. P. Kopaly

Contents

Symbols and abbreviations

Symbols

A	ampere
A_{Hz}	Hertz'ian contact area
C	capacitance
C_{wr}	stator winding-to-rotor capacitance
C_b	bearing capacitance
C_{rs}	rotor-to-frame capacitance
C_{wf}	stator winding-to-frame capacitance
C_{ph}	phase-to-phase capacitance
C_{bNDE1}	non-drive end radial bearing capacitance
C_{bNDE2}	slide thrust bearing capacitance
C_{bDE}	drive-end radial bearing capacitance
C_{ins}	bearing shield insulation capacitance
C_m	mutual capacitance of stator winding one and two
f	frequency
F	farad
g	gram
H	henry
Hz	hertz
i_b	bearing current
kHz	kilohertz
kN	kilonewton
kV	kilovolt
kW	kilowatt
L_c	connectors and internal line conductors inductance
L_s	leakage inductance of stator winding
mA	milliampere
mF	millifarad
mm	millimeter
mm^2	square millimeter
$M\Omega$	megaohm
$m\Omega$	milliohm
MW	megawatt
MHz	megahertz
nF	nanofarad
pF	pikofarad
R_b	bearing resistance
R_g	dissipative loss resistance of stator yoke and frame
s	second
V	volt
VAC	voltage in alternating current
v_b	bearing voltage
V_{ag}	line-to-ground voltage of phase a
V_{bg}	line-to-ground voltage of phase b
V_{cg}	line-to-ground voltage of phase c
V_{com}	common-mode voltage
ϵ_0	vacuum permittivity
ϵ_r	relative permittivity

Operators

$\frac{\mathrm{d}v}{\mathrm{d}t}$	derivative of voltage with respect to time
$\int_a^b f(t)\mathrm{d}t$	definitive integral of function f from a to b with respect to variable t

Abbreviations

AC	alternating current
Azipod	azimuthing electricpodded drive
DC	direct current
DE	drive end
DTC	direct torque control
EDM	electric discharge machining
IGCT	integrated gate-commutated thyristor
NDE	non-drive end
rpm	revolutions per minute
TD	time delay

1 Introduction

For several decades, an increasing number of electric motors have been fed by variable speed drives due to the need for steadily adjustable speed applications that provide high efficiency to the system and a soft start.

Voltage-source inverters with power semiconductors are commonly used for controlling the speed of AC motors. Power losses within the semiconductors are reduced by the high switching frequency of these semiconductor devices. However, high switching frequency leads to a short rise time of the inverter's output voltage leading to high *dv/dt*. Typically, the output of the inverter seen by driven AC motor's terminals consists of common-mode voltages. These voltages with high *dv/dt* are the main reasons for induced bearing currents.

Inverter-fed drive systems are more susceptible to bearing failures than conventional, line-operated drive systems. Bearing failures and the consequent downtime are critical in some applications. The most common reasons for the failures are the inverter-induced bearing currents. If the bearing voltage exceeds the breakdown voltage of the bearing grease, a current will flow through the metallic races of the bearings. Bearing currents can cause electrical fluting which leads to damages on the bearing's surface [1, p. 22]. Bearings are a critical part of electric motors and so, understanding the bearing failures caused by inverters is essential.

Inverter related bearing current failures of AC motors have been the focus of intense research for the last two decades. Many studies, such as done by Erdman, Kerkman, Schlegel and Skibinski in [2], have been devoted to the investigation of AC motor bearing currents and shaft voltages when operated with variable speed drives. Chen and Lipo in [3] have presented the different types of bearing currents in inverter drives. In recent years, much progress has been achieved in minimization or prevention of bearing currents in AC motors, such as those presented in studies [4] and [5].

Capacitances of the drive system come into effect when the AC motor is submitted to common-mode voltages consisting of high frequency components. Due to the big role of the capacitances in this common-mode phenomenon, they are examined extensively in this work. Understanding the nature of bearing currents and the characteristics of bearings provides tools for modeling the phenomena with capacitances that are important at high frequencies. However, no studies have been carried out for large synchronous motors of several megawatts consisting of large bearings, especially the ones used in Azipod ® (Azimuthing electricpodded drive) systems.

The Azipod is a propulsion system built into a rotating pod that is fastened to the outside hull of the ship. Azipod propulsion systems are used in a variety of marine applications such as ice breakers and luxury cruise ships. These Azipod systems consist of high-efficiency synchronous motors that are controlled by adjustable speed drives located onship. The adjustable speed drives use DTC (direct torque control) technology. Previously, the AC motors of Azipod were fed by cycloconverters instead of DTC drives and according to today's knowledge, were not prone to destructive bearing currents. The cycloconverters were changed to DTC drives because these

drives perform better in electric power networks. However, the present solution's synchronous motors are prone to bearing currents caused by the inverters. The existing solution in preventing bearing currents is to insulate the NDE (non-drive end) bearing shield. Moreover, in the NDE side there are shaft brushes ensuring the same potential over the shaft and the thrust bearing. On the other hand, two earthing devices in the DE (drive end) of the motor, located at the shaft, provide the shaft currents a path to earth, thus protecting the bearing from these harmful currents at the propulsion side.

Insulating the NDE bearing shield prevents any destructive currents to flow through the non-drive end bearings. While this approach cancels the bearing currents, it ignores the fact that the insulation requires large space and is challenging to construct. Moreover, the end shield is big and creates logistics challenges to insulate it. In addition, the present solution is expensive, is provided by only a few suppliers and its functionality is not investigated enough, for example, by changing the thickness of the insulation.

The aim of this thesis is to develop an equivalent circuit for the Azipod system and calculate the bearing currents and voltages using a simulation program. Therefore, the obtained model and achieved simulations enable to study the severity of the bearing currents. In addition, simulations are used to examine the role of the insulation with earthing brushes "on" and "off".

The parameters for the equivalent circuit are a combination of calculated and measured values. Calculated values are found with the help of literature and internal support. Some of the measurements, such as input voltages, were done in the assembly line, while the others were carried out on a sailing vessel. Accurate values are inserted in the simulation model in order to acquire the most optimal output addressing the concern. In addition, discussions with bearing, insulation and earthing brush suppliers are carried out in order to investigate alternative solutions on protecting the bearings and minimizing the parasitic effects of the inverter.

Chapter 2 of the thesis presents the Azipod drive system, including the basic components. Chapter 3 describes the physics of bearings and explains the principles underlying the bearing currents. Chapter 4 presents the current bearing insulation. Chapter 5 describes the development of the equivalent circuit that will be simulated and explains how some of the parameters are extracted. Chapter 6 introduces the measurements. Chapter 7 summarizes the simulation results for various scenarios. Finally, Chapter 8 offers a comprehensive summary of the assumptions made in this work and suggests topics for further study.

2 Drive System

This section presents the drive system with its components in general terms. Although the main focus is more in the Azipod itself, this section sets the stage for a more profound examination of the problem, that is presented in the following chapters.

2.1 ACS6000 SD

The drive in question is the ACS6000 SD; it is used for high power applications ranging from 3 to 27 megawatts. The drive's output voltage to the synchronous motor's terminals is up to 3 kV, and covers an output frequency range of 0 to 75 Hz.

The basic configuration of the drive feeding the motor consists of a transformer, a rectifier unit, a DC link and an inverter unit. Depending on the application, the configuration may vary slightly. The Azipod propulsions treated in this work consist of two drives connected in parallel having a common DC link and feeding a synchronous motor that has a double stator winding. Since the motor is synchronous, an excitation unit is added to feed the field windings of the motor from an auxiliary power line. Figure 1 presents the drive system topology.

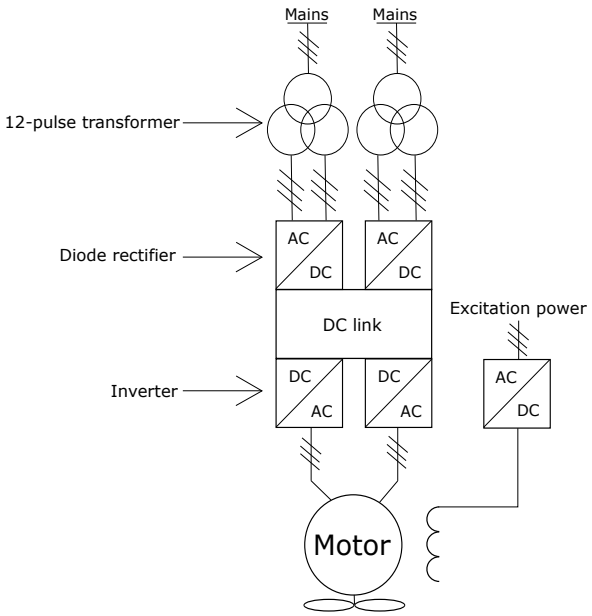

Figure 1: Model of the drive system topology consisting of input transformers, rectifiers, a common DC link, inverters, a synchronous motor and a field winding.

The rectifier and inverter units are of identical design mechanically and electrically. The input transformer's secondary is connected to the rectifier, which then converts AC voltage to DC. The input of the rectifier is connected to three phases: DC (+), DC (neutral) and DC (-). The inverter unit converts these DC voltages of the DC bus to the required three-phase AC motor voltage and frequency. The conversion from AC to DC and then back to AC is done as a result of IGCTs (integrated

gate-commutated thyristor) and diodes, which means that the inverter combines within itself both voltage control and frequency control. [6] Power devices in the thyristor family are popular choices in applications having inverter power ratings beyond 1 MW. [7, p. 242]

Common-mode voltage production is typical among inverters [8] and is defined as the arithmetic mean of line-to-earth voltages [4, p. 7]. If the electric motor is star connected, the common-mode voltage (V_{com}) is defined by the voltage between the star point and earth [9]:

$$V_{com} = \frac{V_{ag} + V_{bg} + V_{cg}}{3}, \tag{1}$$

where V_{ag}, V_{bg} and V_{cg} are the line-to-earth voltages (or line-to-ground voltages). These voltages are illustrated in Figure 2 in order to better understand which voltages are treated. Deriving from Equation 1, the common-mode voltage can be theoretically zero if the motor is supplied by a sinusoidal three-phase voltage source. However, the input of the inverter has two levels: DC (+) or DC (-). On the other hand, each inverter output's phase voltage can be connected to either DC links DC (+) or DC (-). This means that, because of the three phases, these voltages never sum up instantaneously to zero. This common-mode voltage is seen by the motor terminals.

Another typical characteristic of voltage source inverter's output voltage is high *dv/dt*. Semiconductor power switches, including IGCTs, are turned on and off very fast, thus creating rapid changes in voltage (high *dv/dt*). [10, p. 63–87]

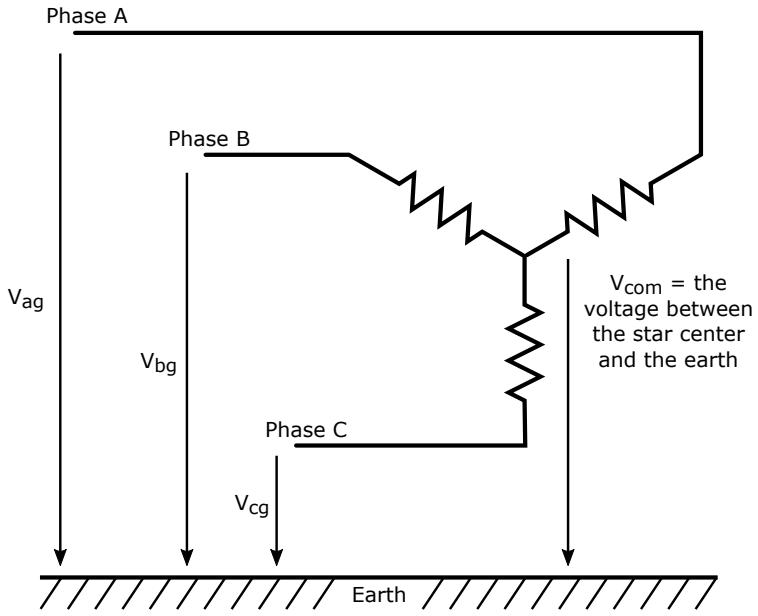

Figure 2: Illustration of the line-to-earth voltages V_{ag}, V_{bg} and V_{cg} to demonstrate the common-mode voltage which is the voltage between the three-phase windings star point and the earth. The line-to-earth voltages are the measured voltages between a terminal (motor or inverter) of each phase and the earth.

2.2 Azipod

The Azipod (Figure 3) consists of a steering module and a propulsion module that are controlled from the wheel house and monitored from the engine control room. The steering module enables the propulsion module to rotate 360 degrees on its vertical axis. In this work we are interested in the propulsion module of the Azipod XO2300 product. This product is the biggest, most expensive, and it is used in many projects within ABB Marine. The main component of the Azipod XO2300 is the fabricated steel hull, in which a synchronous three-phase motor drives a fixed-mounted propeller. The propulsion module is submerged, but due to the steel hull, the electric motor operates in a dry environment.

Azipod propulsion units are available for power ratings from 18 to 23 MW. The motor main supply voltage is approximately 3 kV and the nominal rotation speed of the motor shaft is from 112 to 155 rpm.

The motor's shaft consists mainly of a propeller bearing (DE bearing), a thrust bearing (NDE bearing) and a brushless exciter. The propeller bearing consists of a roller type bearing and the thrust bearing consists of roller and sliding type bearings. The brushless excitation has an AC to AC transformer, in which the magnetic circuit is divided into rotary and stationary parts. The stationary part consists of a diode rectifier producing DC current to the rotor.

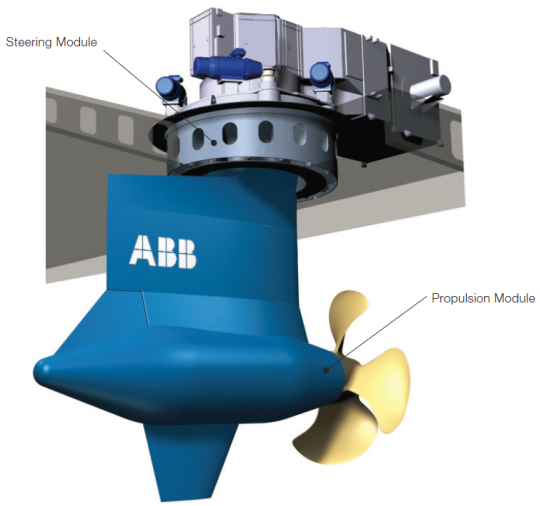

Figure 3: Azipod XO layout showing the propulsion module and the steering module. [11]

3 Bearing Current Phenomenon

The previous section presented the main components of the drive system. This chapter presents the damages in the bearings caused by the bearing currents, which are also discussed in this section. In addition, this chapter presents the main parasitic coupling capacitances in the motor that affect the bearing currents and voltages. Finally, bearing current related earthing system and modeling of the bearing are presented in this section.

3.1 Bearing Damages

Bearings are one of the most critical and most fault prone components in the rotating machines. In the failure of the bearings, either the machine should be stopped in order to repair the fault or the bearings should be changed. Depending on the application of the motor, such a failure can have catastrophic consequences. Bearings are crucial in these rotating machines as they separate the rotating part from the fixed one, while at the same time it is the only mechanical linkage between the stator and the rotor. This linkage is achieved due to a thin film of lubrication oil (also called lubrication grease depending on the application) that keeps apart the elements of a bearing.

Bearings can either be rolling or sliding depending on their friction type and thus on the application of the rotating machine. Bearing type selection is limited by design parameters, which take into consideration the size and the speed of the machine, and the nature of the driven load [12].

Rolling bearings are designed to serve a certain time at a certain probability. This is called L_{10} life, which means that the bearings achieve a determined age at 90 percent probability. Whereas, if some sliding bearings are properly maintained they serve indefinitely. Rolling bearings are usually grease-lubricated. On the other hand, sliding bearings are normally used in medium and large drive motors, and are usually self -and oil-lubricated. In some cases, an external pressurized system is required for the lubrication of sliding bearings. [12]

Advancement in bearing technology has raised bearing life theoretically up to 60.000 hours, and with industrial usage from 20.000 to 40.000 hours [12]. However, the lifetime differs much with the design of the bearing and the application they are used in. Premature bearing failures can be divided into three categories: thermal, mechanical or electrical. Failures due to the first two causes are mechanical vibration, misalignment between load and motor shaft, incorrect greasing system or contamination of bearing lubricant. [13]

Generally in motors, up to 30 percent of motor failures are caused by bearing currents [14]. Electrically induced bearing failures can be roughly divided into frosting and fluting types. Small local arcs occur when the lubrication film is punctured due to a voltage in the bearing higher than the film's breakdown voltage. These arcs create small pits in the bearing races. These pits first appear in regions where the bearing is the loaded, thus where the lubrication film is the thinnest. [15] The early stage of the pitting (Figure 4) forms evenly distributed damage called frosting

(Figure 5) [4, p. 100] that has an appearance of sand blasting surface. Not all the pitting is flattened ideally, thus creating the other type of more serious damage that is fluting [4, p. 100]. The fluting leaves a washboard pattern (Figure 6) as the rollers/balls needs to jump over the unflattened pittings. The early stage of pitting is not visible to the naked eye, whereas fluting and frosting are.

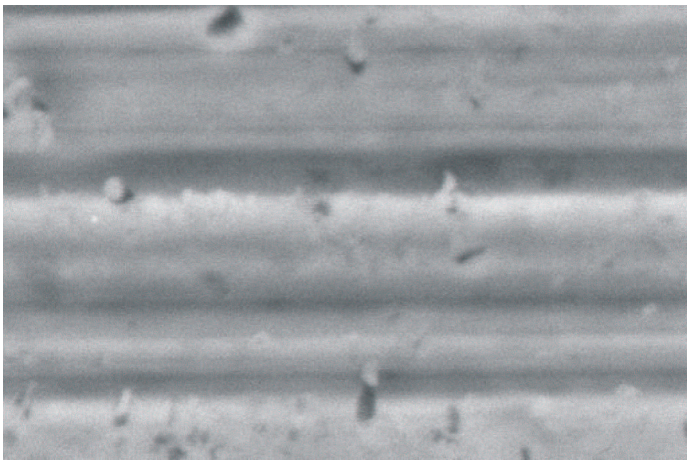

Figure 4: Early stage of pitting on the race surface in microscopic scale (scale of the figure is around 8 µm). [4, p. 99]

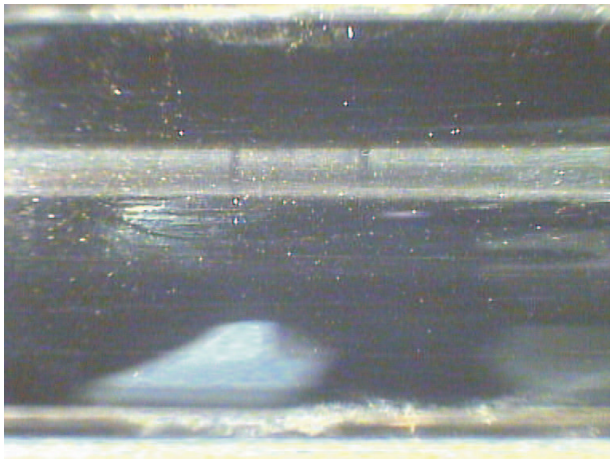

Figure 5: Frosting on the race surface. Scale of the figure is around 20 mm. [4, p. 99]

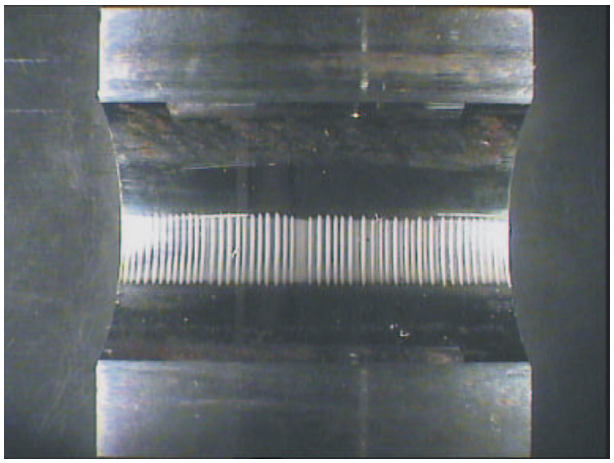

Figure 6: Bearing fluting on the race surface. Scale of the figure is around 40 mm. [4, p. 100]

As a result, a harmful bearing current flow is a current flow in the local metal contact points. These metal contact points have small diameters, thus have higher local bearing current density than the apparent bearing current density. Therefore, a combination of high local current density with metal conductivity dissipates high local power loss density and thus high local temperature. This temperature is high enough to melt the metal and creates craters. [4, p. 98]

3.2 Motor capacitances

This subsection deals with the capacitances in the motor that have an important role in high frequencies. These capacitances are useful in understanding and forming the high-frequency motor model. The capacitances for the most part depend on the geometry of the iron stacks or bearings, the permittivities of the different insulating materials, and the actual position of the conductors in the windings.

The main parasitic coupling capacitances are stator winding-to-rotor capacitance (C_{wr}), bearing capacitance (C_b), stator winding-to-frame capacitance (C_{wf}), and rotor-to-frame capacitance (C_{rs}) [16]. These main capacitances are shown in Figure 7.

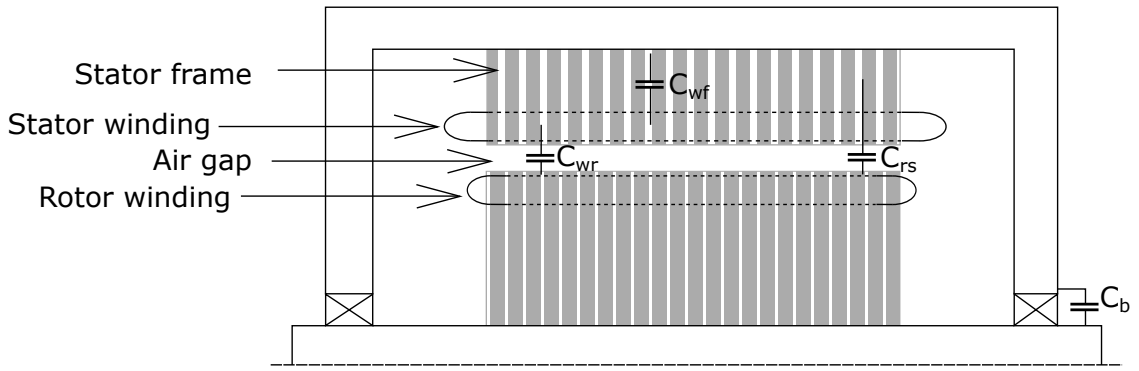

Figure 7: The four main parasitic coupling capacitances in AC motors.

The stator and the rotor windings are coupled by the stator winding-to-rotor capacitance C_{wr}. It is determined from the rotor surface to the stator winding, being separated by the insulations, air gap (rotor-to-stator), and slot wedges. C_b is the capacitance of the bearing in case the lubrication film of the bearing is not punctured and is still insulating, leading that the bearing acts as a capacitor [4, p. 9]. C_{wf} is the capacitance from the stator winding at high voltage to the earthed stator case, separated by winding insulation, and iron lamination stacks. C_{rs} is the capacitance from the rotor to the stator frame (mainly stator tooth tips).

Another capacitance worth mentioning is the capacitance (C_{ph}) in the overhang region of the stator. It is determined between the different stator phases and is separated by the phase-separator insulation. This phase-to-phase capacitance, C_{ph}, is considerably smaller than the winding-to-frame capacitance C_{wf} [17], and therefore it is not presented in any models in this work.

The capacitive coupling from the stator overhang to the rotor winding is assumed negligible in the Azipod system. For that reason it is also not considered in any model in this work. This is because the rotor winding, which does not have a considerable winding overhang, is axially much smaller than the stator winding.

3.3 Bearing Currents

All electric motors, DC or AC, regardless of size, are susceptible to bearing currents [16]. This subsection presents commonly recognized bearing currents and their classification. The cause-and-effect chain of the creation of bearing currents are explained in order to understand which bearing currents are relevant in the studied system.

Historical cause for bearing currents were the asymmetries in the motors. Asymmetries can be caused by rotor eccentricity, stator and rotor slotting or slot combinations, rotor misalignment, air-gap variations, excessive lamination-to-lamination variations, irregularities in slot punching, cooling ducts, keys and key ways, and variations in permeability [12]. Electric motors fed by a sinusoidal grid created unavoidable

induced shaft voltages due to the magnetic flux linkages caused by the asymmetries of the motors constructions. If the induced shaft voltage surpassed the breakdown limit of the bearings lubrication film, a circulating bearing current is created. [16] In addition, a static external excitation on the rotor may cause bearing currents in large synchronous generators [18][19].

Since the magnetic flux creates a loop linking stator frame, DE and NDE bearings, and shaft, it creates circulating bearing currents in the mentioned loop. This current is more likely to occur in bigger motors as the flux linkage is higher. [4, p. 3–4] Nevertheless, present-day motor design and manufacturing has almost eliminated these so called classical bearing currents. [20] It is assumed that the magnetic circuits due to the asymmetries in the motor are negligible and therefore line-operation bearing currents are not in the focus of the presented work. In this work we are interested in the inverted-fed bearing currents.

Added to the above mentioned classical bearing currents are the bearing currents caused by the inverter supply. Azipod propulsions are also prone to these currents due to the ACS6000 SD drive. The common-mode voltage created by the inverter is the cause for the bearing currents. Additionally, since the common-mode voltage interacts with the capacitances in the motor and these capacitances are not in effect in the direct online operation, it is assumed that these capacitances create the inverter related bearing currents [21]. Four types of bearing currents caused by the inverter are distinguished. They are capacitive bearing currents, electrostatic discharge currents (EDM-currents), circulating bearing currents, and rotor ground currents. [4, p. 10–14] Each inverter-induced bearing current is explained in the next paragraphs.

• Capacitive bearing current

The common-mode voltage, V_{com}, causes a voltage drop, v_b, between the inner and the outer race of the motor bearings, and it follows the waveform of the common-mode voltage V_{com}. At speeds normally higher than 100 rpm and at low temperatures, around 25°C, the bearing's oil lubrication forms a small insulating layer and the bearing acts like a capacitor [4, p. 10, p. 108][5, p. 9]. The bearing capacitance C_b with the dv/dt over the bearing creates a current:

$$i_b = C_b \cdot \frac{dv_b}{dt}, \tag{2}$$

which ranges from 5 to 10 mA. This current is called the capacitive bearing current. As it is too small, it is not harmful to the bearings. [4, p. 10] However, with the help of Equation 2, the role of the switching time can be explained. The faster the switching is, the smaller the dt is and the higher the i_b is.

• EDM-currents

When the lubrication film of the bearings is undamaged, the bearing voltage v_b mirrors the common-mode voltage at the stator terminals [4, p. 11]. Its value is determined by the ratio of the significant capacitances within the motor [5, p. 9]. The main significant capacitances are presented in the previous subsection. The

lubrication film charges electrically, and if its threshold voltage is exceeded the lubrication film breaks down (threshold voltage approximately from 6 to 35 V [16]). After the breakdown, the lubrication film discharges in a pulse manner and causes EDM-currents [4, p. 11]. The phenomenon can be modeled with a simple circuit (see Figure 9 of the next subsection), where the loaded bearing capacitance C_b is in parallel with the bearing resistance R_b (which is very non-linear and unknown [22]). When the capacitance C_b discharges via the resistance R_b, it results in a current pulse having a maximum amplitude of:

$$i_b = \frac{v_b}{R_b}, \tag{3}$$

where v_b is the bearing breakdown voltage and R_b the bearing resistance. [4, p. 121] These peak amplitudes are approximately from 0.5 to 3 A with an oscillating frequency of several MHz, and these currents are especially harmful in small motors. [4, p. 11–12]

• Circulating bearing current

The common-mode voltage created by the inverter excites the parasitic capacitances in the motor that offer the low-impedance paths and produce the high frequency common-mode currents [3]. These common-mode coupling currents create a flux in the stator yoke that links the closed loop formed by stator, motor shaft and both end bearings. This magnetic flux then induces a high frequency shaft voltage (especially important voltage in larger motors [23]). If this voltage is higher than the bearings lubrication's breakdown voltage, it destroys the lubrication film's insulating properties and a circulating bearing current is created. [3][5, p. 10][4, p. 11] This circulating bearing current flows in the closed loop consisting of stator frame, NDE bearing, motor shaft, and DE bearing. [24] The peak amplitude of the circulating bearing current varies with the size of the motor and is characterized by an oscillating frequency of several 100 kHz [4, p. 11, p. 13].

• Rotor ground current

Due to the common-mode voltage, some of the common-mode current leaks from the stator to the stator frame. This causes an increase in the potential of the frame in respect to the source's grounded potential. The potential of the motor frame can discharge through the bearing if the frame voltage is higher than the impedance of the bearings lubrication film and if the stator frame is poorly grounded. In addition, if the driven load provides a low-impedance path for the discharged current, it creates the rotor ground current. [25, p. 9][5, p. 10, p. 15][4, p. 14] Rotor ground currents occur only when the rotor is grounded [26] and it passes mainly through the DE bearing [5, p. 15]. This current can reach considerable amounts with the increasing motor size and it is harmful to the bearings since it passes nearly totally through the bearings. Another characteristic of the rotor ground currents is an oscillating frequency of several 100 kHz. [4, p. 13–14] When the rotor ground currents occur, they are added to potentially existing circulating bearing currents. In this case EDM-currents are blocked, since the bearings have lost their insulating properties. Usually when bearing currents occur, one type is the most dominant. [21]

Figure 8 summarizes the cause-and-effect chain of above presented bearing currents. Capacitive bearing currents and EDM-currents are related to the effect of the common-mode voltage on the bearing voltage. Inverter-induced circulating bearing currents and rotor ground currents result from the high frequency common-mode currents.

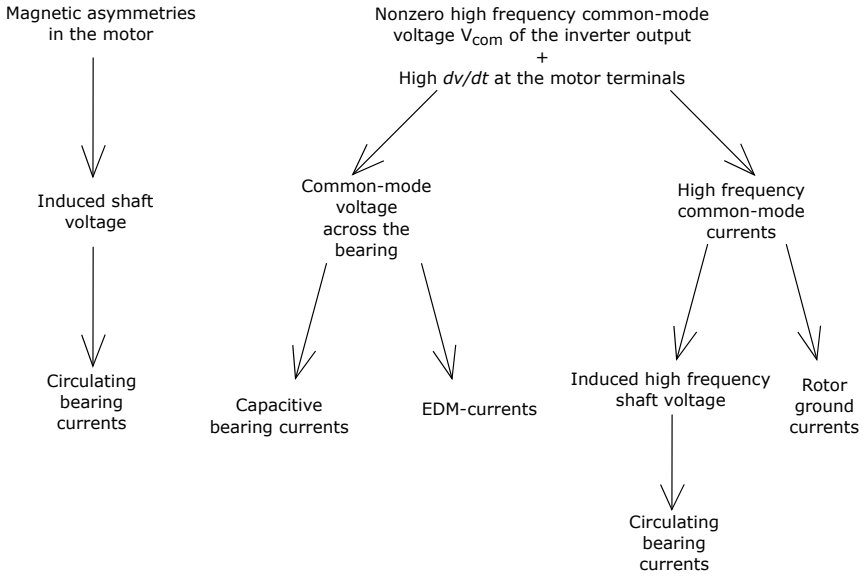

Figure 8: Chain of creation of different bearing currents. Left chain shows the mechanism of classical bearing currents, whereas the right chain shows the mechanism of inverter-induced bearing currents.

3.4 Bearing Current Related Earthing System

In case there are shaft voltages created in the system and thus shaft currents, the shaft must be grounded by grounding brushes [18]. In general, a brush is used to form an electric contact between two elements that conduct, where one is rotating and one is at rest. In electric drives, this means a contact between the rotating shaft and the stationary stator.

Brushes are used mainly for two purposes: current conduction and prevention of voltage buildup. Brushes should carry a current of several tens of amperes as well as discharge low voltages, both requirements at high frequencies. Consequently, these brushes are used for mitigation purposes of high-frequency bearing currents created by the inverter [27]. There are different types of brushes such as bristle, carbon, copper and brass types [18]. Carbon brushes with electric conducting graphite have been used for conducting the currents from the shaft for several years [27].

The brush and the shaft form a low friction sliding contact. A humid environment can create a water layer (in Azipod propulsions it could be an oil layer) on the graphite, thus increasing the self-lubricating properties of the brush. This layer, with the interaction of the current with the graphite, ensures minimum mechanical

wear of the brush, and avoids an increase in the resistance of the brush. However, brushes have a few drawbacks such as excessive wear, and hotspot molding if the conducting sliding contact is decreased. Another problem is the dusting of brushes in applications where there is low humidity. Additional problems, such as maintaining good electrical contact, can be created when used in inverter applications where high frequencies and voltages can occur. The problems are related to the rotation of the shaft, thus on the microscopic level, to the distance between the stationary and rotating element that varies with the roughness of the shaft's surface and to the centering/alignment of the shaft. [27] Although in Azipod propulsion units, the thin oil film can help reduce the friction, and mechanical wear of the brushes, the impurities of this oil can cause a reduction of easy electrical conduction from the shaft line to the brush.

In the Azipod system, one of the bearing current countermeasures is an appropriate shaft earthing system. At the propeller side there are two brushes providing the shaft current with a proper low-impedance path to the earth. Thus, it is crucial that the brushes' resistance values do not increase. These propeller side brushes have an important role under normal operation as they ensure that no harmful currents will flow to the propeller side via bearings. In the ideal case, all the current will flow via brushes to the earth. On the thrust side, there are also two brushes, but not for earthing purposes since the thrust side's bearing shield is completely insulated. Here, the brushes are used for the purpose of balancing the bridge over the thrust bearings, ensuring the same potential over the slide and radial bearings.

Currently the brushes used in the Azipod are made of 85 % copper and 15 % graphite (grade type K106). According to the brush supplier, a brush with 50 % silver and 50 % graphite (grade type K017) provides lower friction, and possibly lower contact resistance resulting in longer product life expectancy. Nonetheless, this new solution should have worthy gains on lower shaft voltages, and life expectancy since the price is high for such a large brush that is used in the Azipod units.

In the equivalent circuit of the motor the brushes are modeled as resistors. A switch can be added in series to describe a situation when the brush is not working or to simulate a situation without the brushes. In this case the switch would be "up". However, for simplicity, the brush is drawn in the model as a resistor without the switch. The brush supplier carried out tests in order to verify the nature of the brush and to define its values. More details of the tests are shown in Appendix B.

3.5 Impedance behavior of bearings

Bearing impedance and the nature of it will determine, to a large extent, the bearing current that flows in the system. The bearing is a complex structure characterized by non-linear impedance, and therefore is hard to analyze. The Azipod system's thrust bearing unit consists of the radial roller bearing and slide thrust bearing. This dual bearing solution ensures the best performance in carrying forces from different directions. The roller bearing carries radial forces, whereas the slide bearing carries axial forces. The bearings should be modeled in order to simulate the bearings' currents and voltages.

In the radial bearings, the actual contact area is large in non-rotation or at low speeds [2]. Bearings rotating at speeds higher than 10 % of rated ones have a partially insulating lubricant between the metallic contacts of the outer and inner races of the bearing [2], thus forming a capacitance due to the lubricant. Bearings capacitance depends on the rotating speed, load, temperature, bearings geometrical dimensions, and the characteristics of the lubricant [28].

Different ranges of operation for the bearings can be distinguished: standstill, rotating, and threshold voltage passed (motor rotating). Bearings of a motor that is not rotating have a thin lubrication layer. Voltage applied to bearings can create currents due to the thin lubrication layer. However, the metallic contact area is large and the bearings can withstand relatively large currents [4, p. 108].

For the equivalent circuits, bearings can be modeled as a capacitance C_b and a resistance R_b of lubricant film (in the range of MΩ) in parallel (Figure 9). The equivalent circuit with the bearing model is for the rotating motor, as it is the mode of operation assumed to be the most prone to damages. In the simplified bearing model, there is a switch connecting the resistance. If the lubrication film is intact, the switch is up (not conducting) and the bearing is mainly capacitive. Immediately after the breakdown, the switch is down and the bearing is mainly resistive (a few ohms [4, p. 109]). Consequently, the switch commutates from the C_b to R_b branch. The breakdown happens when the threshold limit of the bearing is exceeded [29]. Since the bearing resistance before the breakdown is high, it is neglected in the circuit models.

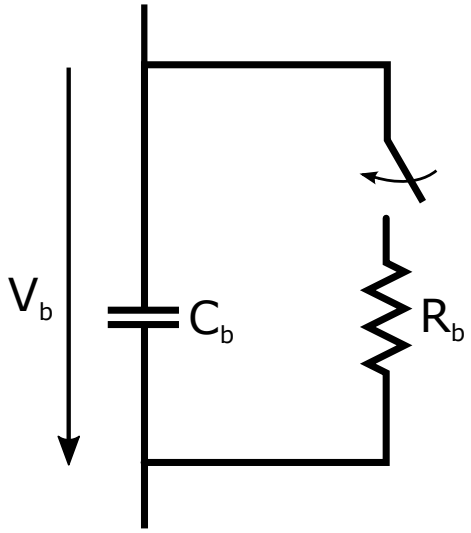

Figure 9: Simplified bearing model. A switch modeling the behavior of the lubricant.

The central lubrication thickness h_c of a roller bearing, determined by the laws of hydrodynamics, is not constant, but can be calculated with the following equation:

$$h_c[mm] = 2.922 \cdot R_{eq}[mm] \cdot U_r^{0.694} \cdot G^{0.47} \cdot W^{-0.166}, \tag{4}$$

where U_r is a speed parameter, G is a material parameter, W is the load parameter

and R_{eq} is the combined equivalent radius of curvature [29]. One can see from the equation, that as the speed increases, so does the lubrication thickness. However, in increasing temperatures, the lubricant's insulating properties decrease [29].

• Analytical calculation of roller bearing capacitance

In order to calculate the capacitance of a radial bearing, one should understand the geometrical structure of the bearings and the made assumptions. The radial curvature of the inner and the outer bearing is considerably larger than the roller radius, therefore the raceway is considered as a flat line [29] (see X-direction in Figure 10). This assumption helps in calculating the capacitance in the Hertz'ian contact area, and the distance between the roller and raceway. The Hertz'ian contact area (A_{Hz}) is the deformation area of the rolls of the bearing under mechanical pressure [4, p. 211].

In the Hertz'ian contact area and next to it (up to $100 \cdot h_c$, see Figure 11) are the biggest capacitances, while the other capacitances can be neglected. Thus, two main capacitances will be considered. One is the capacitance in the Hertz'ian contact area (C_{Hz}) which is separated by the lubricant with a distance h_c. The second one is the capacitance near the contact area (C_{air}) and in the calculations, it is separated by air since a much bigger part of air than lubricant is separating the roller from the raceway. This assumption does not affect the capacitance C_{air} by more than 10 to 15 %. Other neglected assumptions are asperities and contaminations on the surface, and the surface roughness.

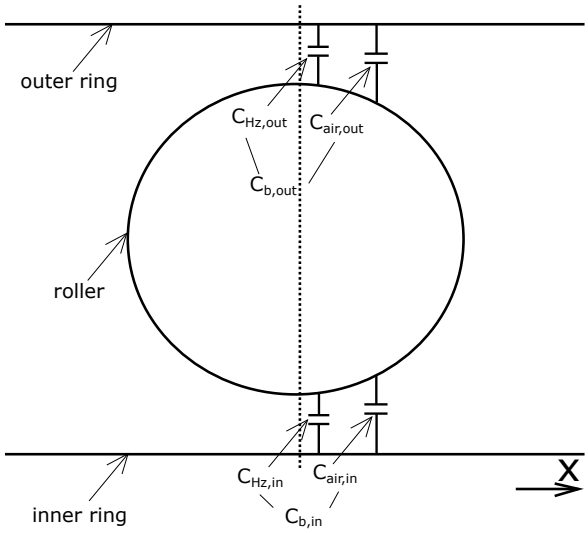

Figure 10: Axial cross-section of one roller element. Since it is symmetric, the capacitances are shown only in one half.

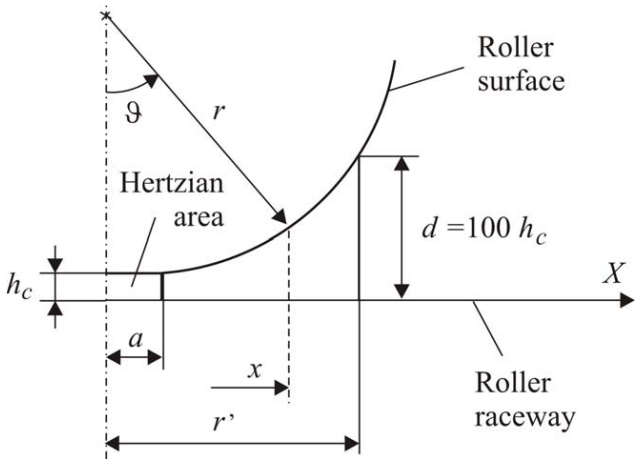

Figure 11: Axial cross-section of a roller element. [29]

In Figure 10, the capacitances $C_{Hz,in}$ and $C_{air,in}$ are in parallel, as are the capacitances $C_{Hz,out}$ and $C_{air,out}$. These capacitances form $C_{b,in}$ and $C_{b,out}$ which are in series. Consequently, the radial bearing capacitance for N rollers is calculated as:

$$C_b = N_z \cdot \frac{C_{b,in} \cdot C_{b,out}}{C_{b,in} + C_{b,out}}, \tag{5}$$

where $N_z = N/4$ (approximate number of roller elements in the loaded area), $C_{b,in} = C_{Hz,in} + C_{air,in}$ and $C_{b,out} = C_{Hz,out} + C_{air,out}$ [29].

The Hertz'ian contact area can be assumed as a flat surface and therefore the capacitance in that region can be calculated as a plane capacitor:

$$C_{Hz} = 2 \cdot \epsilon_0 \cdot \epsilon_r \cdot \frac{A_{Hz}}{h_c}, \tag{6}$$

where ϵ_0 is vacuum permittivity, ϵ_r is the relative permittivity of the lubricant, A_{Hz} is the Hertz'ian contact area, and h_c is the central film thickness of the lubricant. The equation is multiplied by two, since in Figure 11 is presented only half of the roller and the geometry of the roller is symmetric. The same is for the air capacitance C_{air}.

The air capacitance from a to r' can be calculated as follows:

$$C_{air} = 2 \cdot \epsilon_0 \cdot \int_a^{r'} \frac{RE_{length}}{h_c + \delta_x x^2} dx, \tag{7}$$

where RE_{length} is the length of the roller element and $\delta_x = \frac{1}{2 \cdot r}$ (r is the roller radius) [29].

For a there is no predefined value, so it is calculated from the Hertz'ian contact area A_{Hz} and the length of the roller element RE_{length}:

$$\begin{aligned} A_{Hz} &= 2 \cdot RE_{length} \cdot a \\ \Rightarrow a &= \frac{A_{Hz}}{2 \cdot RE_{length}}. \end{aligned} \tag{8}$$

The value r' is determined from the geometry of Figure 11, where a right-angled triangle is formed having one side (hypotenuse) r, the other side $r - 99 \cdot h_c$ and the remaining side r':

$$\begin{aligned} r^2 &= (r')^2 + (r - 99 \cdot h_c)^2 \\ \Rightarrow r' &= \sqrt{r^2 - (r - 99 \cdot h_c)^2}. \end{aligned} \tag{9}$$

After calculating the analytical values of the required capacitances ($C_{Hz,in}$, $C_{air,in}$, $C_{Hz,out}$ and $C_{air,out}$), we obtain for the drive end bearing (C_{bDE}): $C_{b,in} = C_{Hz,in} + C_{air,in} = 1.671 \times 10^{-8} + 2.103 \times 10^{-10} = 1.692 \times 10^{-8}$ F and $C_{b,out} = C_{Hz,out} + C_{air,out} = 1.430 \times 10^{-8} + 1.955 \times 10^{-10} = 1.45 \times 10^{-8}$ F. The parameters obtained for the roller bearings are assumed for a shaft speed of 120 rpm with bearings inner ring temperature of 70°C and the outer ring temperature is 10°C cooler. Finally, the capacitance of the drive-end bearing is:

$$\begin{aligned} C_{bDE} = N_z \cdot \frac{C_{b,in} \cdot C_{b,out}}{C_{b,in} + C_{b,out}} &= 8 \times \frac{1.692 \times 10^{-8} \times 1.45 \times 10^{-8}}{1.692 \times 10^{-8} + 1.45 \times 10^{-8}} \\ &= 6.247 \times 10^{-8}\ F = 62.47\ nF. \end{aligned} \tag{10}$$

For the non-drive end bearing (C_{bNDE1}) we get: $C_{b,in} = C_{Hz,in} + C_{air,in} = 5.943 \times 10^{-9} + 2.704 \times 10^{-10} = 6.213 \times 10^{-9}$ F and $C_{b,out} = C_{Hz,out} + C_{air,out} = 5.157 \times 10^{-9} + 2.471 \times 10^{-10} = 5.404 \times 10^{-9}$ F. The capacitance of the non-drive end slide bearing is:

$$\begin{aligned} C_{bNDE1} = N_z \cdot \frac{C_{b,in} \cdot C_{b,out}}{C_{b,in} + C_{b,out}} &= 8 \times \frac{6.213 \times 10^{-9} \times 5.404 \times 10^{-9}}{6.213 \times 10^{-9} + 5.404 \times 10^{-9}} \\ &= 2.312 \times 10^{-8}\ F = 23.12\ nF. \end{aligned} \tag{11}$$

According to the manufacturer (SKF) of the roller bearings, every lubricant has a certain breakdown voltage and if exceeded, electrical discharges will take place in the form of sparks. This is assumed in the case when the bearing is initially in the full-film lubrication regime. Typically, the ideal film thickness in the rolling contact is only a few hundred nanometers, and the discharges are triggered with only a few volts. These discharges naturally depend on several factors. Thus, no exact breakdown voltage of the lubrication can be given covering the whole operating regime.

• Analytical calculation of slide bearing capacitance

The analytical calculation of the slide thrust bearing is simpler than the roller bearing as it has 14+14 circular shape pads. The circular pads are made of white metal and supposedly conduct electrical currents. These sliding surfaces (also called pads) have an identical area which makes it easy to calculate their total capacitance. The first 14 pads that carry the thrust forces are in parallel with the other 14 pads that carry the reverse direction forces. The capacitance of a single thrust pad is

$$C_{thrust-pad} = \epsilon \cdot \frac{A_{pad}}{d_{thrust}}, \tag{12}$$

and the capacitance of a reverse direction pad is

$$C_{reverse-pad} = \epsilon \cdot \frac{A_{pad}}{d_{reverse}}, \tag{13}$$

where ϵ is the permittivity of the lubricant, A_{pad} is the area of the pad, d_{thrust} and $d_{reverse}$ are the distances from the pads to the conducting part of the shaft ($d_{thrust} \neq d_{reverse}$).

Since each set of 14 pads are in parallel, the total capacitance of the thrust pads is

$$C_{thrust} = 14 \cdot C_{thrust-pad}, \tag{14}$$

and respectively

$$C_{reverse} = 14 \cdot C_{reverse-pad}, \tag{15}$$

for the reverse pads. The capacitance C_{thrust} and the capacitance $C_{reverse}$ are in parallel forming a total capacitance C_{bNDE2} with the help of Equations 12–15:

$$\begin{aligned} C_{bNDE2} &= C_{thrust} + C_{reverse} = 14 \cdot C_{thrust-pad} + 14 \cdot C_{reverse-pad} \\ &= 14 \cdot \epsilon \cdot \frac{A_{pad}}{d_{thrust}} + 14 \cdot \epsilon \cdot \frac{A_{pad}}{d_{reverse}} = 14 \cdot \epsilon \cdot A_{pad} \cdot \left(\frac{1}{d_{thrust}} + \frac{1}{d_{reverse}}\right) = 420.4\ nF. \end{aligned} \tag{16}$$

3.6 Elements affecting the common-mode phenomenon

This subsection introduces some points that affect the common-mode phenomenon either positively or negatively in the Azipod environment and could provide some ideas for further studies.

• Effects of cables

This work mainly focuses on the motor itself. However, a few things should be pointed out, which might affect the common-mode phenomena in the system. The main cabling can either be a complete three-phase cable (see Figure 12) or bundled up in three single-phase cables forming a three-phase system. Geometrically, this makes a difference, and it can be seen when observing the cables' cross-sections. The first one forms a symmetric triangle itself, whereas the latter does not form a symmetric triangle, and already creates a non-symmetric system. The more asymmetries there are in the system, the more harmful the common-mode voltages are. This is why it is essential to have a symmetric system with the main cabling as well as within the motor construction as discussed in the earlier chapter.

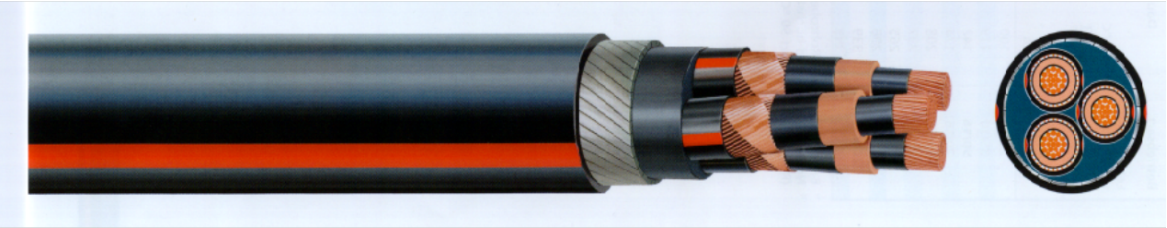

Figure 12: Three-phase cable with individually shielded conductors. Electromagnetically preferred solution.

Electromagnetically, three-phase main cabling is better, and it used to be a more common option, but it has a few drawbacks. Three-phase main cabling is heavy to handle and carry in the shipyard, and it is difficult or impossible to fold compared to the single-phase cabling. This is the reason why shipyards request single-phase cabling and it is unfortunately the trend right now.

Furthermore, for long cables, the line-to-ground voltage at the motor terminals oscillates due to the wave reflection. This motor terminal voltage can reach considerable maximum values. This overvoltage has a negative contribution in the common-mode system and in the prediction of common-mode voltages and currents. In addition, longer cables lead to higher voltage drops.

Finally, the thrust bearing has a large number of cables and sensors. During assembly, special care should be taken of the parts that have contact with the bearing shell or shaft in order to not bridge the insulations by other components, such as the piping of the lubrication system or the thermometers. Due to the large number of auxiliary cables and the complexity of their analyzes, this work assumes that no leakage is happening from these cables, and that the insulation is perfect.

• Input transformer

The input transformer cuts galvanically the drive's input cables from the mains, leading to smaller cable capacitances than without the transformer. The input transformer contributes to a smaller common-mode main circuit since the voltage cannot propagate and reflect from the other side of the transformer.

• Excitation system

As mentioned in the introduction, before using DTC adjustable speed technology, the Azipod units were fed by cycloconverters. With cycloconverters, the excitation system was the same, and at that time there were no bearing current problems. The currents and voltages in the shaft caused by the excitation machine are neglected entirely in this work. The excitation machine is left out mainly because it is not assumed to be a source of harmful currents, even though the input voltage was lower with cycloconverters. Moreover, the inductance of the excitor's winding is high, having constant DC current and is separated galvanically from the AC input. Nevertheless, the complete effect of the excitation machine is still unclear due to the complexity of the overall system and lack of references. However, the effect of the

excitation system should be considered in future works.

4 Present Bearing Insulation Solution

The present insulation solution is technically and logistically challenging, as well as expensive. Requirements for the insulation are demanding where mechanical properties, electrical properties and environmental conditions must be taken into consideration. The role of the insulation is to block the harmful currents from passing through the bearings. In general, the insulation is present to protect the bearings and to keep the machine functioning by avoiding bearing damages caused by electrical reasons. The insulation should be thick enough to not behave as a small capacitor, but also thin enough to minimize potential long term material creepage problems in used application.

The bearing shield insulation consists of two different sections: axial surface and radial surface (Figure 13). Each section has a different material requirement as they are suppressed into different loads. The axial part should withstand higher loads than the radial part, and is the reason for allowing weaker materials in the mechanical sense for the radial part. Axial and radial insulations are called by the supplier as insulation plate and wound insulation, respectively. Added to the two different sections of the bearing shield insulation is the insulation bushing that insulates the fastening bolt. The insulation supplier should test every finalized product providing material datasheets or test reports to ABB.

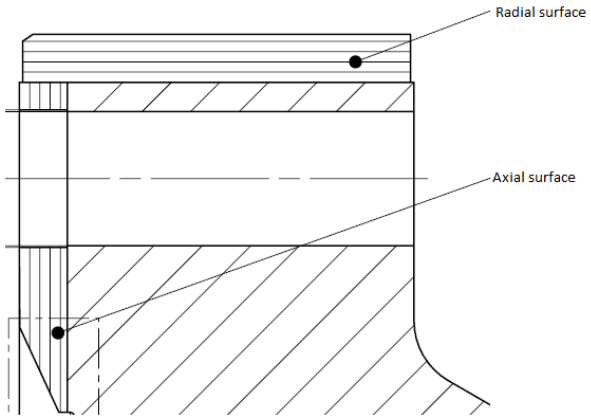

Figure 13: Two different sections of the insulation. Radial surface taking forces from "up" and axial from "right". This caption is from the top part of the bearing shield.

5 Development of the Equivalent Circuit

This section presents a high-frequency model of the drive for the purpose of analyzing the common-mode current and the bearing voltage. Figure 14 will be the starting point for the creation of the model. When the machine is fed with common-mode voltages with high-frequency components, the parasitic capacitances that were introduced in subsection 3.2 must be considered. Therefore, at high frequencies, a standard equivalent circuit of the motor is no longer valid. [4, p. 10, p. 110] The equivalent circuit introduced in this work is a non-linear combination of the earlier presented parasitic capacitances, inductances, and resistances that vary with the frequencies. Several high-frequency models have been presented in literature for a system of inverter, cables and motor. However, this work focuses only in the high-frequency representation of the motor.

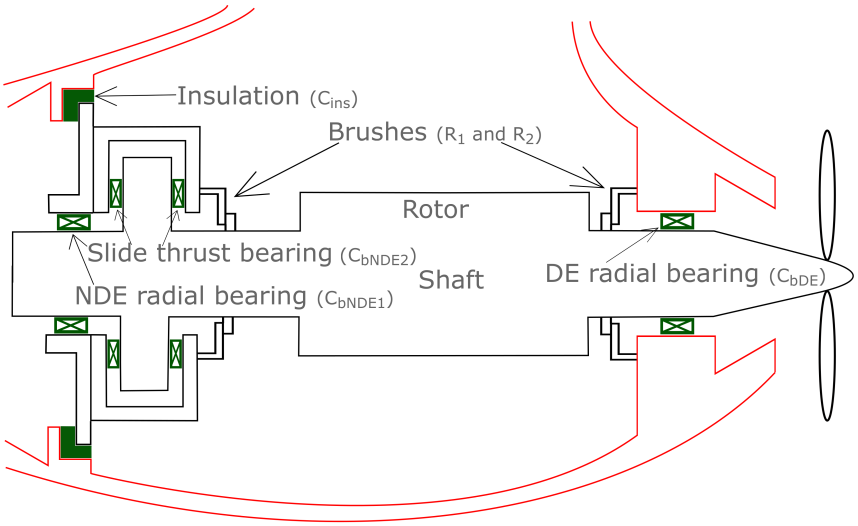

Figure 14: Simplified graphic of Azipod consisting of thrust bearing and its insulation, earthing brushes, rotor, motor shaft and drive-end rolling bearings. The stator, as well as the excitation system, are left out in order to prevent complications in the figure. These components have their equivalent circuit symbols in parenthesis.

5.1 Three-phase high-frequency model

High-frequency models can be presented as transmission line models or frequency-response models depending on the structure of the drive system and on the parameter determination methods. In this work, the frequency-response model is used due to its simplicity over the transmission line model. However, experimental measurements are needed to determine some parameters. Time-domain simulations can be done using the frequency-response model.

A high-frequency model originally developed for induction motors and proposed in [30] is used here as a base model. The model in [30] has been proved to be accurate for induction motors with rated power up to 240 kW. It is reasonable to use the induction motor model for a frequency level of at least up to 1 MHz, since the impedance-response curves are almost the same as the ones in synchronous motors. Impedance-response curves were obtained by measuring phase-to-neutral and phase-to-ground motor impedances. [31] In ABB's induction motor factory at Pitäjänmäki, same measurements for a 1400 kW machine were carried out. Results are shown in graphs in Appendix C.

In order to capture the machine's two impedance resonances, the stator winding-to-frame capacitance C_{wf} should be separated into capacitances C_{wf1} and C_{wf2}, that are illustrated in Figure 15. The winding-to-rotor capacitance C_{wr} is also separated into capacitances C_{wr1} and C_{wr2}. The winding is modeled by one RL branch consisting of eddy current loss resistance R_e and leakage inductance L_s. The RL branch takes into account the skin and proximity effect, and the high frequency iron losses. The branch is connected with the four above mentioned capacitances C_{wf1}, C_{wf2}, C_{wr1} and C_{wr2}. [30] [32] Ways of determining these parameters is presented in the following subsection.

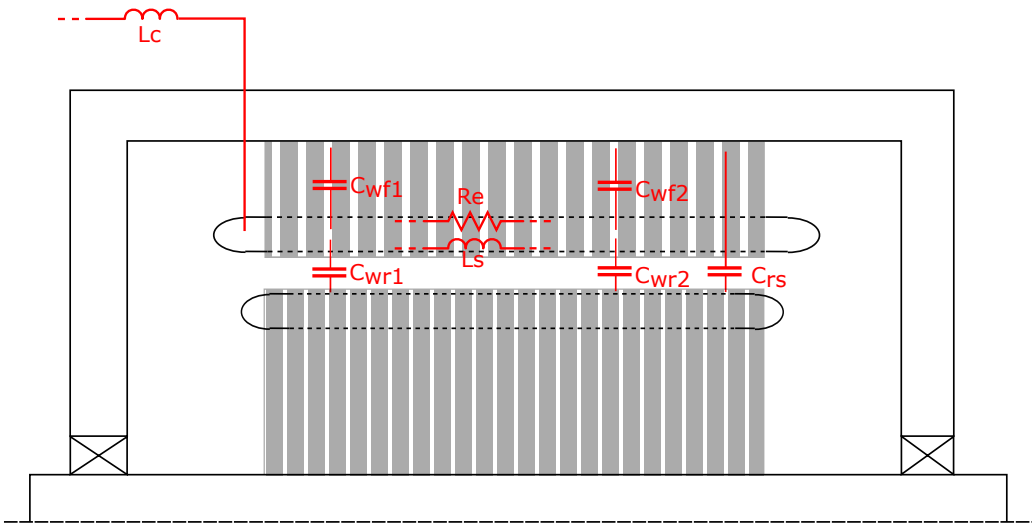

Figure 15: A figure to understand where are exactly the components used in the equivalent circuit model.

The capacitances C_{wf1}, C_{wf2}, C_{rs}, C_{ins} (capacitance of bearing shield insulation) and C_{bDE} with the resistances R_2 and R_3 must share a common point on the stator frame (Figure 16). R_2 is the resistance of the earthing brush and R_3 is the resistance of the shaft end and the propeller. These components are connected to R_g, which is the dissipative loss resistance caused by the common-mode current flowing in the stator yoke and the frame. R_g includes also other losses associated with the current flow from the stator to the ground via the frame. The parasitic inductance L_g of the stator lamination will not be presented in the model as it is small, but it will be part

of the connectors and internal line conductors inductance L_c. On the other hand, the capacitances C_{bNDE1}, C_{bNDE2}, C_{wr1}, C_{wr2} and C_{rs} with the resistances R_1, R_2 and R_3 must share a common point on the rotor, see Figure 16 and Figure 17. In Figure 16 gray boxes illustrate the main areas of the Azipod that is presented in Figure 14.

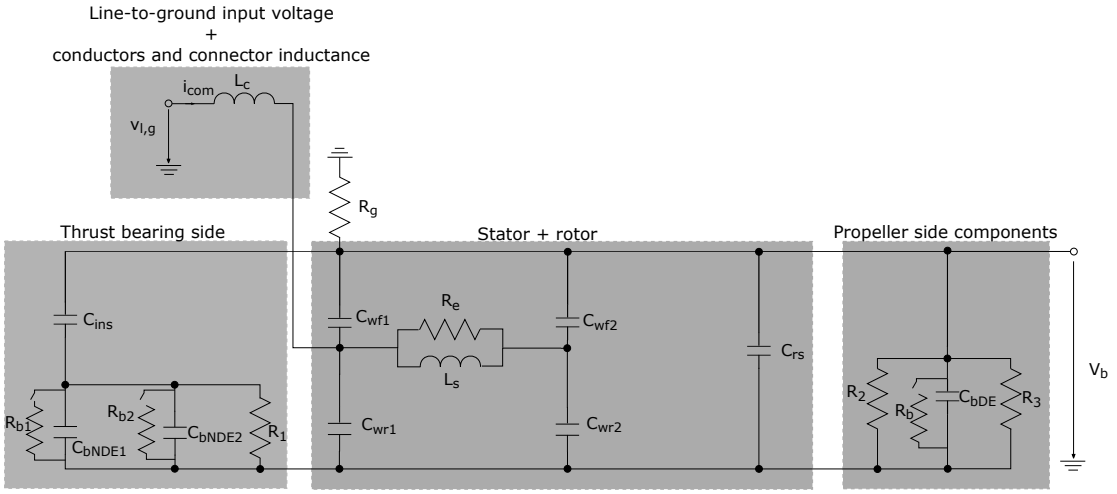

Figure 16: Per phase high-frequency model to calculate common-mode current and bearing voltage. R_b, R_{b1} and R_{b2} are the bearing resistances.

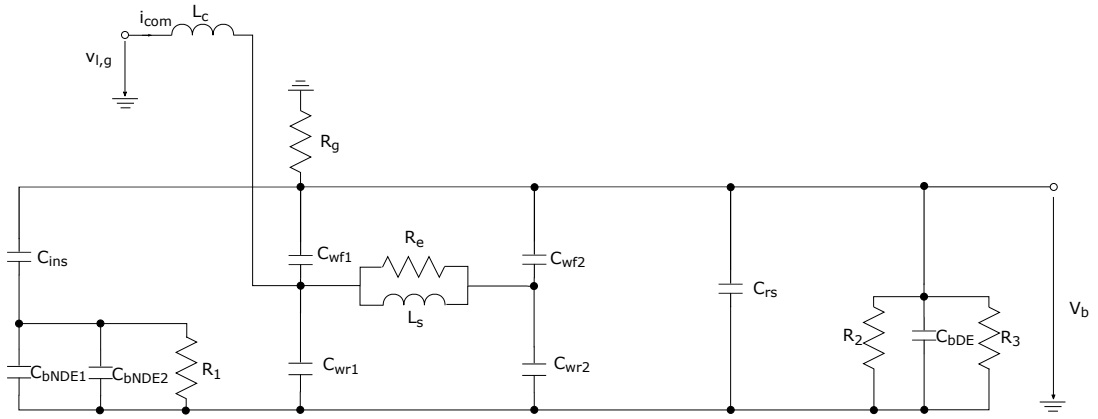

Figure 17: Per phase high-frequency model for simulation with bearings lubrication oils insulating.

Each per phase is equal by assuming that the motor construction is symmetric, which is not far from reality considering today's manufacturing technology. This means everything involving windings' phases should appear three times and identically in the model, as shown in Figure 18. The stator winding-to-frame capacitances C_{wf1} and C_{wf2} (C_{wf}) of each phase should share a common point in the stator frame. Whilst the stator winding-to-rotor capacitances C_{wr1} and C_{wr2} (C_{wr}) of each phase should share a common point in the rotor. The intersections of C_{wf2}, C_{wr2} and the

RL branch of each phase should be connected from one side while the other side, intersections of C_{wf1}, C_{wr1} and the RL branch, will have line-to-ground voltage (V_{ag}, V_{bg} and V_{cg}) inputs.

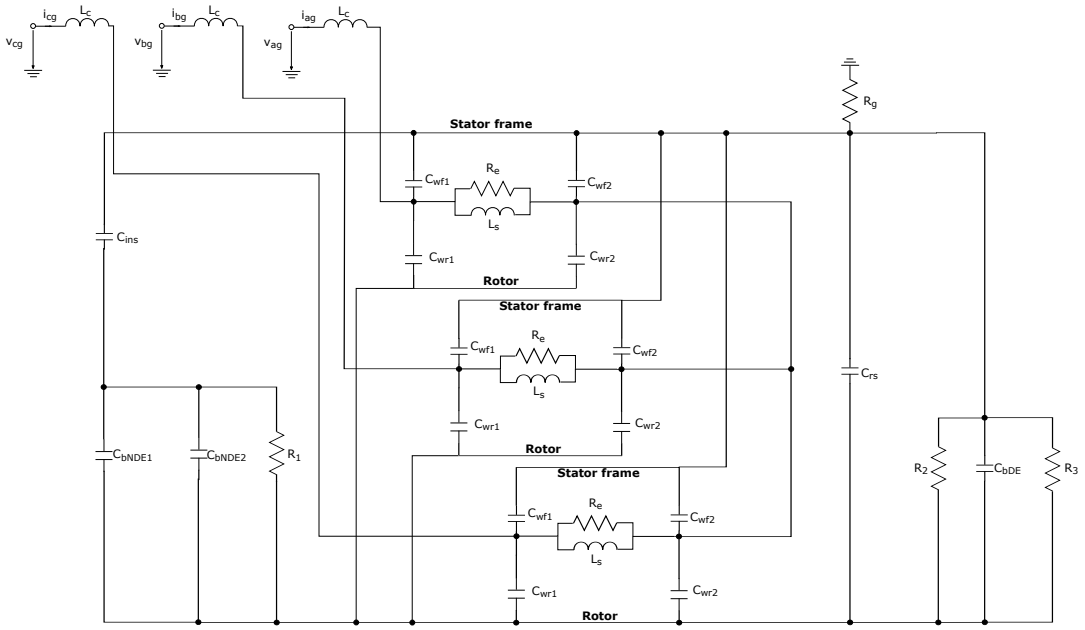

Figure 18: Three-phase high-frequency model for simulation with line-to-ground voltage inputs for phases a, b and c.

The model in Figure 18 is for one winding. However, the Azipod has two windings, and is fed by two drives. Finally, Figure 19 shows the complete equivalent circuit. The capacitance C_m (C_{m1} and C_{m2}) is the mutual coupling capacitance of the two windings, and it is assumed to be approximately the same in each connecting point. Since the Azipod is fed by two drives, the windings are fed with different voltage pulses that have a 30 degree phase difference. The reason for two different drives, with different pulses and a phase difference, is to provide redundancy in the system. These pulses are fed randomly, however, taking enough time from the measured line-to-ground voltages and inserting them into the simulation program will give sufficient accuracy in the outputs.

In the complete Azipod model of Figure 19 symbols are shown as they are in the simulation program. The letters "a", "b" and "c" indicate the phase and the numbers "1" and "2" the winding. The simulated model appears in Figure 40.

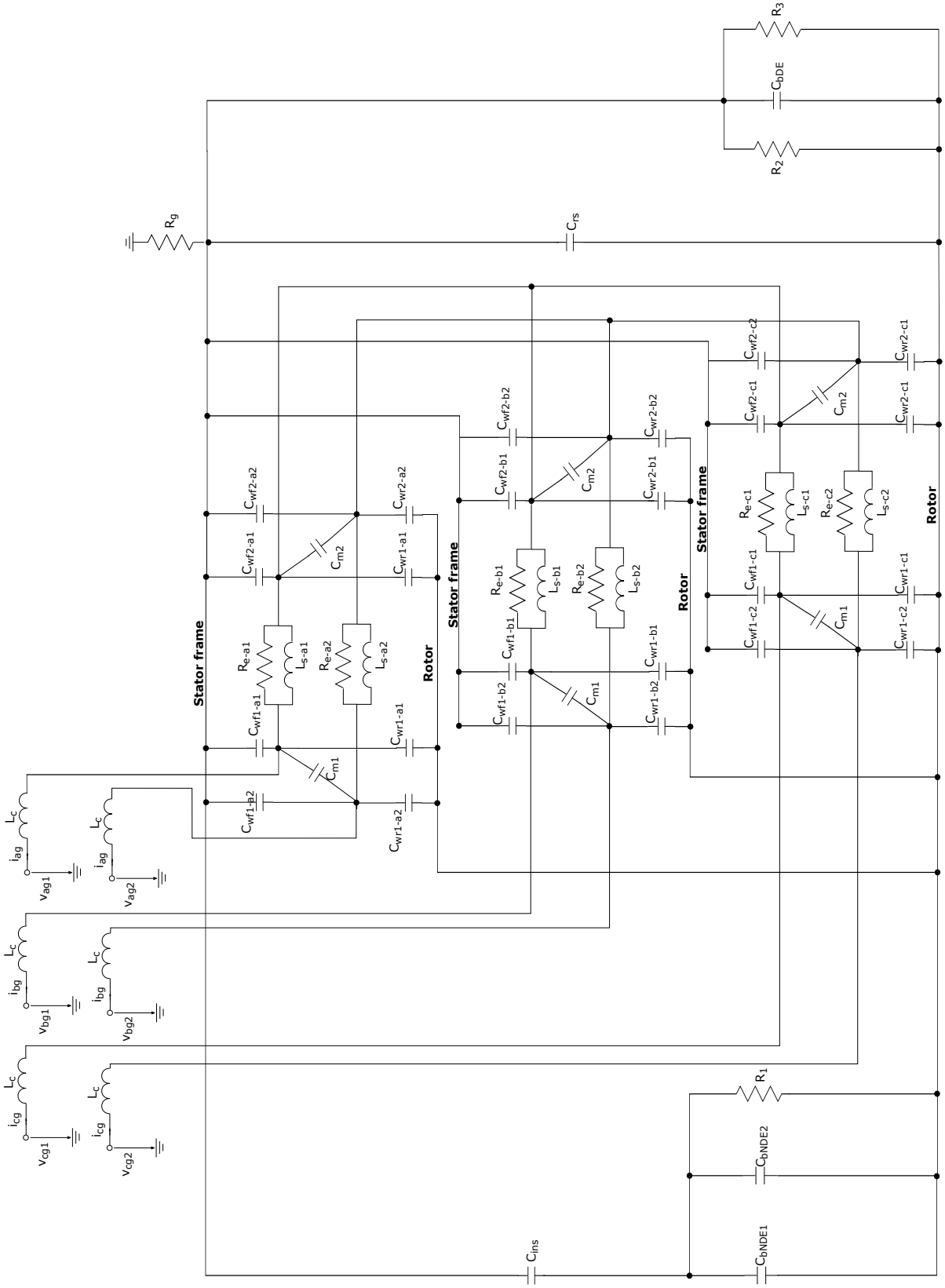

Figure 19: Complete three-phase high-frequency model with double winding.

5.2 Extraction of the parameters in the model

The following paragraphs present the methods to extract parameters from the differential- and common-mode impedance measurements of the stator windings. In addition, for the rest of the parameters, analytical methods to calculate these are discussed.

• Parameters extracted from common-mode impedance
The common-mode impedance measurement should produce the graph shown in Figure 20. The graph is a reference from the measured common-mode impedance of a 240 kW induction machine in [30]. The frequency response of the impedance of the stator windings will give important values in order to determine the parameters for the high-frequency model. Point 1 represents the first antiresonance frequency f_1. Thus the capacitances C_{wf} describe the motor behavior at lower frequencies (f_4) and C_{wf1} at higher frequencies (f_3).

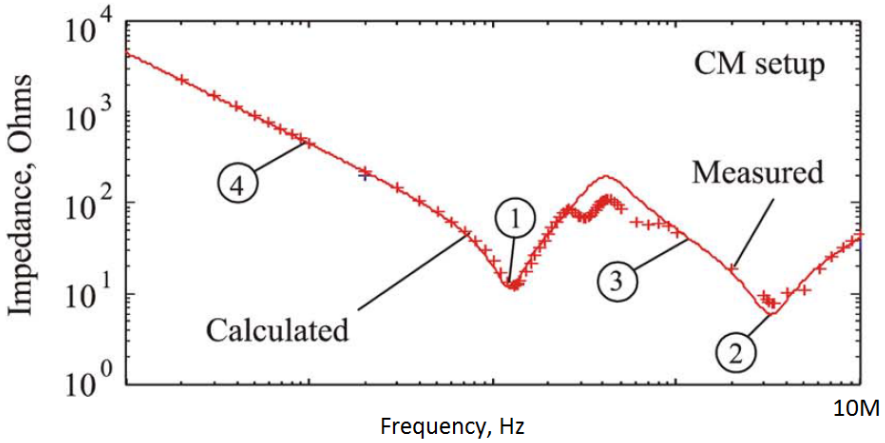

Figure 20: Measured common-mode impedance in [30].

With the help of the capacitance's reactance equation:

$$X_c = \frac{1}{2 \cdot \pi \cdot f \cdot C}, \tag{17}$$

the stator winding-to-frame capacitance per phase can be extracted from the following equation:

$$C_{wf} = \frac{1}{3} \cdot \frac{1}{2 \cdot \pi \cdot f_4 \cdot Z_{CM,4}}, \tag{18}$$

where $Z_{CM,4}$ is the common-mode impedance at frequency f_4. The capacitance is in farads (F). The winding-to-frame capacitance at frequency point 3 is

$$C_{wf1} = \frac{1}{3} \cdot \frac{1}{2 \cdot \pi \cdot f_3 \cdot Z_{CM,3}}, \tag{19}$$

where $Z_{CM,3}$ is the common-mode impedance at frequency f_3. Since

$$\begin{aligned} C_{wf} &= C_{wf1} + C_{wf2} \\ \Rightarrow C_{wf2} &= C_{wf} - C_{wf1}. \end{aligned} \tag{20}$$

The stator-winding inductance can be calculated as follows:

$$L_s = \frac{1}{4 \cdot \pi^2 \cdot f_1^2 \cdot (C_{wf1} + C_{wf2})}. \tag{21}$$

The inductance is in henrys (H).

The additional loss resistance is given by the formula:

$$R_g = 3 \cdot Z_{CM,2}, \tag{22}$$

where $Z_{CM,2}$ is the minimum impedance. [30] [32]

• Parameters extracted from differential-mode impedance

The differential-mode impedance measurement should produce the graph shown in Figure 21. This measurement gives the eddy current loss resistance R_e, and the feeding cable inductance L_c. Point "B" is the maximum impedance point and point "A" is the minimum impedance.

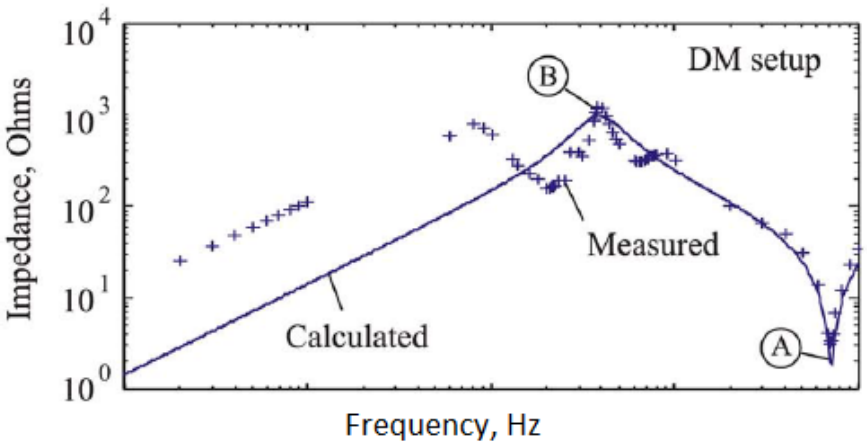

Figure 21: Measured differential-mode impedance in [30].

Eddy current loss resistance can be calculated with the following equation:

$$R_e = \frac{2}{3} \cdot Z_{DM,max}, \tag{23}$$

where $Z_{DM,max}$ is the maximum impedance (impedance at point "B").

The motor internal feed conductors and connector inductance is given by:

$$L_c = \frac{2}{3} \cdot \left(\frac{3}{8 \cdot \pi^2 \cdot f_{min}^2 \cdot C_{wf1}} - L_{cable}\right), \tag{24}$$

where f_{min} is the frequency at the lowest resonant point and L_{cable} is the inductance of the measuring cable. [30] [32]

• **Stator winding-to-rotor capacitance** C_{wr}
The stator winding-to-rotor capacitance C_{wr}, initially presented in Figure 7, can be calculated analytically by approximating C_{wr} as a parallel-plate capacitor and having Q_s (number of stator slots) plate capacitors in parallel [33]. The plate capacitor can be calculated by the following equation:

$$C = \frac{\epsilon \cdot A}{d}, \tag{25}$$

where ϵ ($\epsilon = \epsilon_r \cdot \epsilon_0$) is the permittivity of the insulating materials, A is the area of the plates and d is the distance between the two plates [34, p. 30]. A relative permittivity $\epsilon_r \approx 3$ of winding insulation is often used in the literature and would be a good approximation in this application. The distance d consists of two parts each having different permittivities, thus different capacitances. The first part is the air gap and the height of the slot opening, forming a capacitance (C_{wr-air}). The second part is the height of both the slot wedge and windings slot insulation (including the wire insulation), forming a capacitance (C_{wr-ins}). Thus, the capacitance C_{wr} is C_{wr-air} and C_{wr-ins} in series having Q_s branches in parallel:

$$C_{wr} = Q_s \cdot \frac{C_{wr-ins} \cdot C_{wr-air}}{C_{wr-ins} + C_{wr-air}} = \frac{Q_s}{\frac{1}{C_{wr-air}} + \frac{1}{C_{wr-ins}}} = \frac{1}{\frac{1}{Q_s} \cdot (\frac{1}{C_{wr-air}} + \frac{1}{C_{wr-ins}})}. \tag{26}$$

We can define C_{wr-air} and C_{wr-ins} by using the equation 25, and we get:

$$C_{wr-air} = \frac{\epsilon_{r0} \cdot \epsilon_0 \cdot w_{slot} \cdot l_{stack}}{\delta + h_{slot}}, \tag{27}$$

where w_{slot} (shown in Figure 22) is the width of the slot opening, l_{stack} is the length of the stators lamination stack, δ is the air-gap and h_{slot} is the height of the slot opening, and

$$C_{wr-ins} = \frac{\epsilon_{r1} \cdot \epsilon_0 \cdot w_{slot} \cdot l_{stack}}{h_{wedge} + h_{ins}}, \tag{28}$$

where h_{wedge} is the height of the wedge and h_{ins} is the height of the windings insulation.

The slot consists of double windings separated by the spacer between the coils. Each winding consists of conductors that are separated by the conductor insulation. These are kept together by the main insulation. The slot consists also of the slot opening filler, slot wedge and a very small air-gap. In reality h_{wedge} and h_{ins} include the slot opening filler that is taken into account in the calculations. However, the same relative permittivity ($\epsilon_r \approx 3$) is used with the insulating materials.

Due to the separation of the winding-to-frame capacitance C_{wr} into C_{wr1} and C_{wr2}, we get:

$$C_{wr1} \approx k_{cap} \cdot C_{wr} \tag{29}$$

$$C_{wr2} \approx (1 - k_{cap}) \cdot C_{wr}, \tag{30}$$

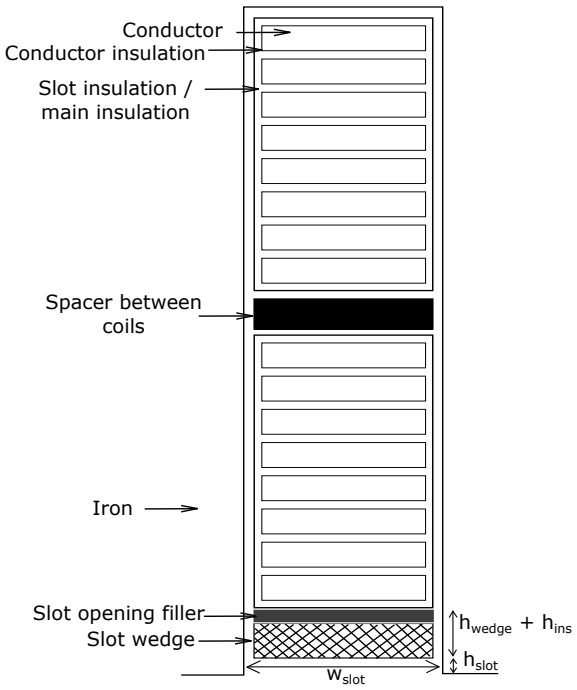

Figure 22: Sketch of a cross-section of the synchronous motor's windings slot.

where the coefficient (from [30]) is:

$$k_{cap} = \frac{C_{wf1}}{C_{wf}}. \tag{31}$$

• **Rotor-to-frame capacitance** C_{rs}

The rotor and the stator have similar geometries as a coaxial cable. Thus, the rotor-to-frame capacitance C_{rs} can be calculated analytically by approximating C_{rs} as a cylindrical capacitor [33]. The cylindrical capacitor is calculated by the equation:

$$C = \frac{2 \cdot \pi \cdot \epsilon \cdot L}{\ln(b/a)}, \tag{32}$$

where L is the length of the cylinder ($L = l_{stack}$), a is the inside radius and b the outside radius [35, p. 80]. Let say d_{stator} is the diameter of stator's inner surface and d_{rotor} is the outer diameter of the rotor. Then d_{stator} equals d_{rotor} plus two times the air gap δ. The cylindrical capacitor becomes:

$$C_{rs} = \frac{2 \cdot \pi \cdot \epsilon_r \cdot \epsilon_0 \cdot l_{stack}}{\ln(d_{stator}/d_{rotor})} = \frac{2 \cdot \pi \cdot \epsilon_r \cdot \epsilon_0 \cdot l_{stack}}{\ln[(d_{rotor} + 2 \cdot \delta)/d_{rotor}]} = \frac{2 \cdot \pi \cdot \epsilon_r \cdot \epsilon_0 \cdot l_{stack}}{\ln(1 + 2 \cdot \delta/d_{rotor})}. \tag{33}$$

However, here the distance δ from the rotor to the stator frame is not uniform due to the slots. In reality, the air gap δ is longer than its physical measure. Thus, in the formula, δ should be multiplied by the so called Carter factor $k_c > 1$. Since the

rotor and the frame are separated only by air, $\epsilon_r = 1$ (the relative permittivity of air), the rotor-to-frame capacitance can be calculated as:

$$C_{rs} = \frac{2 \cdot \pi \cdot \epsilon_0 \cdot l_{stack}}{\ln(1 + 2 \cdot k_c \cdot \delta / d_{rotor})}. \tag{34}$$

• **Stator winding-to-frame capacitance** C_{wf}

It is reminded here, that when calculating or measuring the winding-to-frame capacitance C_{wf}, the phase-to-phase capacitance C_{ph} comes along. However, due to its negligible influence, we consider only the C_{wf} and, therefore, analytical calculation of C_{ph} is left out.

The stator winding-to-frame capacitance C_{wf} can be determined by measuring it directly with a RLC-meter [36] or analytically. In the latter method the C_{wf} is considered to be Q_s number of parallel plate capacitors. The stator is a wound coil consisting of insulation tape and high quality epoxy resin from the vacuum pressured impregnation.

The stator winding-to-frame capacitance is calculated as follows:

$$C_{wf} = F_c \cdot \epsilon_r \cdot \epsilon_0 \cdot Q_s \cdot \frac{U_{slot} \cdot l_{stack}}{d_{slot}}, \tag{35}$$

where F_c is form factor, ϵ_r is relative permittivity, ϵ_0 is permittivity of vacuum ($8.8522 \cdot 10^{-12}$ As/Vm), U_{slot} is circumference of stator slot, l_{stack} is the length of the stators lamination stack and d_{slot} is the thickness of the insulation in the slot (tape+resin). However, in this work the stator winding-to-frame capacitance is measured since the analytical calculation is difficult.

• **Feeding cable inductance** L_c

Finally, we get to the determination of the parameter L_c. Since we already have a value, no measurements for the feeding cable inductance were done. It is important to mention here, that the feeding cable is the cable from the output of the drive to the stator windings' inputs. The cable consists of six conductors. Each conductor has an inductance of 178 $\mu H/km$. The length of the cable is 10 m so the inductance of a conductor is 1.78 μH. In consequence, the total inductance L_c of parallel conductors is:

$$\frac{1}{L_c} = \frac{1}{L_1} + \frac{1}{L_2} + \frac{1}{L_3} + \frac{1}{L_4} + \frac{1}{L_5} + \frac{1}{L_6}. \tag{36}$$

The conductors are identical, so: $L_1 = L_2 = L_3 = L_4 = L_5 = L_6 = 1.78\ \mu H = L$. As a consequent, the upper equation becomes:

$$\frac{1}{L_c} = \frac{6}{L} \tag{37}$$

$$\Rightarrow L_c = \frac{L}{6} = \frac{1.78\ \mu H}{6} \tag{38}$$

$$\Rightarrow L_c = 0.297\ \mu H. \tag{39}$$

6 Measurements

The rest of the values, that were not calculated analytically, were measured. These measurements were carried out to determine the bearing shield impedance, and stator winding impedances. The bearing shield impedance measurement is not important for the simulation itself. However, it helped with the preparations of the measurements of the stator winding impedances. The challenges of the measurements were getting accustomed to the measurement device, finding the right equipment and acquiring the knowledge on how they might affect the results. In addition, the Azipod should be at the exact time in the assembly line resulting in a gap of around 24 hours for the measurements. The exact time for the stator winding impedance means that the Azipod is in a convenient position for access of the measurement probes without having the rotor and feeding cables assembled yet. In the stator winding measurements, the stator is fitted into the Azipod hull's cylindrical frame without the rotor inside the stator.

The impedance measurements were done at ABB Marine Vuosaari's assembly factory with a Hioki (Figure 23) L2000 4-terminal probe RLC-meter:

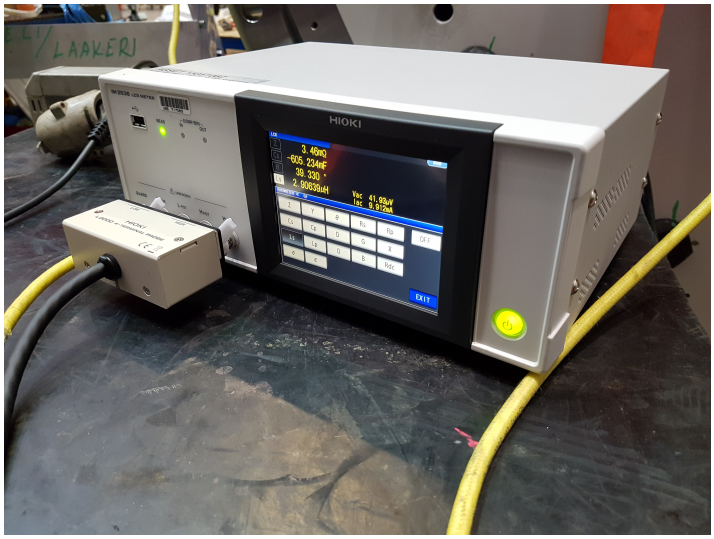

Figure 23: Hioki L2000 RLC-meter.

The Hioki RLC-meter prints the measured values of each setup to an excel file where they are plotted on a logarithmic graph. These graphs are shown in Figures 27-31.

6.1 Stator impedance measurements

The parameters (C_{wf1}, C_{wf2}, L_s, R_g, R_e and L_c) of the high-frequency model can be extracted from the differential- and common-mode impedance measurements of the motor phases [32]. Figure 24 shows the measurement setups for both types of measurements. In the common-mode impedance measurement, all three phases of the

winding are in parallel. Whereas in the differential-mode measurement two phases are connected in parallel, which are then in series with the third phase.

The measurements are done directly at the stator windings before the assembly of the feeding cables. Thus, the parameter L_c that describes the feeding cable inductance is not extracted from these measurements. However, this value of L_c was determined in the previous section. The Figure 25 shows the three phases of one winding, whereas Figure 26 shows both windings that form the stator of the synchronous machine. It is both easier and more accurate to directly measure the stator windings without the feeding cables.

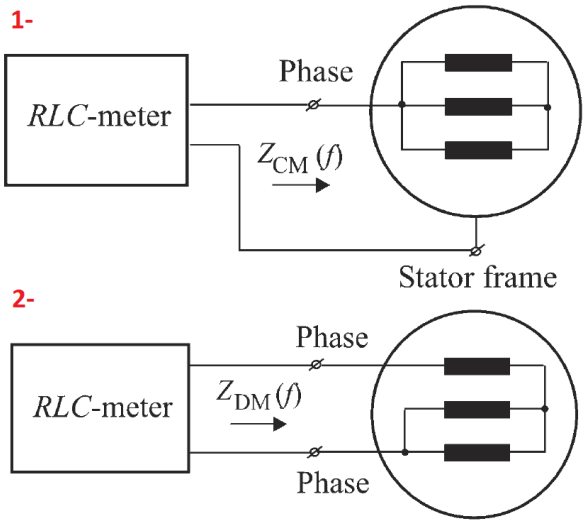

Figure 24: Impedance measurement setups for: 1- common-mode and 2- differential-mode. [30]

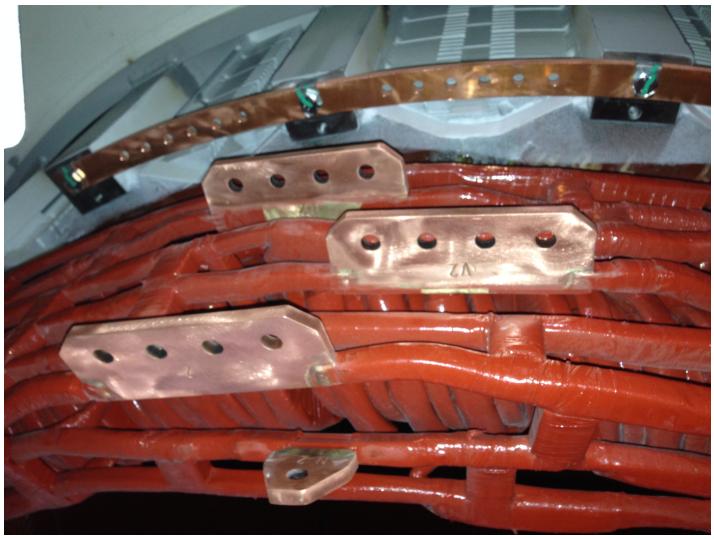

Figure 25: Three phases and star point of one winding.

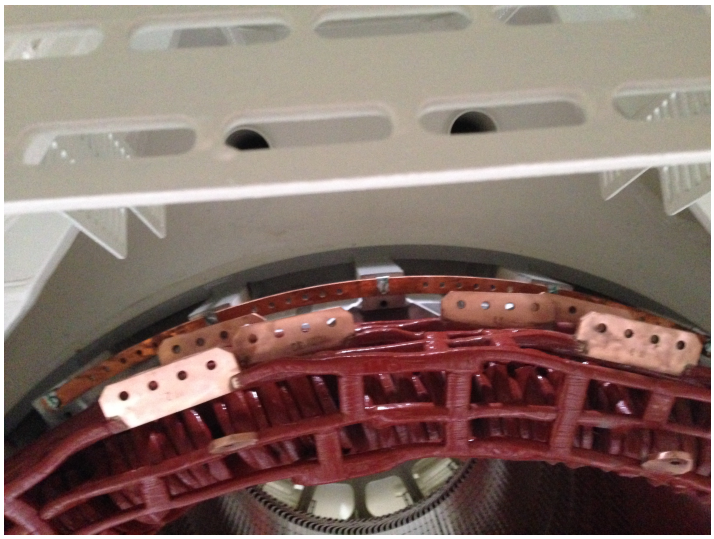

Figure 26: Complete winding configuration that is measured.

An open circuit and a short circuit compensation was done before each measurement. These compensations were carried out to minimize the effect of the parasitic capacitances from the measuring cables. In the open circuit compensations, the measuring cables were left "open" and as close as possible to the measuring points. On the other hand, in the short circuit compensations, the measuring cables were put "short" after which the compensation is carried out. The compensations were realized with the Hioki RLC-meter. Detailed pictures of the stator winding impedance measurements with the compensations are shown in Appendix A.

The next paragraphs show the plotted impedance responses of the measurements, and the extraction calculations of the desired values. The graphs of Figures 27-30

are similar to the impedance response curves of the 1400 kW induction motor in Appendix C. As a result, it is proved that the base model of the induction motors can also be used for synchronous motors.

- **Primary winding**

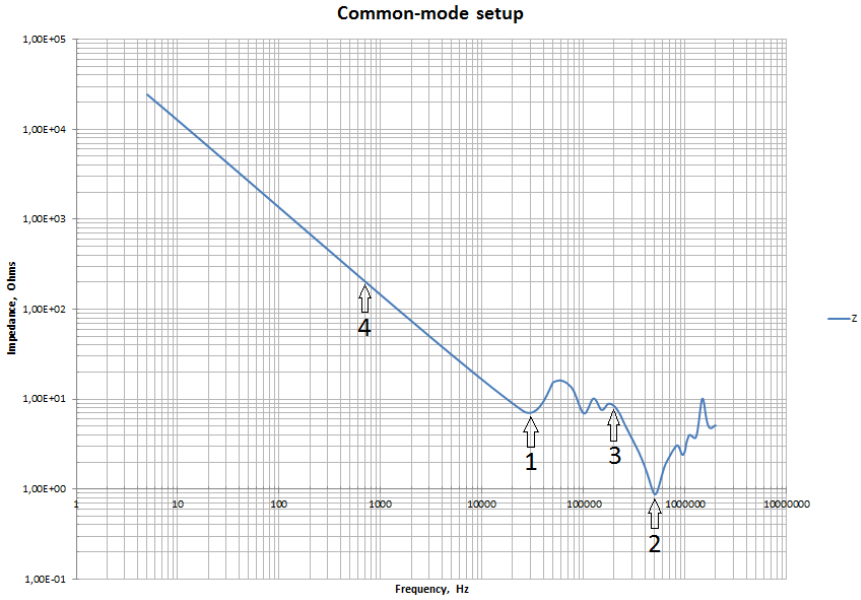

Figure 27: Measured common-mode impedance of the first winding.

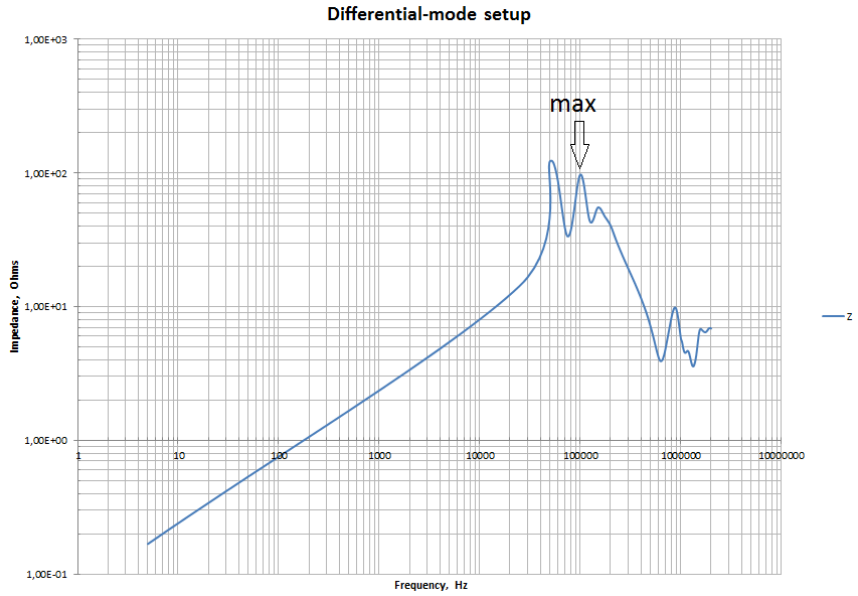

Figure 28: Measured differential-mode impedance of the first winding.

$$C_{wf} = \frac{1}{3} \times \frac{1}{2 \cdot \pi \cdot f_4 \cdot Z_{CM,4}} = \frac{1}{3} \times \frac{1}{2 \cdot \pi \cdot 700 \times 200} = 3.789 \times 10^{-7}\ F; \tag{40}$$

$$C_{wf1} = \frac{1}{3} \times \frac{1}{2 \cdot \pi \cdot f_3 \cdot Z_{CM,3}} = \frac{1}{3} \times \frac{1}{2 \cdot \pi \cdot 200000 \times 8.36369} = 3.172 \times 10^{-8}\ F = 31.72\ nF; \tag{41}$$

$$C_{wf2} = C_{wf} - C_{wf1} = 3.789 \cdot 10^{-7} - 3.172 \cdot 10^{-8} = 3.472 \times 10^{-7}\ F = 347.2\ nF; \tag{42}$$

$$k_{cap} = \frac{C_{wf1}}{C_{wf}} = \frac{3.172 \times 10^{-8}}{3.789 \times 10^{-7}} = 0.0837; \tag{43}$$

$$L_s = \frac{1}{4 \cdot \pi^2 \cdot f_1^2 \cdot (C_{wf1} + C_{wf2})} = \frac{1}{4 \cdot \pi^2 \cdot 30000^2 \cdot (3.172 \times 10^{-8} + 3.472 \times 10^{-7})} = 7.428 \times 10^{-5}\ H; \tag{44}$$

$$R_g = 3 \cdot Z_{CM,2} = 3 \times 0.981 = 2.943\ \Omega; \tag{45}$$

$$R_e = \frac{2}{3} \cdot Z_{DM,max} = \frac{2}{3} \times 97.18 = 64.79\ \Omega. \tag{46}$$

- **Secondary winding**

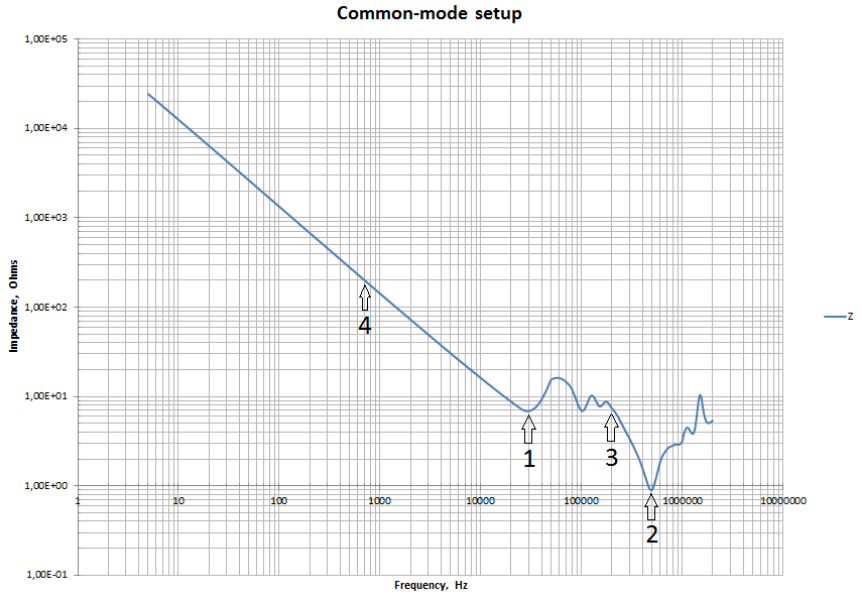

Figure 29: Measured common-mode impedance of the second winding.

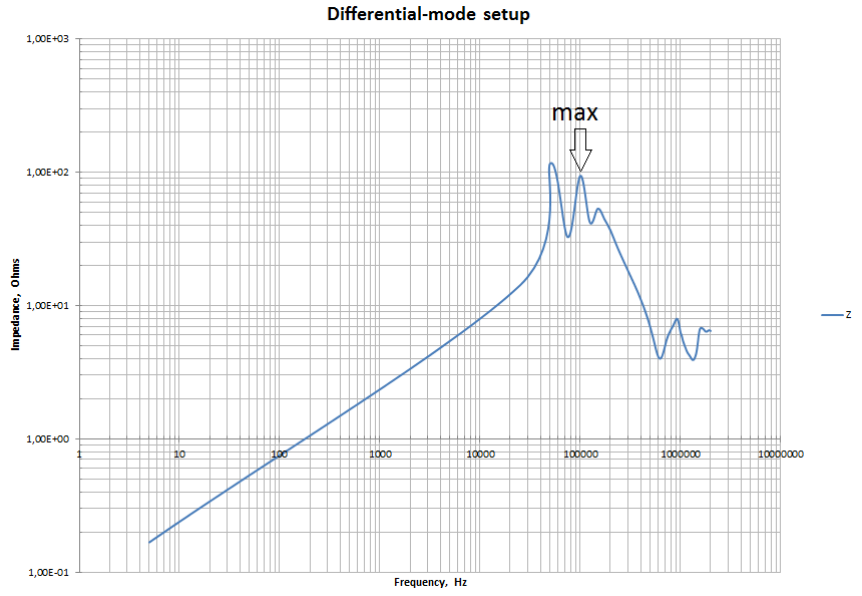

Figure 30: Measured differential-mode impedance of the second winding.

$$C_{wf} = \frac{1}{3} \times \frac{1}{2 \cdot \pi \cdot f_4 \cdot Z_{CM,4}} = \frac{1}{3} \times \frac{1}{2 \cdot \pi \cdot 700 \times 200} = 3.789 \times 10^{-7}\ F; \qquad (47)$$

$$C_{wf1} = \frac{1}{3} \times \frac{1}{2 \cdot \pi \cdot f_3 \cdot Z_{CM,3}} = \frac{1}{3} \times \frac{1}{2 \cdot \pi \cdot 200000 \times 7.31673} = 3.625 \times 10^{-8} F = 36.25\, nF; \tag{48}$$

$$C_{wf2} = C_{wf} - C_{wf1} = 3.789 \times 10^{-7} - 3.625 \times 10^{-8} = 3.426 \times 10^{-7} F = 342.6\, nF; \tag{49}$$

$$k_{cap} = \frac{C_{wf1}}{C_{wf}} = \frac{3.625 \times 10^{-8}}{3.789 \times 10^{-7}} = 0.0957; \tag{50}$$

$$L_s = \frac{1}{4 \cdot \pi^2 \cdot f_1^2 \cdot (C_{wf1} + C_{wf2})} = \frac{1}{4 \cdot \pi^2 \cdot 30000^2 \cdot (3.625 \times 10^{-8} + 3.426 \times 10^{-7})} = 7.429 \times 10^{-5}\ H; \tag{51}$$

$$R_g = 3 \cdot Z_{CM,2} = 3 \times 0.913 = 2.739\ \Omega; \tag{52}$$

$$R_e = \frac{2}{3} \cdot Z_{DM,max} = \frac{2}{3} \times 94.20 = 62.80\ \Omega. \tag{53}$$

- **Both windings**

This measurement is achieved by connecting one probe to the first phase U_1 of the first winding and the other probe to the first phase U_2 of the second winding. This way the impedance between the windings is measured giving the values of the mutual capacitances.

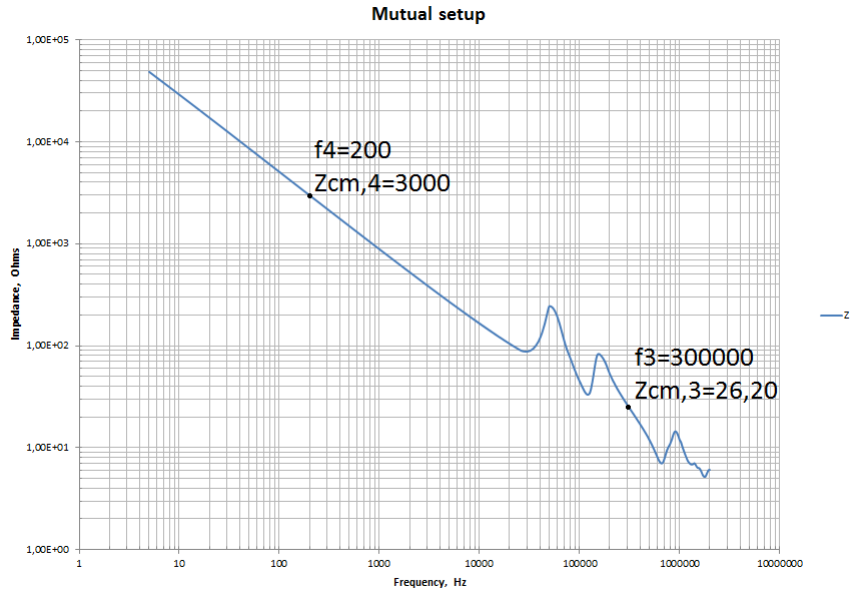

Figure 31: Measured impedance of the total stator winding.

The mutual capacitance C_m is calculated in a similar way as the winding-to-frame capacitance C_{wf}, but instead of dividing it by 3, it is divided by 6. This is because

there are a total of 6 phases. Consequently, the mutual capacitance C_m is:

$$C_m = \frac{1}{6} \times \frac{1}{2 \cdot \pi \cdot f_4 \cdot Z_{CM,4}} = \frac{1}{6} \times \frac{1}{2 \cdot \pi \cdot 200 \times 3000} = 4.421 \times 10^{-8}\ F; \quad (54)$$

$$C_{m1} = \frac{1}{6} \times \frac{1}{2 \cdot \pi \cdot f_3 \cdot Z_{CM,3}} = \frac{1}{6} \times \frac{1}{2 \cdot \pi \cdot 300000 \times 26.2} = 3.375 \times 10^{-9}\ F; \quad (55)$$

$$C_{m2} = C_m - C_{m1} = 4.421 \times 10^{-8} - 3.375 \times 10^{-9} = 4.084 \times 10^{-8}\ F. \quad (56)$$

6.2 Thrust bearing impedance measurements

Measurements of the thrust bearing (Figure 32) were the first measurements, and were carried out to get accustomed to the setups and to find the critical measuring equipment and positions. In addition, the values obtained here can be used to calculate the capacitance of the bearing shield insulation if the impedance from the outside of the insulation to the shaft is measured. The measurements were done with the RLC-meter by setting one measuring pin to the metal ring, and the other pin to the shaft with the help of bolts. Contact points were cleaned and bolts tightened in order to have the most optimal electrical contact. Earthing brushes were not assembled yet to obtain the impedance values without them, since the brushes naturally have a low resistance which would affect the results.

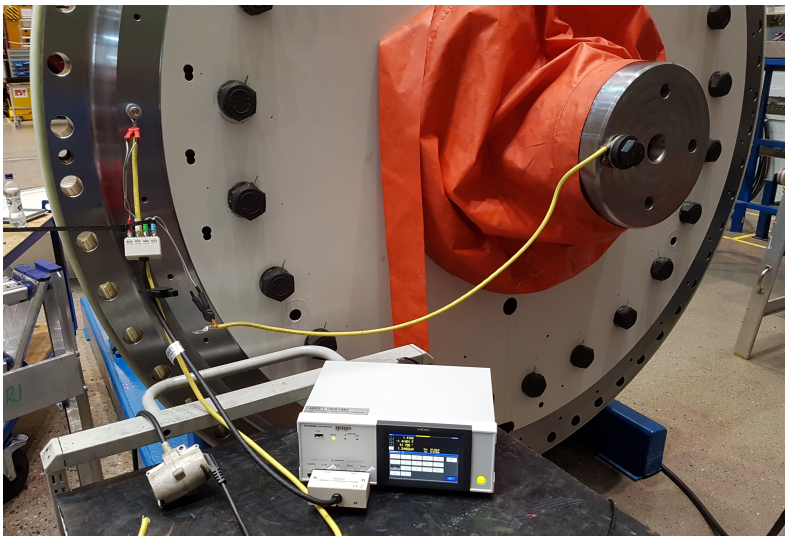

Figure 32: Measuring the impedance of the thrust bearing.

The first measurement was achieved at 120 Hz and the impedance was 3.46 mΩ with a capacitance of 603 mF. The display gives two capacitances: C_s (equivalent series capacitance) and C_p (equivalent parallel capacitance). This work uses the values of the equivalent series capacitance, which is the default setting of the device. Since Hioki's probes were too short to be used alone, extra connectors (yellow connector in Figure 34) were added on both sides. In the second measurement, one extra

connector was left out and the new value of the impedance with the same frequency was 1.75 mΩ with a capacitance of 1.1 F. We realized that it is essential to have long connecting probes in order to minimize the error in this matter. This way there would be no need to make any extra connections with random cables just to reach the measuring objects. The error might be considerable with higher frequencies when the inductance of the cables increase. The third measurement was a sweep from 5 Hz to 8 MHz with the same setup. The impedance values changed linearly from 1.42 mΩ to 68.7 Ω. Capacitance values were more extreme, varying nonlinearly from 193 F to 290 pF.

The impedance value is therefore highly dependent on the metal that is being measured, and on the frequency. At small frequencies the current penetrates the metal normally, whereas at higher frequencies, skin effect affects the material and increases the resistance of the metal. It is expected that the small resistance of the brushes would decrease the impedance of the system.

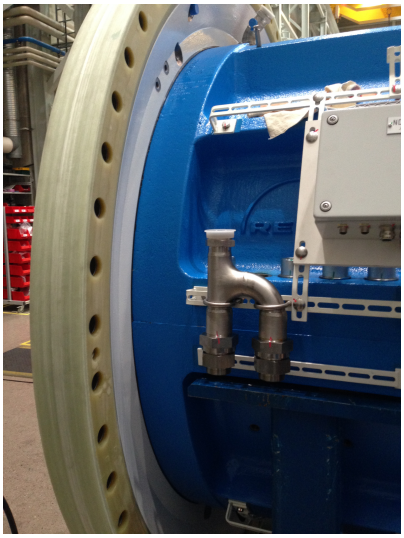

Figure 33: Thrust bearing system with insulation, radial bearing and slide thrust bearing.

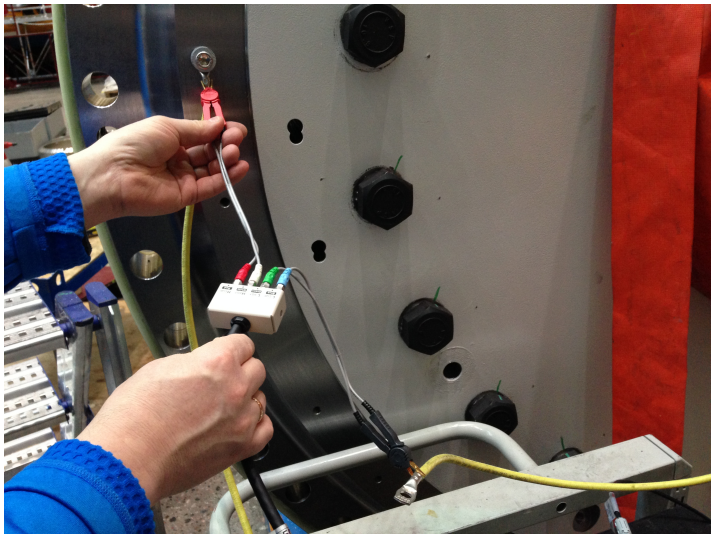

Figure 34: Connections to the bearing (one extra connector left out).

7 Simulations

The aim of the simulations is to find the role and importance of the bearing shield insulation and the earthing brushes. Moreover, with the simulations we can study the interdependence of the insulation and the earthing brushes on the bearing current and voltage. This is carried out by calculating the capacitive bearing voltage with different parameters using a simulation program. We can compare the graph of the worst case, when the insulation and brushes are not working, to the case where everything is expected to work. Additionally, combinations such as insulation not working with functioning brushes or vice versa can be simulated. The simulations were performed with OrCAD Capture CIS program.

7.1 Testing the program parameters

Before creating a simulation model for the Azipod, the model presented in [30] was tested. The model has simulation outputs for several machines and their predefined parameters. Testing a model used in a previous research and proving it to work gives confidence in proceeding with the Azipod model, which is more complicated. The test was conducted with a 240 kW (the highest power within the research) induction motor high-frequency model. The simulations targeted the model's common-mode current and bearing voltages. However, we did not have premeasured input voltages that were used in [30] so we had to create in the program a simulated input of line-to-ground voltages. Nevertheless, in the Azipod simulations we have measured input voltages, which are presented in the next subsection.

First we tested the per phase model of Figure 35 with single line-to-ground voltage to simulate the bearing voltages. Voltage differential probes are set in the DE and NDE bearings to get the traces of both. The output differed from the one obtained in [30]. The bearing voltage lacked the "increasing" transient effect of the other two phases of line-to-ground voltages. In Figure 36 the bearing voltage in the time domain is given. The input is a pulse voltage that simulates the measured line-to-ground voltage. On the other hand, the bearing voltage rises to a certain maximum and stays there until the input voltage changes its sign. After this the bearing voltage damps to zero, which is an unwanted result.

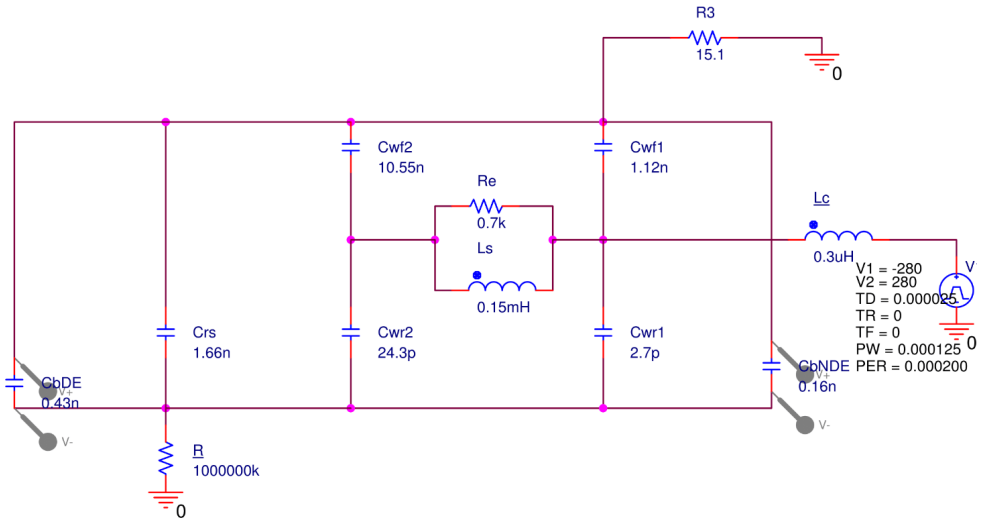

Figure 35: Per phase circuit with values given in the model of 240 kW induction motor.

In the model of Figure 35 there is an extra resistor R added that is connected to the circuit from the rotor on one side, and connected to the ground on the other side. Although in reality the circuit is correct without the added resistor, in the simulation program it gives a "node is floating" error. Adding a very large resistor to the floating point and grounding the node will cancel the error. Not any resistor can prevent this error. A large value resistor will prevent the current from flowing from the resistor to ground or will inflate the simulation, but not affect the output appreciably. One other way to get rid of the error is to add a very large resistor in parallel with the floating node. However, it is seen as more correct to do it in the way it is done in the model of Figure 35. This large resistor is present in all the following simulation models.

Before we proceed to the changes made to get better results, it is important to know what inputs to use and how they are implemented in the simulation program. The VPULSE source of OrCAD has several parameters that are:

- V1= the starting level of the voltage pulse
- V2= the voltage level where it changes from V1
- TD= the time delay before the pulses are started
- TR= the length of time that it takes to ramp the voltage of the pulse from V1 to V2 (rise time)
- TF= the length of time that it takes to incline the voltage from V2 to V1 (fall time)
- PW= the length of time that the pulse voltage is equal to V2

- PER= the length of time of the period of a continuous output of pulses

However, in the Azipod simulation's text file, line-to-ground voltage inputs of measured sailing vessel will be used. In OrCAD it is a source block nominated VPWL_FILE. These real inputs will give the transient effects that otherwise would be very difficult to implement in pulse inputs used here. The transient effect gives different curves as will be shown later in this work.

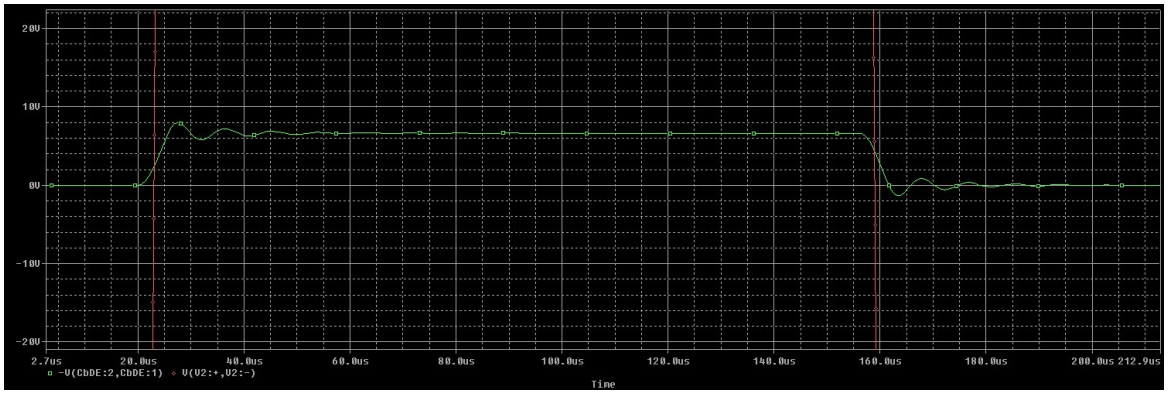

Figure 36: Simulated bearing voltage with one line-to-ground voltage as an input.

Creating a new model for the simulation with all three phases (Figure 37) will give a different bearing voltage. Each phase has its own pulse voltage, which are identical but have a different time delay TD (Figure 38). The output of this model is given in Figure 39. This is the wanted output since all the phases give an increasing effect in the bearing voltage trace when they are positive. However, in reality the bearing voltage should go from -10 V to +10 V. To get this, the input voltages of the simulation model should be modified. In this simulation, the bearing voltage is zero when the input voltages are -280 V, which means that v_b never reaches negative. To overcome this problem, the inputs should start from zero, and then switch between +280 V and -280 V. Nevertheless, this would require further investigation of the simulation problem since it requires three level input. This is not a problem in the Azipod simulations since the used input is the file (real measurements) instead of the pulse voltage.

Apart from the added resistor R that is mentioned earlier, shunt resistances R_4 and R_5 are added in series with the voltage sources V_{bg} and V_{cg}. This is because the program does not accept a loop that contains only a source and a coil. The values of the added resistances are kept very small in order to have a minimal effect on the simulation. These shunt resistances are also part of the following Azipod simulations.

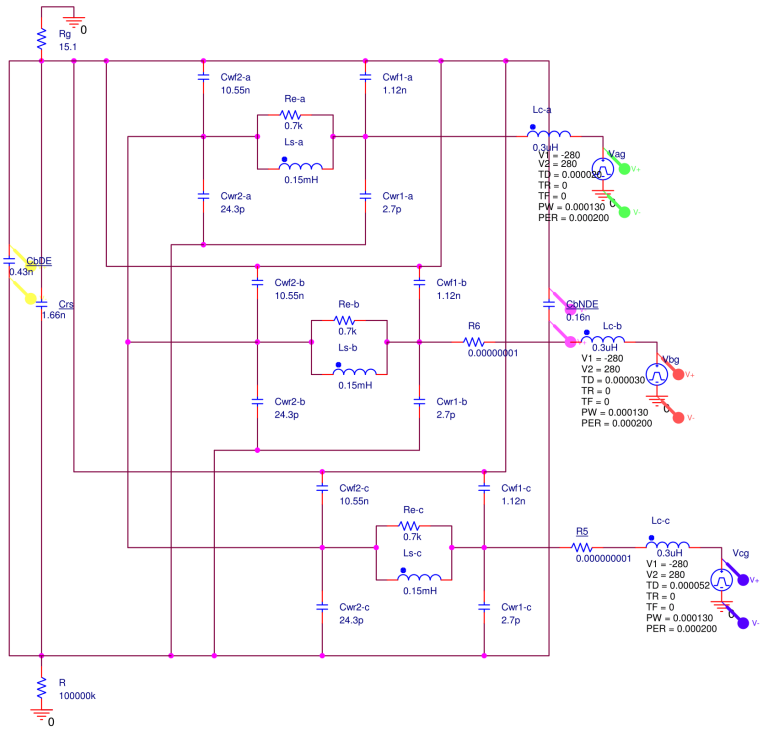

Figure 37: Three-phase model of the tested motor.

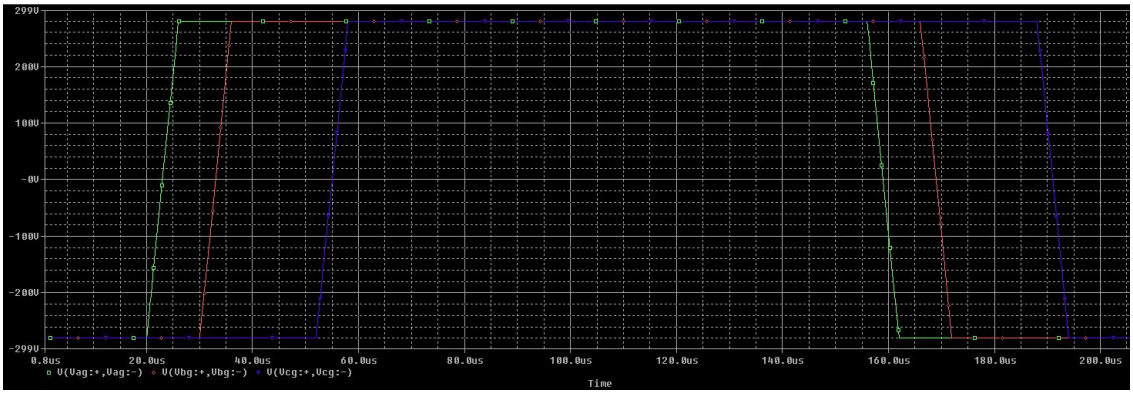

Figure 38: Plotted three-phase input voltages.

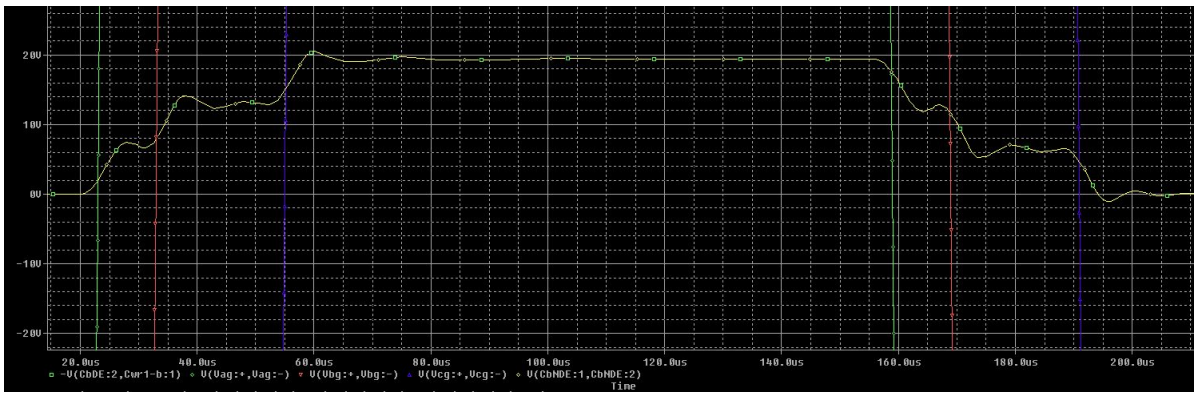

Figure 39: Simulated bearing voltage with line-to-ground voltages as inputs.

7.2 Simulations of Azipod model

The earthing brushes R_1 and R_2, the auxiliary resistance R_3 of the propeller, the capacitance C_{ins} of the bearing shield insulation, and the capacitance C_{bNDE2} of the slide thrust bearing are added to the model presented in subsection 7.1. This is the model presented in Figure 19. Figure 40 for instance, shows how the model looks in the simulation program. The figure might be slightly unclear, but the main point is to get familiar with the placements of the different components in the program. Moreover, understanding the model provides a good reference for future studies.

Since no value for the propeller resistance was determined and since it is assumed no currents flow through the propeller, the auxiliary resistance R_3 was left out from the simulations. However, one can refer to Figure 19 if the current flow through the propeller is examined in the future. The resistance R_3 is determined as one resistance for clarity, although in reality modeling the propeller side could be more complex.

The measured voltages were from a sailing cruise ship. The voltage is line-to-line and is 2800 VAC. Stator current is 100 % and is 3740/2 A = 1870 A for one stator. The stators are 30 degrees phase shifted. The switching frequency of the drive is on average between 200 Hz and 300 Hz. For maximum current the switching frequency is around 200 Hz.

The inputs used in the simulations were taken from two random time windows. One is shorter and the latter is longer. The first input is from 3.95175 s to 4.15175 s and the second input is from 8.765 s to 9.265 s. Figure 41 shows the longer input for one phase. Consequently, Figure 42 shows inputs of all six phases. The input data were opened with Yokogawa's Xviewer program, and Figure 41 and Figure 42 are screenshots from a chosen time window. From this program are extracted the inputs to a ".csv" file, which then is converted to a ".txt" file. Finally, this text file is the right format for the inputs used in the simulation program OrCAD. In the test model of the previous subsection the inputs were pulse voltages, whereas the inputs used here are real line-to-ground voltages. This change will improve the accuracy of the system drastically and will give more precise results.

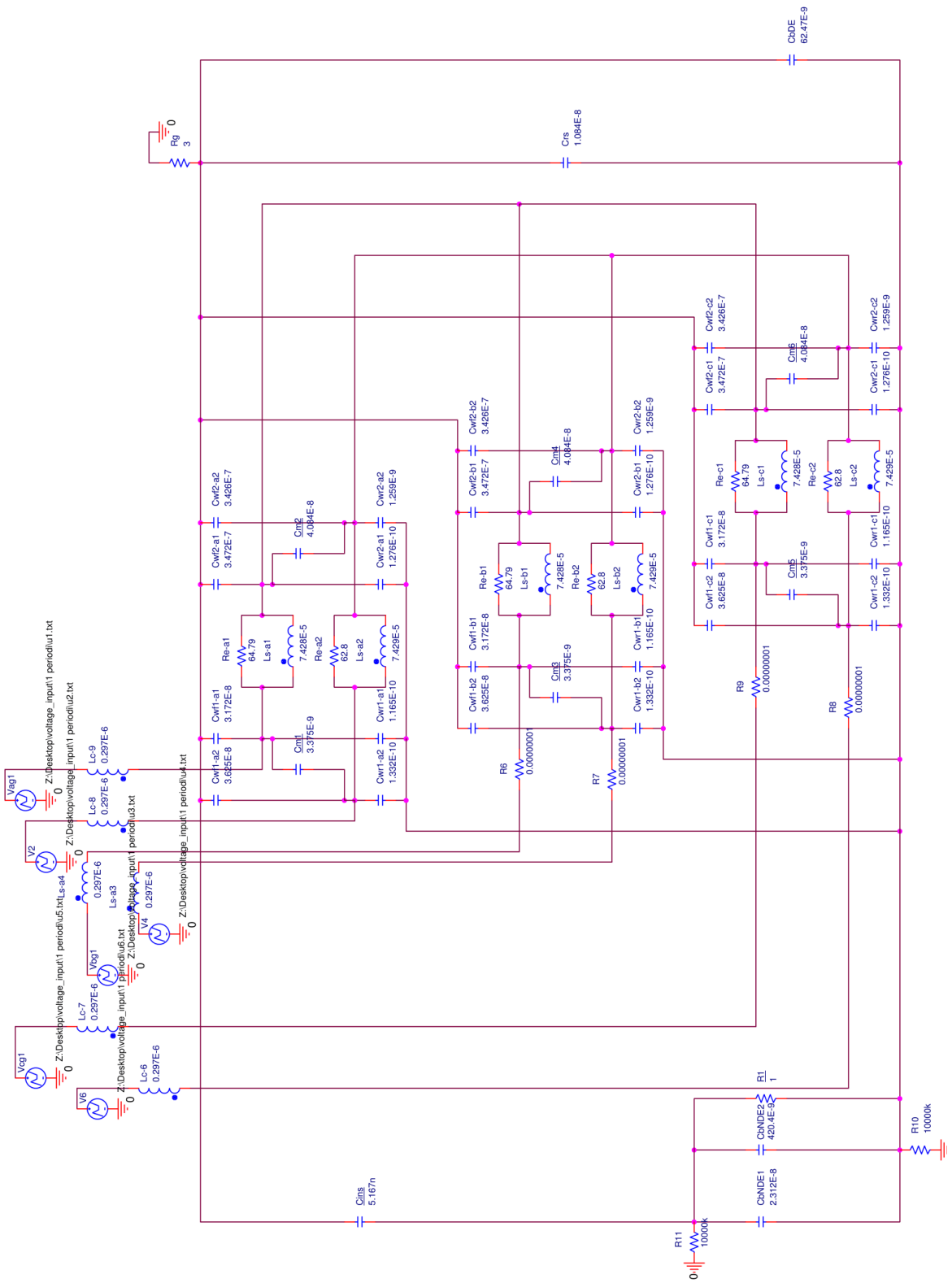

Figure 40: Complete model from OrCAD.

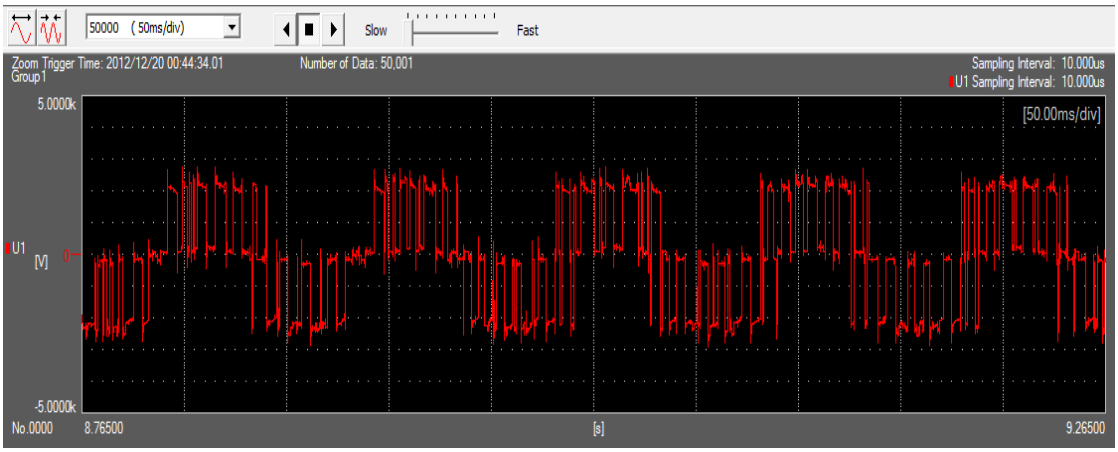

Figure 41: This is how the input line-to-ground voltage looks for one phase. It is the input from 8.765 s to 9.265 s.

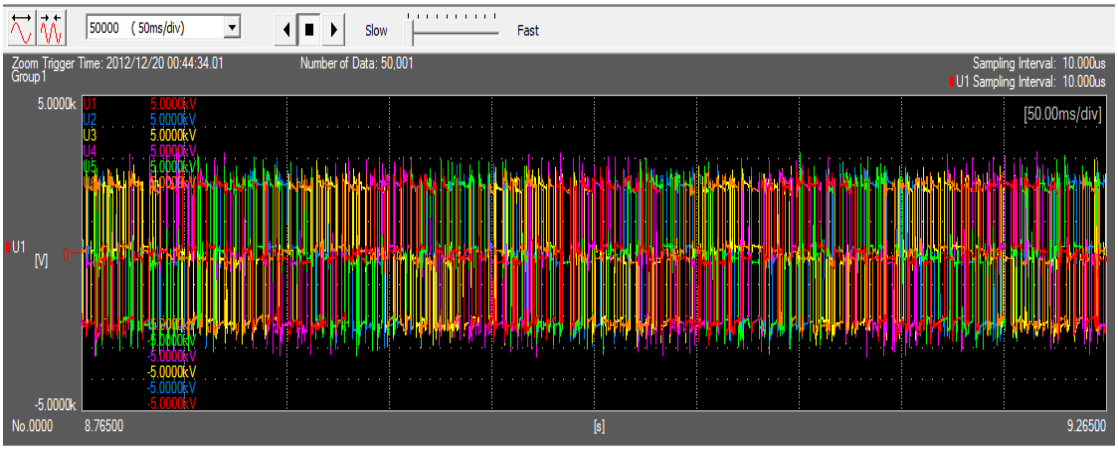

Figure 42: This is how the input line-to-ground voltages look for all six phases. They are the inputs from 8.765 s to 9.265 s.

No sensitivity analysis or any loop simulations were carried out since the simulations were achieved with a few predefined parameters. Figure 43 illustrates the simulation settings. The first inputs were set as in the figure and the second inputs started at 8.76 s and ended at 9.28 s.

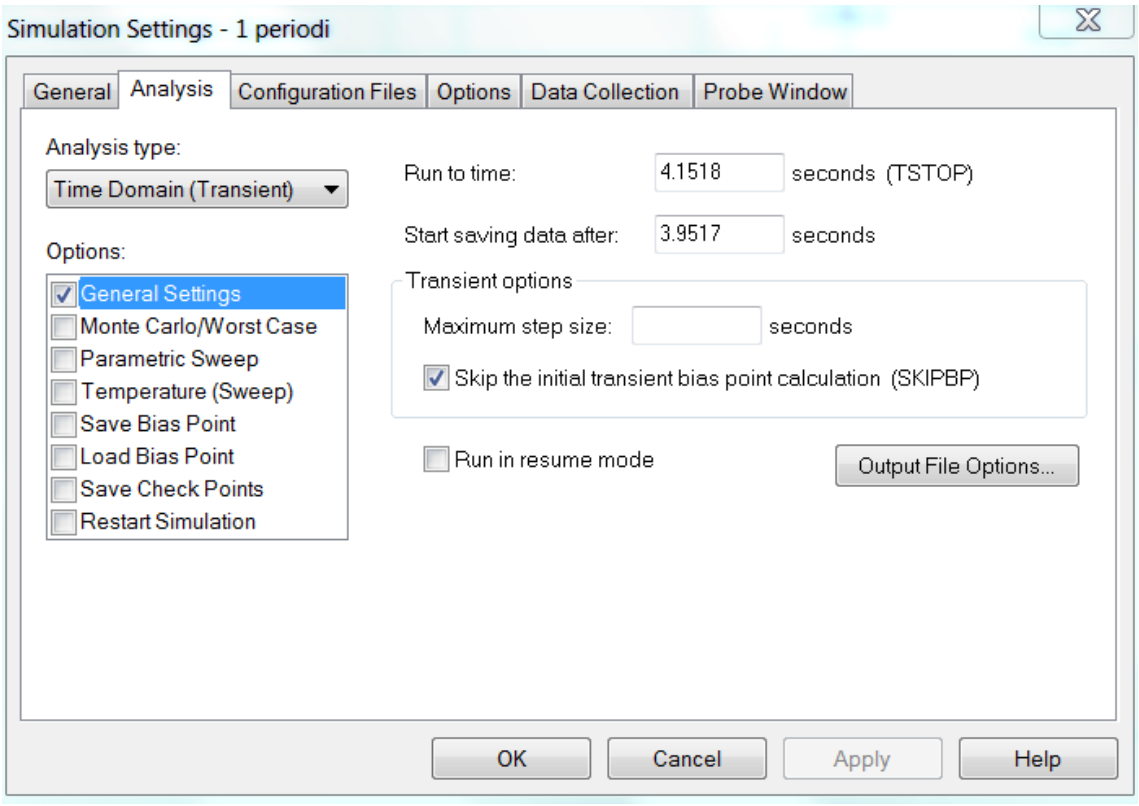

Figure 43: Simulation profile in OrCAD.

In the scenario when the insulation is working, it is C_{ins} in the model and is in series with the thrust bearings. On the contrary, when the insulation is not working, the bearing shield is conducting and C_{ins} is replaced by a short circuit. On the other hand, when the brushes are working, they are in parallel with the bearings and have resistances R_1 and R_2. When the brushes are not working, they do not conduct and are represented as open circuits in the model. Consequently, we could think of these as "on" or "off" situations. For the insulation a value is calculated when the capacitance is directly weakened by 50 %, whilst the thrust brushes are either left out from the simulations or have a constant value. This means that no optimization of the brushes has been done in this work nor any simulation with in-between values. Nevertheless, as we are interested in the thrust side in this work, the propeller side brushes are left working in all the following scenarios from 1 to 5. Following are the simulation runs enumerated as:

1. Insulation working, brushes working (ideal case)
2. Insulation not working, brushes not working (realistic worst case)
3. Insulation working, brushes not working
4. Insulation not working, brushes working
5. Insulation weakened by 50 %, brushes not working.

It is important to note where the measuring probe is set in the model. Figure 44 illustrates the exact location of the probes in the model. All the currents (marked as "I") are individual values of each bearing. Thus, naturally it leads to lower values than measuring the entire bearing assembly. In the latter case, the probe would be set "up" next to the insulation measuring the sum of each thrust bearing. However, we are more interested in the individual currents than the summed one, that is why the probes are set in the way shown in Figure 44. In addition, since these bearings share common points, the voltage (marked as voltage difference: "V+" and "V-") over the radial bearing is the same as the voltage over the slide thrust bearing.

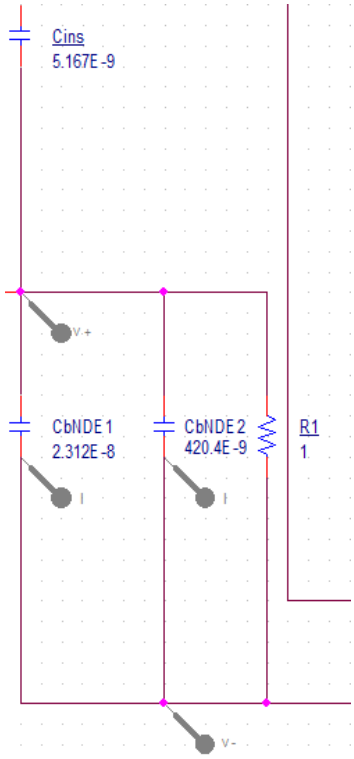

Figure 44: Caption of the NDE part of the model showing the locations of the measuring probes.

7.3 Simulation results of Azipod model

All the performed simulations are shown in Appendix D and Table 1 illustrates the results in a simple way in absolute maximum values. Table 1 is somewhat a summary of simulations and is created to help with the comparison of the different cases. Figures 45-47 are simulations outside the five cases. They show the worst case and the severity level when the bearing shield insulation, the thrust brushes and the propeller brushes are left out from the system. These figures are good references, as we can conclude that the bearings are destroyed if none of the protecting systems are used since the absolute bearing voltage is around 80 V. This voltage level is huge

and can destroy the bearings. Nevertheless, this problem is known in ABB and it is the reason why protective measures have been taken seriously.

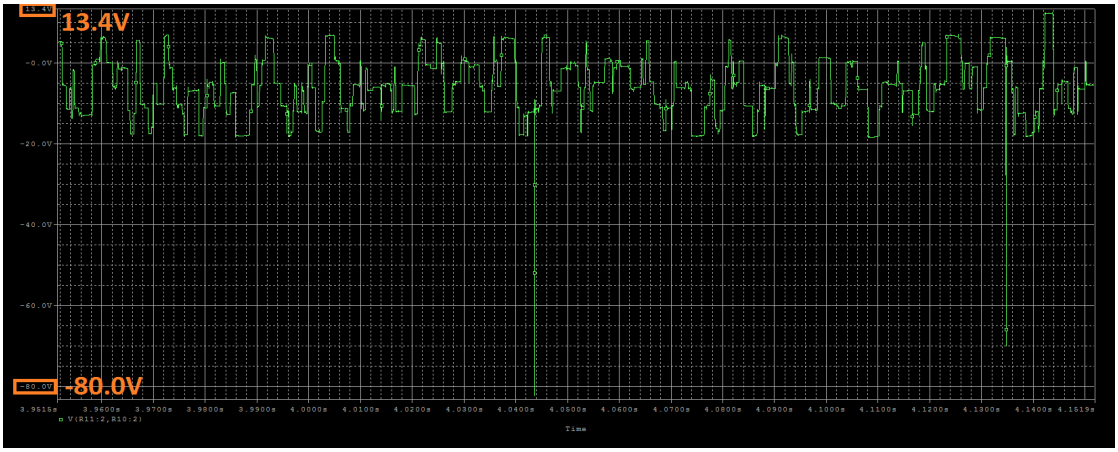

Figure 45: Bearing voltage when there is no bearing shield insulation and none of the brushes are working. Absolute maximum around 80 V.

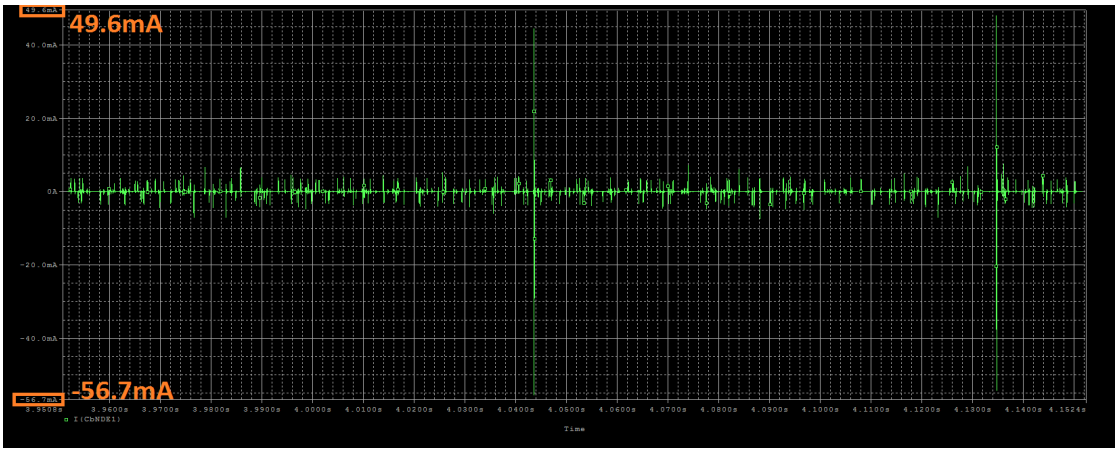

Figure 46: Bearing current when there is no bearing shield insulation and none of the brushes are working. Absolute maximum around 57 mA.

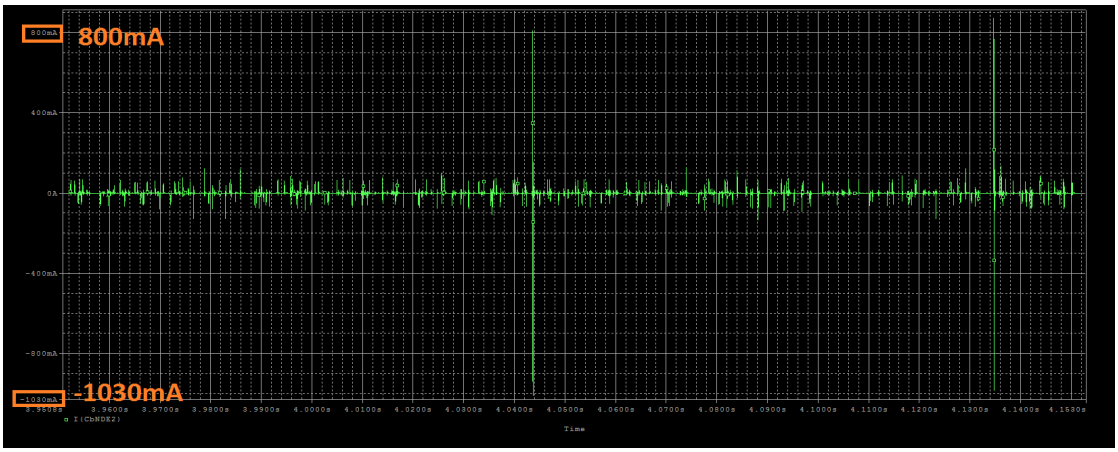

Figure 47: Bearing current when there is no bearing shield insulation and none of the brushes are working. Absolute maximum around 1.03 A.

Table 1: Absolute maximum values of the different simulated cases. First row shows the bearing voltages, second row shows the bearing currents of the radial bearing and third row shows the bearing currents of the slide thrust bearing.

Case 1	**Case 2**	**Case 3**	**Case 4**	**Case 5**
900 µV	1.25 V	16 mV	600 mV	20 mV
40 µA	4 mA	40 µA	1.93 mA	70 µA
766 µA	70 mA	766 µA	36 mA	1.2 mA

From Table 1 we can deduce the first case is the best in terms of voltage and current levels. It is the case when the insulation is present with all the brushes. This is an expected result. Case 3 follows, when the insulation is present, but the thrust side brushes are not. Then comes case 5 with insulation present but weakened, and thrust side brushes "off". After that case 4 follows, when insulation is not present, but all the brushes are. Finally the worst scenario between all these 5 cases comes up. It is the case 2, with insulation and thrust side brushes not present. This was also an expected result. However, this is better than the one shown in Figures 45-47 when even the propeller side brushes are not in the system. To summarize, here are the five cases in decreasing order: $1 < 3 < 5 < 4 < 2$.

Case 1 and 3 have a huge difference in voltage, but have the same current levels. This is an important observation, meaning that adding brushes in the thrust side seems to be lowering the voltage, but does not affect the bearing currents.

Cases 1, 3 and 5 have safe voltage and current levels. This means that if there is insulation, thrust side brushes can be taken off, or if they are left, then the insulation structure can be reduced by 50 %. However, since the calculation of the insulation is approximate, no optimal level of reduction is researched in this work.

Cases 2 and 4 seem to have dangerous levels of voltages and currents. This means,

that even though there are brushes, some kind of insulation should be in the system to protect the bearings. Nevertheless, this is a crucial consideration since according to these simulations the bearing voltage and current will not increase to dangerous levels even though the insulation is weakened.

Even though the simulation model is perfect with all the affecting components and parameters taken into account, it is hard to say which voltage and current level is safe. It is also hard to say which level is the limit, since the breakdown limits for these bearings are not defined. In addition, the bearings can withstand relatively high voltages for short periods. If the high peaks occur often and for long periods, they charge the lubrication film electrically, and if the threshold is exceeded, the bearings will be destroyed over time.

One other important conclusion from these simulations can be made. The current in the slide thrust bearing is higher than the current in the radial bearing. This is most probably the case also in any real measurements. This is good news, since it is assumed that the thrust bearing withstands higher currents. However, even with small currents, high voltages in the bearings can destroy radial bearings after the breakdown occurs. When a breakdown in the bearing occurs, the metal contacts start to conduct and the current is high in the bearing. This is the scenario when the bearing has lost its insulating properties and the bearing becomes resistive instead of being capacitive.

Although the inputs were from the same measurements, two different time windows were chosen for these simulations. Due to the large amount of measurement data, not everything was possible to include in the simulations. This is why the inputs were limited and short in time. Two time windows from different times with several periods were chosen to improve the accuracy of the simulations. Nevertheless, since the inverter switching technology is random, it is hard to say whether these inputs are enough to acquire all the unwanted peaks. Taking a longer time window will include more random transients and can lead to even higher peaks than obtained in these simulations. In this way new severity levels might be achieved.

In reality, the phenomenon is complicated and these values could be much higher. When doing bearing voltage and current measurements, many things that are assumed not to influence might finally affect the results. The model used in these simulations is simplified and is without the effect of the excitation machine that could increase the bearing voltages and/or currents. Moreover, if any of the thrust bearing outfittings' insulations break, it will give increased values in the real measurements. Furthermore, if the sailing boat has been operating for years, the bearing shield's insulation might be dirty and it will start to conduct. This dirtiness might lead to higher bearing currents.

Finally, if these values are compared to real measurements, they should be from the same conditions. The same conditions means that the bearing shield insulation with the outfittings insulations are perfect, shaft speeds are 120 rpm with the bearing's inner ring temperature being 70°C and the outer ring temperature being 10°C cooler. The bearing current measurements, if they are done and compared with the results in this work, should be done separately to each bearing in order to be appropriate for the comparison.

8 Assumptions and Future Suggestions

The Azipod propulsion is a complex three-phase system consisting of the power supply, the frequency drive, the feeding and the motor cables, and the synchronous motor. Including all the components and details would result in a large model. However, each of these components brings a contribution in the parasitic capacitances in the drive system and thus affects the common-mode phenomenon. The components and the common-mode impedance distribution of the whole system should be modeled as precisely as possible in order to have a good overall approximation for the common-mode phenomenon and shaft voltage values in the system. Furthermore, accurate information about the system states is needed for a complete description of the problem. The system is highly dependent on the frequency, for example, with increasing frequency, the cable resistance increases and inductance decreases. Therefore, no constant high-frequency values can be chosen since the impedance of the cable would be too high at low-frequencies.

Figure 48 shows the possible paths for the common-mode currents in the drive system of the Azipod. The common-mode impedance distribution of the total drive system of Figure 48 should be studied in order to have an adequate analysis for the common-mode phenomenon. The current i_1 is the common-mode current produced by the drive itself. A part of it never enters the motor terminals and flows via the cable's leakage capacitances. This leakage current is denoted as i_2 in the figure. The remaining current i_3 flows through the motor. These currents with the possible current i_{exc} from the excitation machine are summed up into i_4 in the protective earth conductor of the cable. Finally, i_5 is the current that flows via the parasitic capacitances between the drive's cabinet and DC link, and the rest of the current i_6 returns to the drive via the supply. [5]

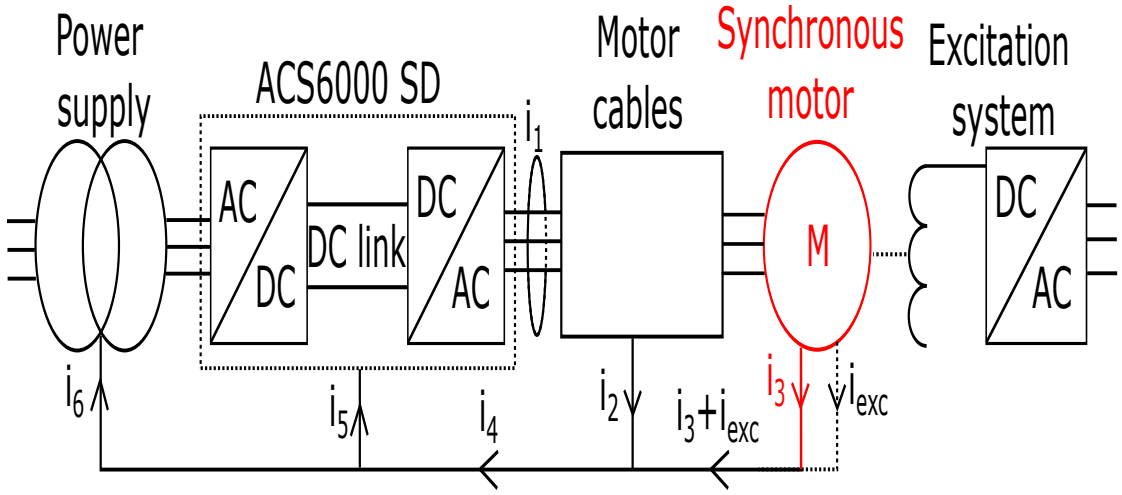

Figure 48: The possible paths of the common-mode currents.

8.1 Alternative approach

In this work the so called end-to-end shaft voltage was not studied. There is no model that can simultaneously be useful for determining the bearing current, the bearing voltage and the shaft voltage. Therefore, the shaft voltage is treated elsewhere. In [23], a model is presented that is suitable for the analysis of the bearing currents while taking into consideration both the capacitive and the induced shaft voltages. The model presented in [23] would provide a different perspective to the problem. However, since the model is different than the one presented in this work, a different approach is used and thus most values are determined differently.

8.2 For future works

This subsection presents a list of future suggestions that need clarification or more detailed research. The second list shows the assumptions used in this work. These suggestions can be done in ABB's research and development department with the help of a university such as Aalto University. Depending on the complexity level, these suggestions can be done as Bachelor's or Master's thesis or as Doctoral dissertation. There is plenty of help in the literature that can support these suggestions. However, some of them are very complex and needs doctoral level research. Below is the list:

- As mentioned earlier, no sensitivity analysis or loop simulations were carried out. This is essential to research in order to find other critical components that were not treated in this work.

- Bearing current and bearing voltage measurements should be performed on an Azipod moving in seawater. The same conditions (temperature, speed, load, etc.) as in this work should be achieved in order to compare the simulated values with the measured values. The measurements can also tell us if the model is correct. If the measured values differ from the simulated ones, deeper analysis is needed to find the reasons for the discrepancy. This suggestion also requires profound measurement planning since there is a risk of damaging the bearings if the measurement is not carried out properly. Measurement planning alone could be a separate topic. Added to these, proper measurement equipments should be purchased, such as high-frequency Rogowski coils. These coils should have the necessary bandwidth of several megahertz and an opening large enough to accommodate the desired measuring locations in the Azipod system.

- An improvement of the model presented in this work is necessary. The model presented here is good for analyzing bearing voltages and currents, however no research is done on the effect of the excitation machine. If it affects bearing currents or voltages, it should be added on the model. Additionally, a model should be created for the scenario if the insulations of the sensors on the thrust side break.

- Investigation into the insulation of parts that have contact with the bearing shield or shaft. These parts are, for example, pipings of the lubrication system, thermometers, etc. A study on the effect if the bearing shield insulation is bridged with these outfitting items in case such as break of insulation of these parts.

- This work focuses on the thrust side of the Azipod which means that no current is flowing through the propeller and to the seawater. Future works could investigate the presence of any currents flowing to the propeller. This can be done with measurements. Additionally, if a resistance value for the whole propeller side is obtained, it can be added to the model presented in Figure 19. In the model it is labeled as R_3.

- Deeper investigation on alternatives for the bearing shield insulation is recommended. Improvement solutions could include changing the material or the geometry of the insulation. In addition, investigations need to be made on the bearing shields that have been on operating Azipod systems for many years. A check on the condition of this insulation is crucial since if there is a large amount of dirt, it might start to conduct.

- Investigation on the effects of larger shaft brushing holders on shaft voltage, bearing voltage and bearing currents are needed. In addition, further investigation into alternative brush concepts such as the one presented in [27] for the possible use in Azipod systems. The alternative solution could be promising as it has very low friction and negligible wear. Furthermore, they are robust against contamination and are especially suitable for use with high-frequency currents and voltages.

- The capacitance of the bearing shield is calculated analytically and thus involves several approximations. Better analysis on the carrying/conducting areas should be carried out, for example, in the NX 3D-model at ABB Marine research and development department. This will give more accurate values for the capacitance.

- Possible paths for the currents in the whole drive system should be studied. Different components can be added to the Azipod model developed in this work. This is a very demanding task and is recommended for PhD level. Figure 48 shows a simplified sketch of possible paths for the currents and it can be used as a reference or starting point for the future work.

- Roller bearing capacitances are calculated with fixed load, fixed film thickness and fixed bearing temperature. These parameters vary with speed, forces on rotor and load, etc. Studies should be done for different parameters to get more simulations on various modes of operations. In addition, one should try to find bearing capacitance with different methods or by measurement and comparing it with the values obtained in this study.

- The capacitance between two windings is achieved by measurement. It is realized by connecting one probe to the first phase U_1 of the first winding and the other probe to the first phase U_2 of the second winding. An alternative method to extract this capacitance is to connect phases U_1, V_1 and W_1 together as well as U_2, V_2 and W_2, and then measure the capacitance between the windings in the same way as the original method. In case each method gives completely different values, the correctness of methods should be studied and the effect of different mutual capacitances in the simulations of bearing currents and voltages.

- Simulations with longer time should be carried out. This might lead to higher voltage and current peaks than obtained in this work. This could be done as a special assignment or Bachelor's thesis.

- A study of the possibility of adding cost-effective common-mode filters on the output of the drive is possible.

Throughout the work, the models and the calculations were done as precisely as possible in the limits of moderation and current knowledge. However, below is the list of assumptions that were used in this work. The assumptions used might have some effects on the result that were not taken into consideration or were taken very little. Many of these assumptions were noted where they were presented, however it is convenient to show them in clear bullet points. The list of assumptions:

- While creating the high-frequency model with capacitances, some capacitances with assumed minor effects were left out from the model. These capacitances are phase-to-phase capacitance and the capacitive coupling from the stator overhang to the rotor.
- It is assumed that there are no magnetic asymmetries in the motor construction.
- Assumptions used while analytically calculating capacitances C_{wr} and C_{rs}. For the assumptions please refer to subsection 5.2. These assumptions are such as permittivity of the insulation material of windings or the methods used to calculate the capacitance.
- Assumptions used while calculating the geometry and then the capacitances of the bearings. Without assumptions, analytically it would be almost impossible to find out the bearings' capacitances and methods such as finite element should be applied. However, using finite element method is very theoretical and involves also many assumptions itself.
- The bearing shield insulation consists of several parts and is challenging geometrically. Thus, several dimensional assumptions were used to determine the conducting areas.
- Sensors, oil pumps, bolts and all the other outfitting items in the thrust bearing system are perfectly insulated which means no leakage is assumed to happen from these parts. In reality, some of these could be conducting and thus cause disturbance in the system. In addition, the level of the disturbance is unknown.

9 Summary

The work presented in this thesis involved the creation of a high-frequency model in order to evaluate the bearing currents and voltages in the Azipod system. The approach was to implement an induction motor model, previously used for other research, in the Azipod environment. This method turned out to be adequate, giving promising results for analyzing bearing currents and voltages. The use of the developed high-frequency model enabled us to find the optimized combination of the bearing shield insulation and the brushes.

The parameters for the high-frequency model were either calculated analytically or measured. Simulations were carried out in order to acquire bearing voltages and currents. The interdependence of different components of the system was studied with the help of the simulations.

The results showed that without any protective measures, the bearings will be destroyed due to the high bearing voltages. Other useful findings showed that thrust side brushes can be taken off if the existing insulation is present, or if the thrust side brushes are present then the existing bearing shield insulation can be weakened. In addition, it was found that if there were no insulation at all, the bearing voltages and currents reached dangerous levels, even though the brushes worked normally.

Furthermore, with the aim of improving the Azipod model accuracy and broadening the knowledge of the problematic phenomenon, the thesis comprehensively suggests topics that require further investigation. These include bearing current measurements on sailing vessels and investigating the effect of the excitation machine on the bearing current phenomenon.

Suppliers of bearing shield insulation, brushes and bearings were interviewed in order to give ideas and feedbacks on the existing protective systems of the thrust bearing assembly. Finally, the interrogations indicated that no bearing supplier had requested an embedded electrical insulation solution for the Azipod technology.

References

[1] P. Pellinen, "Laakereiden kunnonvalvontamenetelmät ruoripotkurilaitteissa," Master's thesis, Teknillinen korkeakoulu, 2007.

[2] J. M. Erdman, R. J. Kerkman, D. W. Schlegel, and G. L. Skibinski, "Effect of PWM inverters on AC motor bearing currents and shaft voltages," *IEEE transactions on Industry Applications*, vol. 32, no. 2, pp. 250–259, 1996.

[3] S. Chen and T. A. Lipo, "Circulating type motor bearing current in inverter drives," *IEEE Industry Applications Magazine*, vol. 4, no. 1, pp. 32–38, 1998.

[4] A. Muetze, "Bearing currents in inverter-fed AC-motors," Ph.D. dissertation, Darmstadt University of Technology, 2004.

[5] P. Mäki-Ontto, "Modeling and reduction of shaft voltages in AC motors fed by frequency converters," Ph.D. dissertation, Helsinki University of Technology, 2006.

[6] *ACS6000 user manual*, ABB Medium Voltage Drives, 2016.

[7] D. W. Novotny, T. A. Lipo, and T. M. Jahns, *Introduction to electric machines and drives*. Wisconsin power electronics research center, 2009.

[8] S. Chen, T. A. Lipo, and D. Fitzgerald, "Modeling of motor bearing currents in PWM inverter drives," *IEEE Transactions on Industry Applications*, vol. 32, no. 6, pp. 1365–1370, 1996.

[9] M. Cacciato, A. Consoli, L. Finocchiaro, and A. Testa, "High frequency modeling of bearing currents and shaft voltage on electrical motors," in *2005 International Conference on Electrical Machines and Systems*, vol. 3. IEEE, 2005, pp. 2065–2070.

[10] A. M. Trzynadlowski, *Introduction to Modern Power Electronics*, 3rd ed. Wiley, 2016.

[11] *Product introduction*, ABB Marine, 2012.

[12] H. Toliyat and G. Kliman, *Handbook of Electric Motors*, 2nd ed. CRC, 2004.

[13] R. Schiferl, M. Melfi, and J. Wang, "Inverter driven induction motor bearing current solutions," in *Petroleum and Chemical Industry Conference, 2002. Industry Applications Society 49th Annual*. IEEE, 2002, pp. 67–75.

[14] D. Dahl, D. Sosnowski, D. Schlegel, R. J. Kerkman, and M. Pennings, "Gear up your bearings," *IEEE Industry Applications Magazine*, vol. 14, no. 4, pp. 45–53, 2008.

[15] H. E. Boyanton and G. Hodges, "Bearing fluting [motors]," *IEEE industry applications magazine*, vol. 8, no. 5, pp. 53–57, 2002.

[16] D. Busse, J. Erdman, R. Kerkman, D. Schlegel, and G. Skibinski, "Characteristics of shaft voltage and bearing currents," *IEEE Industry Applications Magazine*, vol. 3, no. 6, pp. 21–32, 1997.

[17] S. Ogasawara, H. Ayano, and H. Akagi, "Measurement and reduction of EMI radiated by a PWM inverter-fed AC motor drive system," *IEEE Transactions on Industry Applications*, vol. 33, no. 4, pp. 1019–1026, 1997.

[18] M. J. Costello, "Shaft voltages and rotating machinery," *IEEE Transactions on Industry Applications*, vol. 29, no. 2, pp. 419–426, 1993.

[19] C. Ammann, K. Reichert, R. Joho, and Z. Posedel, "Shaft voltages in generators with static excitation systems-problems and solution," *IEEE Transactions on Energy Conversion*, vol. 3, no. 2, pp. 409–419, 1988.

[20] P. J. Link, "Minimizing electric bearing currents in adjustable speed drive systems," in *Pulp and Paper Industry Technical Conference, 1998. Conference Record of 1998 Annual.* IEEE, 1998, pp. 181–195.

[21] A. Muetze and A. Binder, "Practical rules for assessment of inverter-induced bearing currents in inverter-fed AC motors up to 500 kW," *IEEE Transactions on Industrial Electronics*, vol. 54, no. 3, pp. 1614–1622, 2007.

[22] A. Binder and A. Muetze, "Techniques for measurement of parameters related to inverter-induced bearing currents," *IEEE Transactions on Industry Applications*, vol. 43, no. 5, pp. 1274–1283, 2005.

[23] P. Maki-Ontto and J. Luomi, "Induction motor model for the analysis of capacitive and induced shaft voltages," in *IEEE International Conference on Electric Machines and Drives, 2005.* IEEE, 2005, pp. 1653–1660.

[24] F. J. Ferreira, J. P. Trovão, and A. T. de Almeida, "Motor bearings and insulation system condition diagnosis by means of common-mode currents and shaft-ground voltage correlation," in *Electrical Machines, 2008. ICEM 2008. 18th International Conference on.* IEEE, 2008, pp. 1–6.

[25] "Bearing currents in modern AC drive sytems," ABB Drives, 2011, Technical guide No. 5.

[26] A. Binder and A. Muetze, "Scaling effects of inverter-induced bearing currents in AC machines," *IEEE Transactions on Industry Applications*, vol. 44, no. 3, pp. 769–776, 2008.

[27] A. Muetze and H. W. Oh, "Design aspects of conductive microfiber rings for shaft-grounding purposes," *IEEE Transactions on Industry Applications*, vol. 44, no. 6, pp. 1749–1757, 2008.

[28] D. Busse, J. Erdman, R. J. Kerkman, D. Schlegel, and G. Skibinski, "System electrical parameters and their effects on bearing currents," *IEEE Transactions on Industry Applications*, vol. 33, no. 2, pp. 577–584, 1997.

[29] O. Magdun and A. Binder, "Calculation of roller and ball bearing capacitances and prediction of EDM currents," in *Industrial Electronics, 2009. IECON'09. 35th Annual Conference of IEEE*. IEEE, 2009, pp. 1051–1056.

[30] A. Binder and O. Magdun, "High-frequency induction machine modeling for common mode current and bearing voltage calculation," *IEEE Transactions on Industry Applications*, vol. 50, no. 3, pp. 1780–1790, 2014.

[31] A. Boglietti, A. Cavagnino, and M. Lazzari, "Experimental high-frequency parameter identification of AC electrical motors," *IEEE Transactions on Industry Applications*, vol. 43, no. 1, pp. 23–29, 2007.

[32] M. Schinkel, S. Weber, S. Guttowski, W. John, and H. Reichl, "Efficient HF modeling and model parameterization of induction machines for time and frequency domain simulations," in *Applied Power Electronics Conference and Exposition, 2006. APEC'06. Twenty-First Annual IEEE*. IEEE, 2006, pp. 6–pp.

[33] A. Muetze and A. Binder, "Calculation of motor capacitances for prediction of the voltage across the bearings in machines of inverter-based drive systems," *IEEE Transactions on Industry Applications*, vol. 43, no. 3, pp. 665–672, 2007.

[34] L. Aura and A. J. Tonteri, *Teoreettinen sähkötekniikka ja sähkökoneiden perusteet*, 6th ed. WSOY, 2004.

[35] I. Lindell and A. Sihvola, *Sähkömagneettinen kenttäteoria 1.* Otatieto, 2002.

[36] O. Magdun, Y. Gemeinder, and A. Binder, "Prevention of harmful EDM currents in inverter-fed AC machines by use of electrostatic shields in the stator winding overhang," in *IECON 2010-36th Annual Conference on IEEE Industrial Electronics Society*. IEEE, 2010, pp. 962–967.

A Detailed pictures of impedance measurements

It is important to show how the measurements were carried out. Pictures from A1 to A12 illustrate the common-mode and differential-mode measurements as well as the open circuit and short circuit compensations for the both windings. Moreover, in the last three pictures are shown the mutual winding measurements.

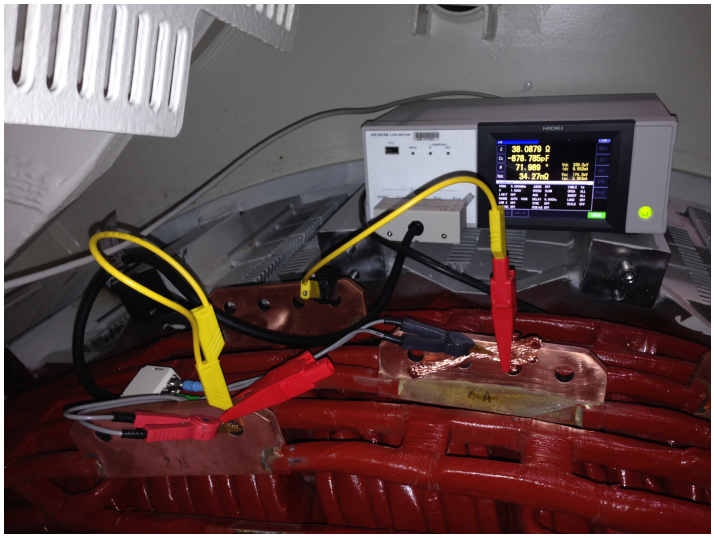

Figure A1: Winding one, common-mode measurement.

Figure A2: Winding one, common-mode open circuit compensation.

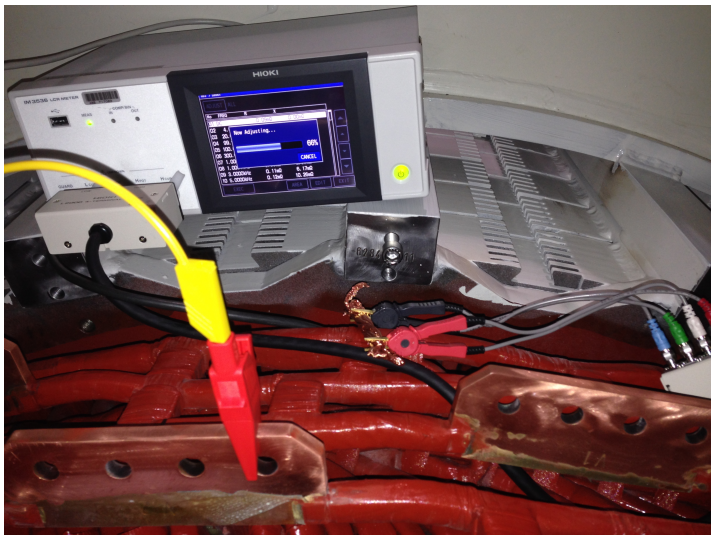

Figure A3: Winding one, common-mode short circuit compensation.

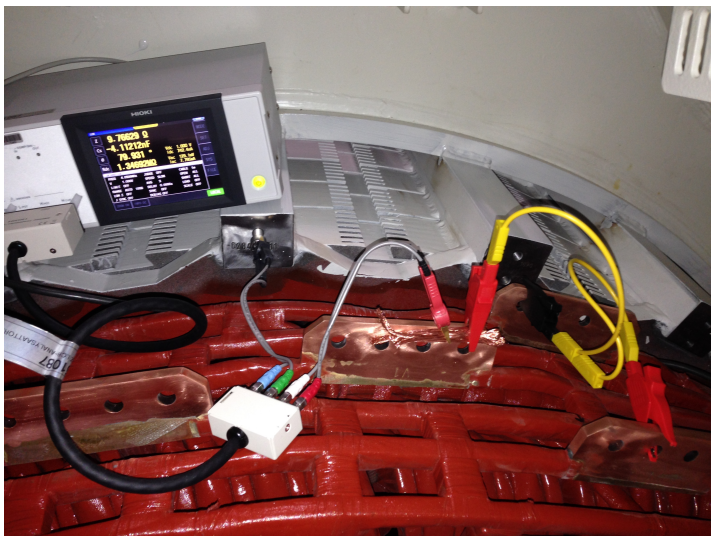

Figure A4: Winding two, common-mode measurement.

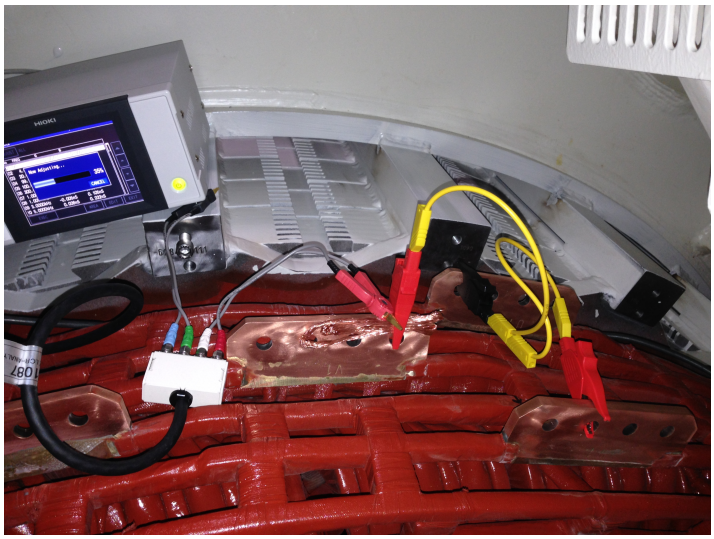

Figure A5: Winding two, open circuit compensation.

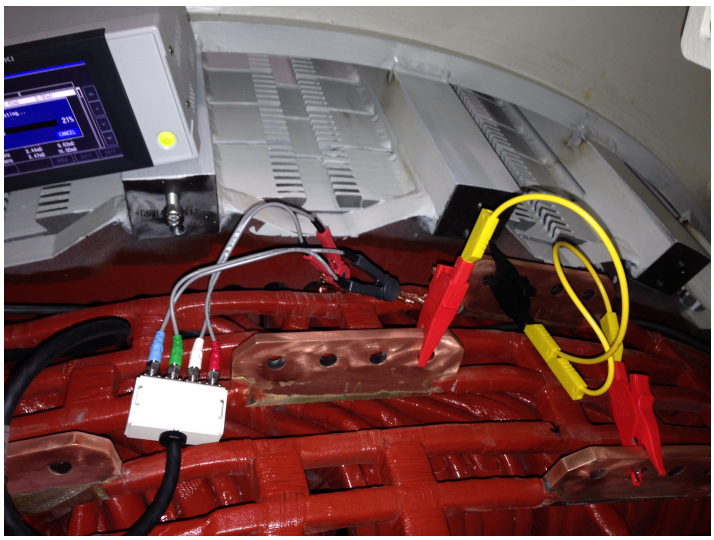

Figure A6: Winding two, common-mode short circuit compensation.

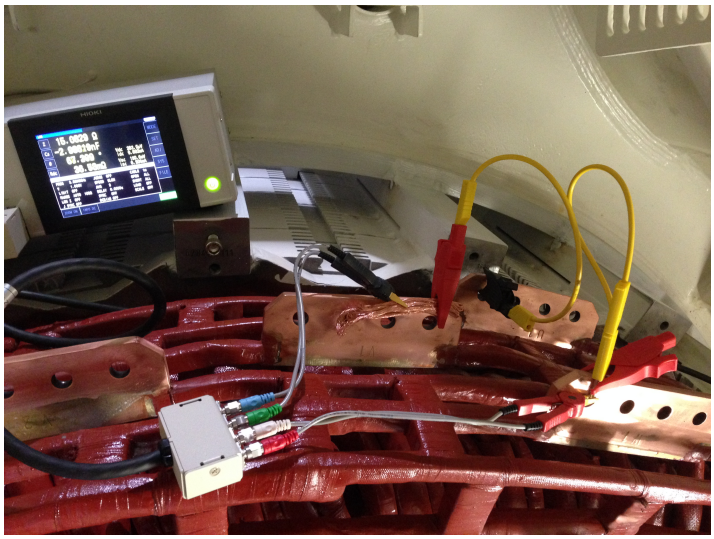

Figure A7: Winding two, differential-mode measurement.

Figure A8: Winding two, differential-mode open circuit compensation.

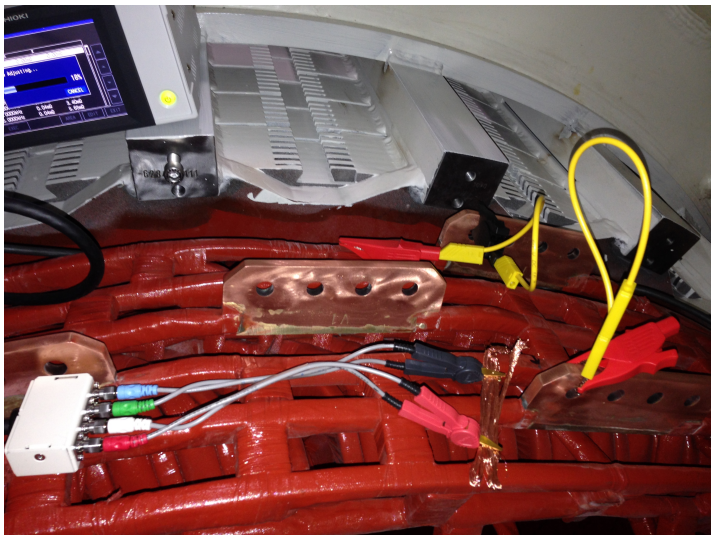

Figure A9: Winding two, differential-mode short circuit compensation.

Figure A10: Mutual winding measurement.

Figure A11: Mutual winding open circuit compensation.

Figure A12: Mutual winding short circuit compensation.

B Shaft grounding testing

The manufacturer of the earthing devices is Helwig Carbon Products. Due to our demand, high-frequency electrical tests for the brushes were carried out in their factory in Wisconsin. The test setup is shown in Figure B1.

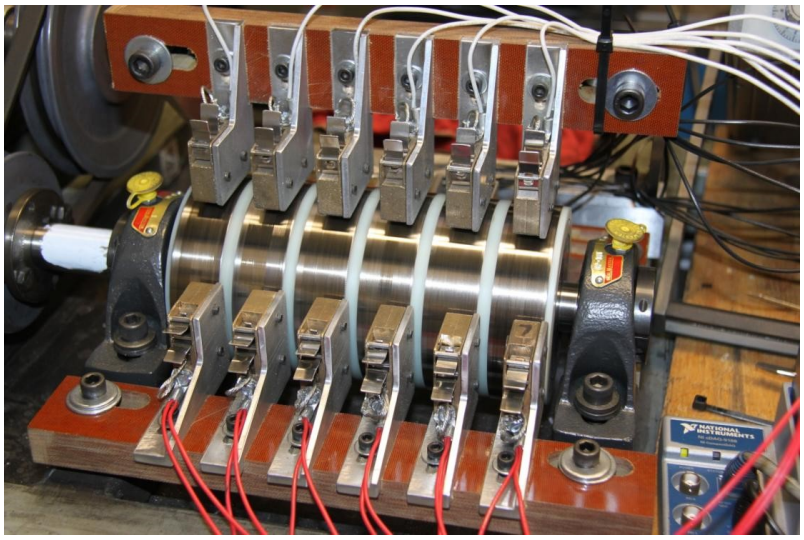

Figure B1: Shaft grounding test setup.

The brush holder was manufacturer's standard shaft grounding BPK-4, with 9.5×6.3 contact area, and 230 g constant spring force. The 100 mm steel shaft was rotated at various speeds up to 4000 RPM, and there were no significant differences in the results. A frequency generator was used to apply the low power at the varying frequencies on each of the brush grades. Figures B2 and B3 are graphs for the grade K106 (85 % copper graphite) and grade K017 (50 % silver graphite) brushes. Both graphs have difference in resistance scale. The graphs are linear with the change of frequencies, which means that the nature of the contact seems to be resistive regardless of currents and frequencies within the limits of the test. Due to these tests, resistance values for the brushes are $R_1 = R_2 = 1\ \Omega$. These values are applied in the model.

The grade type K106 is the one currently used in the Azipod propulsion systems. Additional information from the supplier regarding the tests were received. They say that one of their customers had field tested their shaft grounding system at higher frequencies. They found that their larger 20×10 mm holder maintained lower shaft voltage at high frequency than their standard 9.5×6.3 holder. For the Azipod propulsions, adding larger holders should be an advantage at high frequencies. This important observation is added in the future suggestions section.

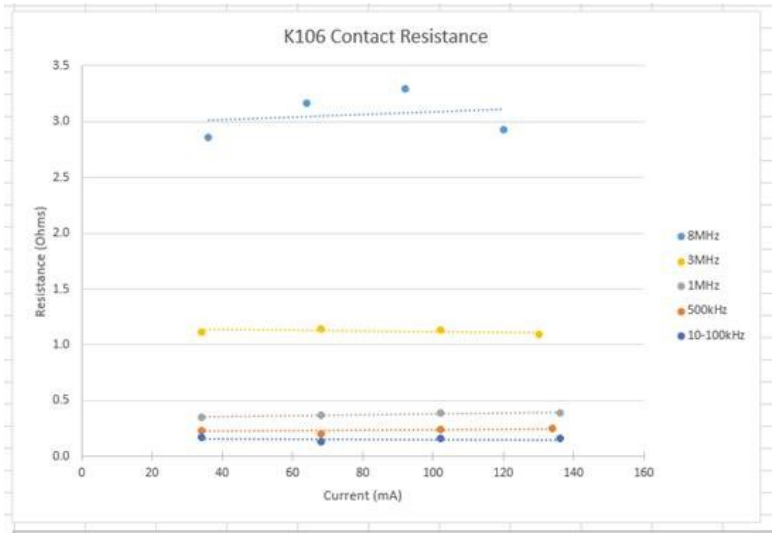

Figure B2: Contact resistance characteristic of K106 with different frequencies.

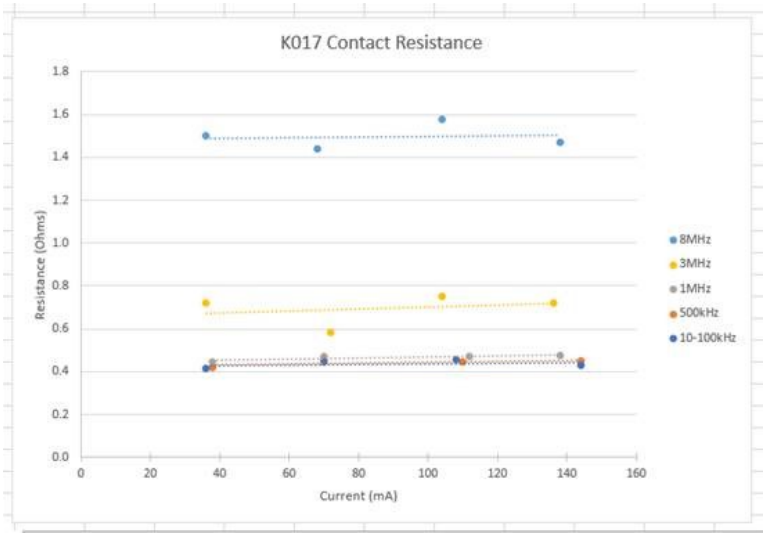

Figure B3: Contact resistance characteristic of K017 with different frequencies.

C Common-mode and differential-mode measurements of an induction motor

Here are shown the impedance response curves of a 1400 kW induction motor AMI 560L8A. Measurements were carried out at ABB Pitäjänmäki factory.

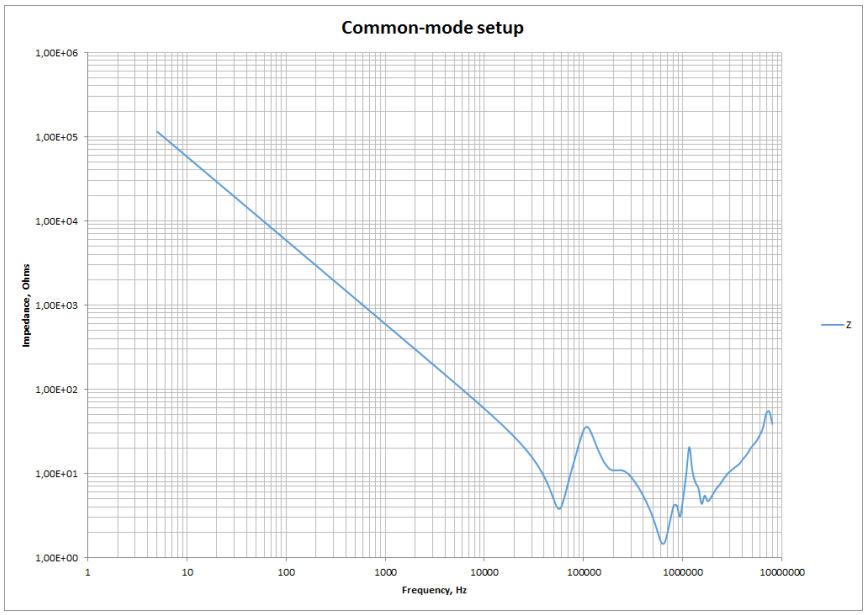

Figure C1: Common-mode measurement of AMI 560L8A.

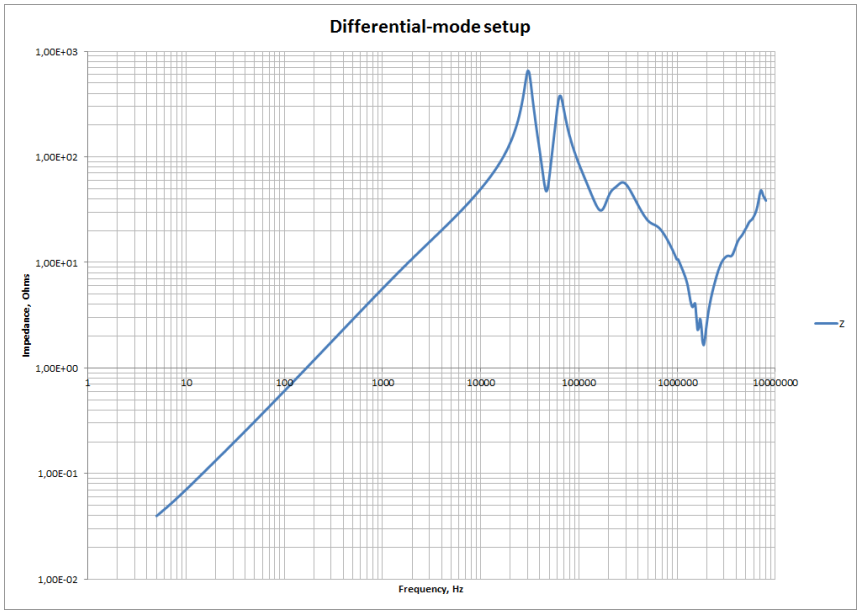

Figure C2: Differential-mode measurement of AMI 560L8A.

D Simulation results

First inputs

In each case, the first picture is bearing voltage, the second is bearing current over the radial bearing and the third picture is bearing current over the slide thrust bearing. To illustrate the scale, each picture has orange boxes with the value next to it. However, this value is not the maximum or minimum in all cases.

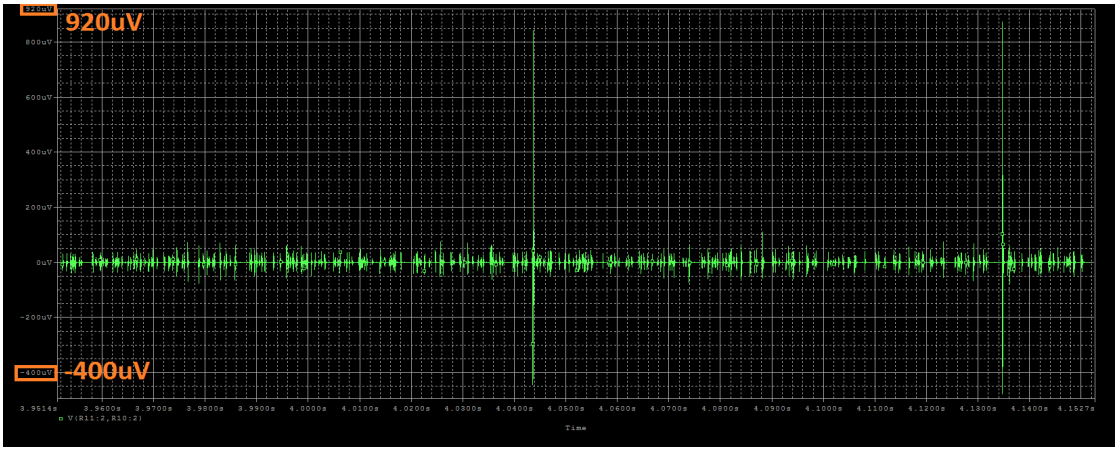

Figure D1: Case 1: Absolute maximum voltage around 900 µV.

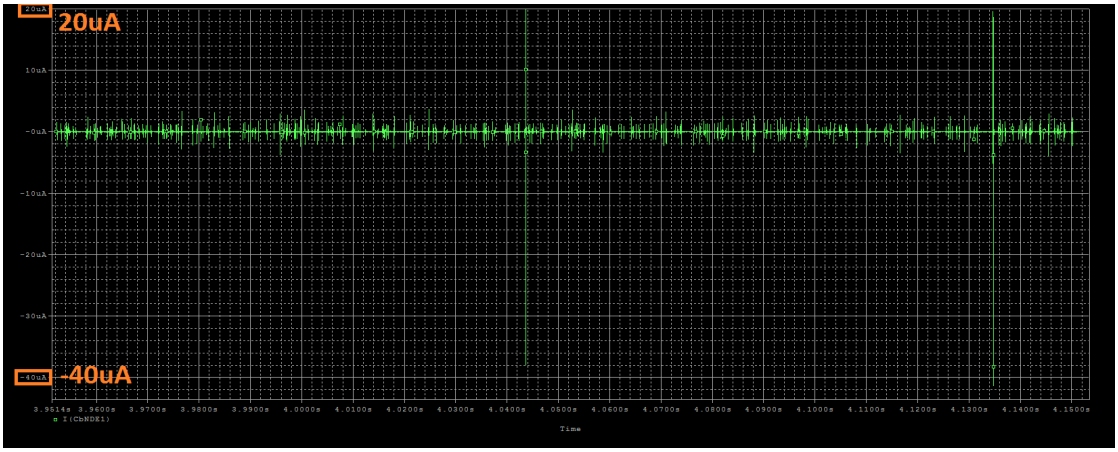

Figure D2: Case 1: Absolute maximum current around 40 µA.

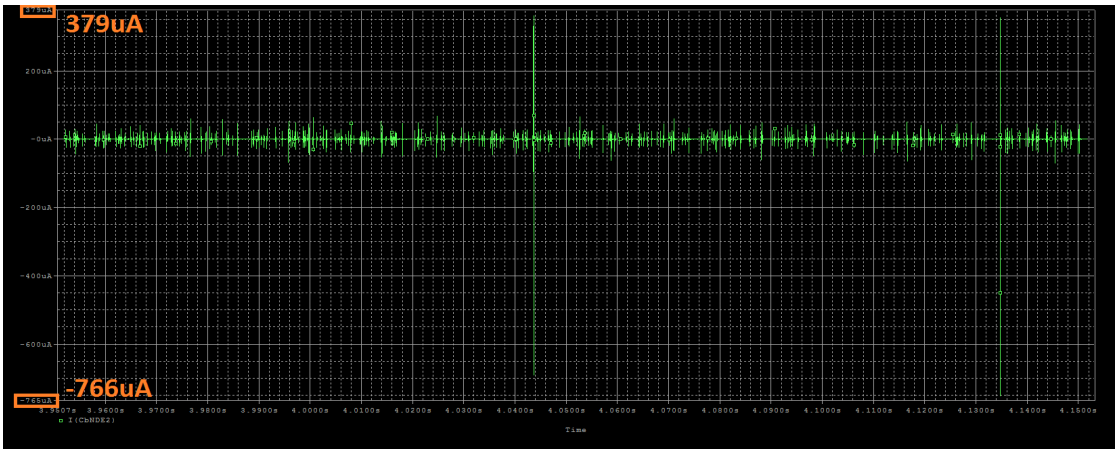

Figure D3: Case 1: Absolute maximum current around 766 µA.

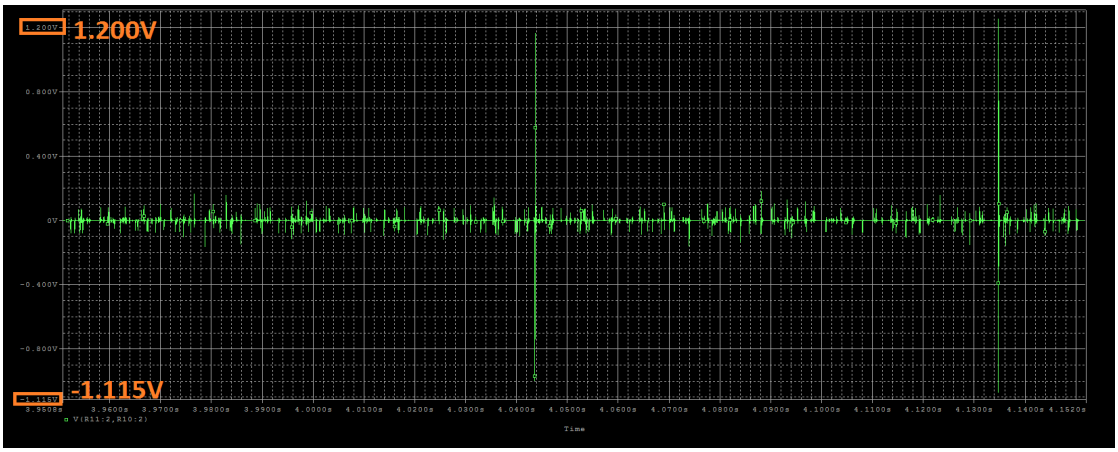

Figure D4: Case 2: Absolute maximum voltage around 1.25 V.

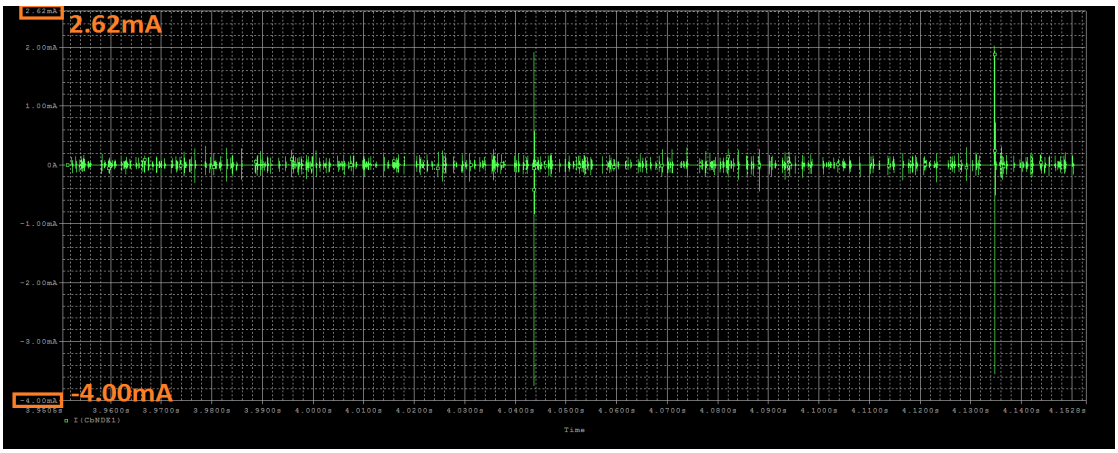

Figure D5: Case 2: Absolute maximum current around 4 mA.

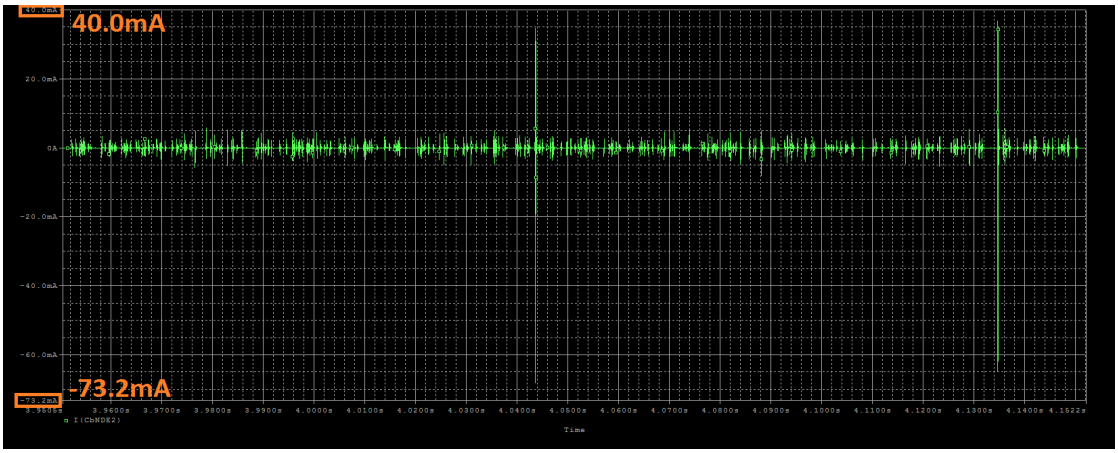

Figure D6: Case 2: Absolute maximum current around 70 mA.

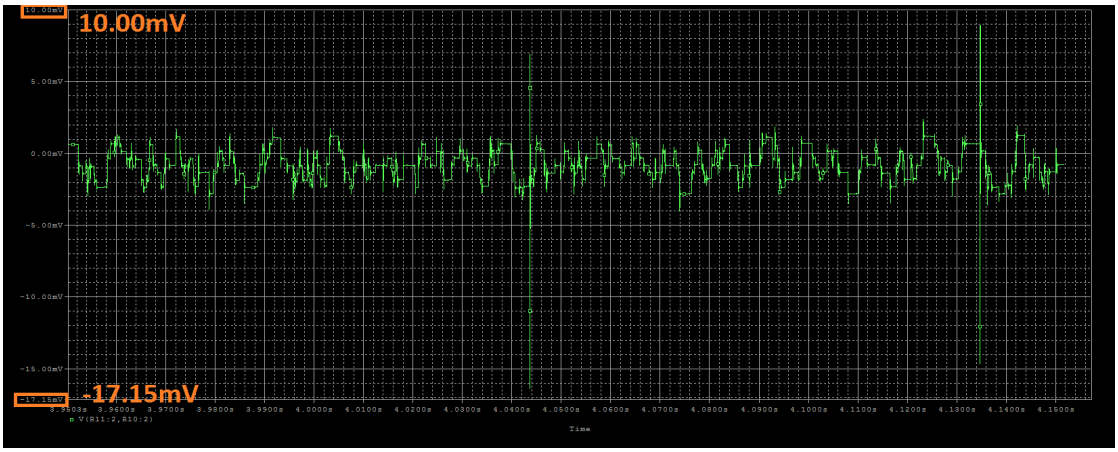

Figure D7: Case 3: Absolute maximum voltage around 16 mV.

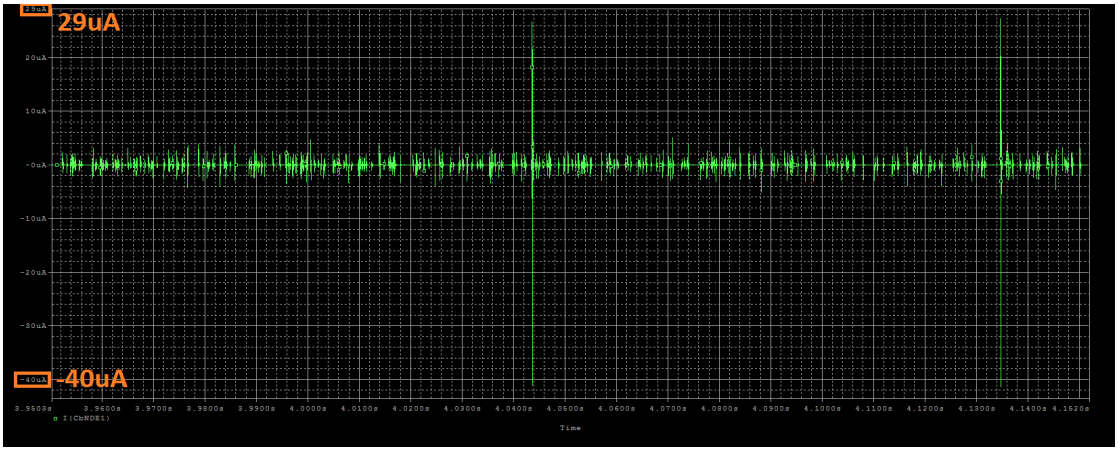

Figure D8: Case 3: Absolute maximum current around 40 µA.

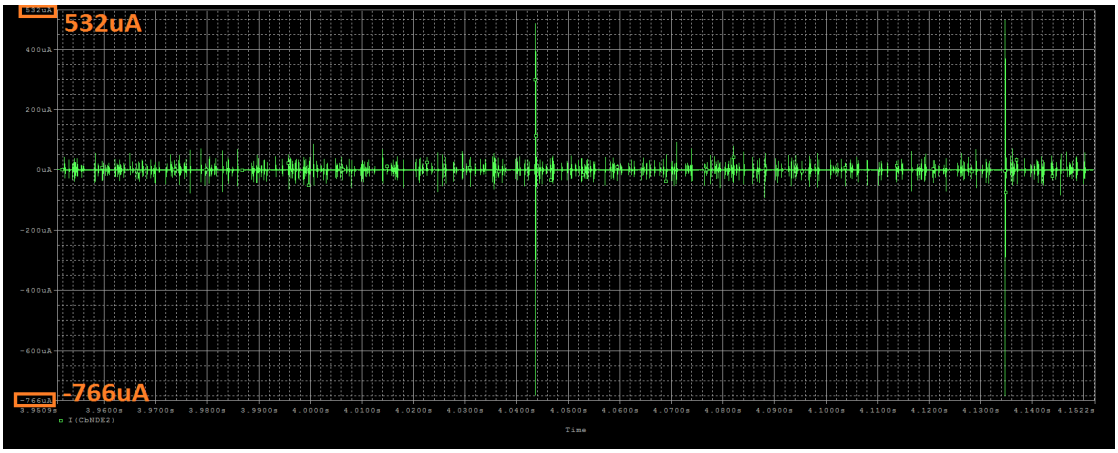

Figure D9: Case 3: Absolute maximum current around 766 µA.

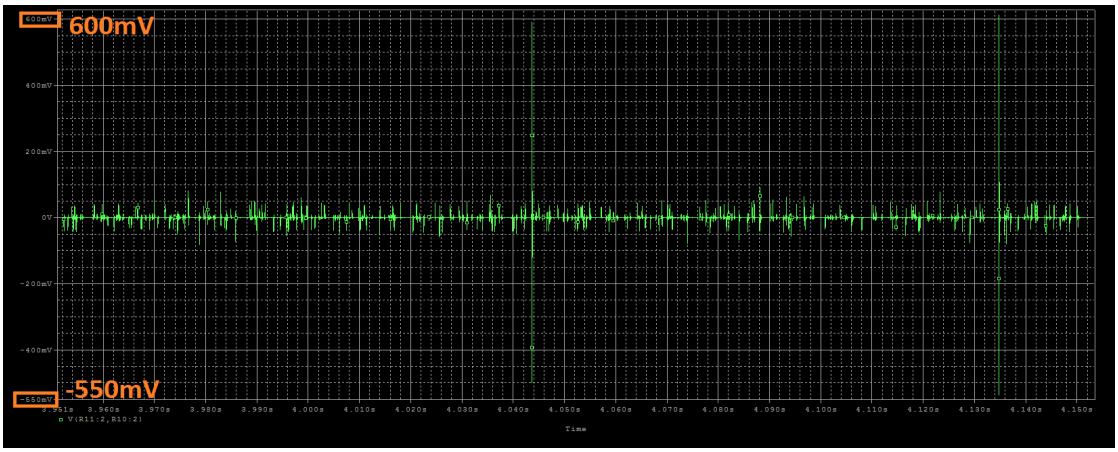

Figure D10: Case 4: Absolute maximum voltage around 600 mV.

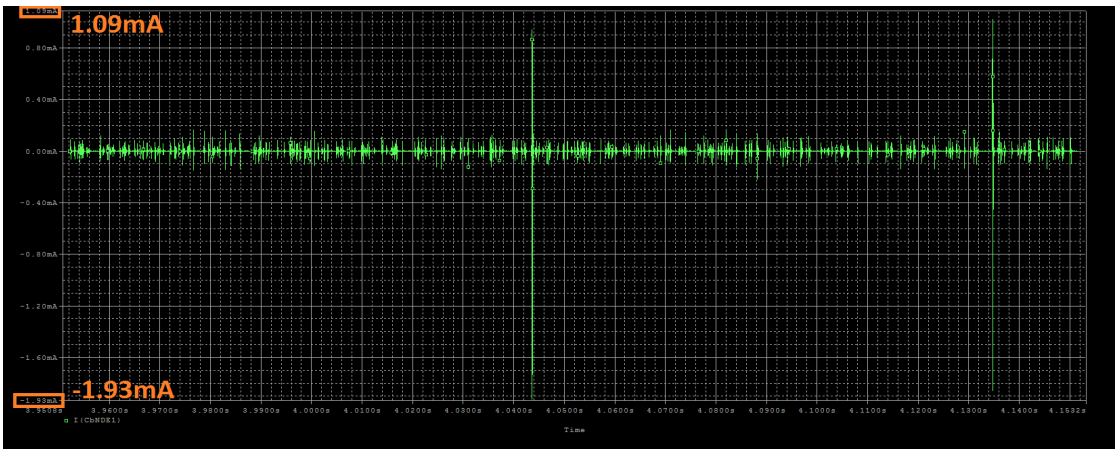

Figure D11: Case 4: Absolute maximum current around 1.93 mA.

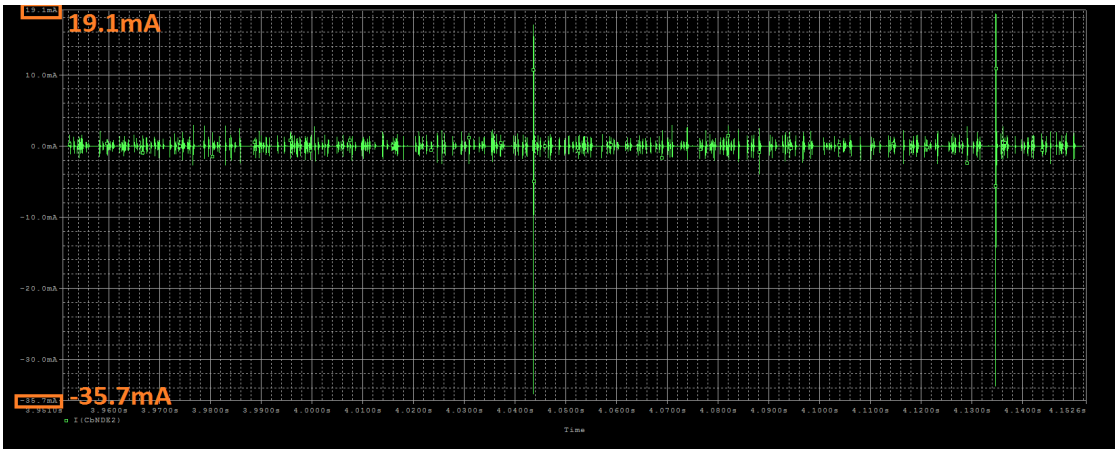

Figure D12: Case 4: Absolute maximum current around 36 mA.

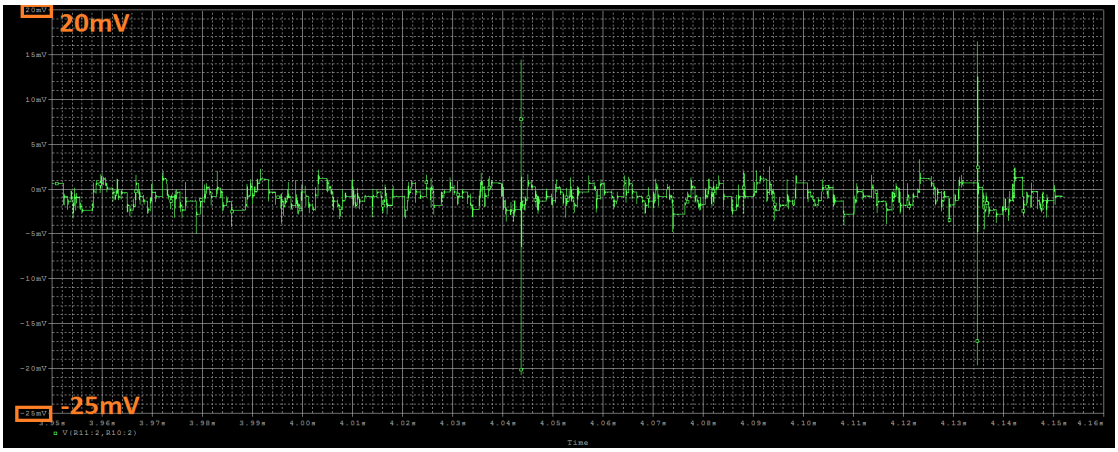

Figure D13: Case 5: Absolute maximum voltage around 20 mV.

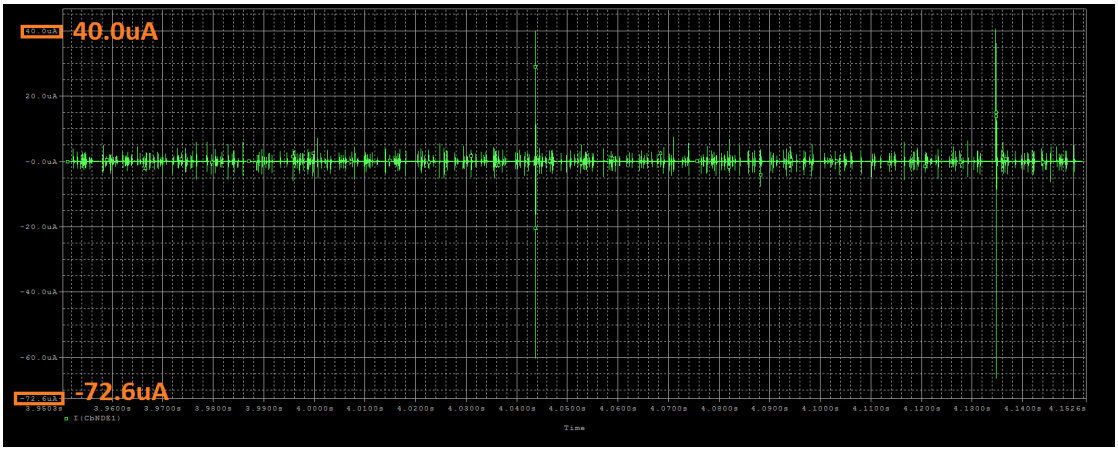

Figure D14: Case 5: Absolute maximum current around 70 µA.

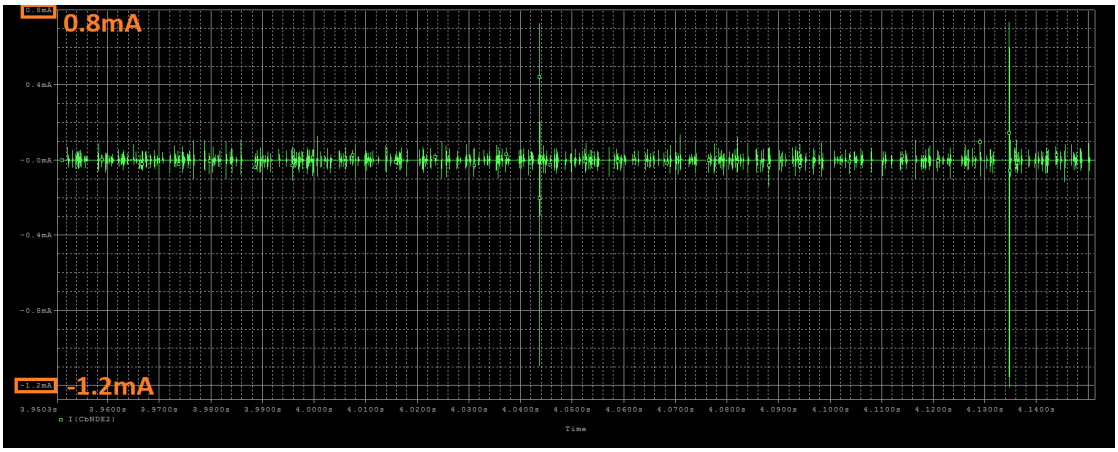

Figure D15: Case 5: Absolute maximum current around 1.2 mA.

Second inputs

Although all cases were simulated, here is shown only case 1. This is because the values are slightly lower than the ones in the first input and thus these simulations will not provide any extra value to the work.

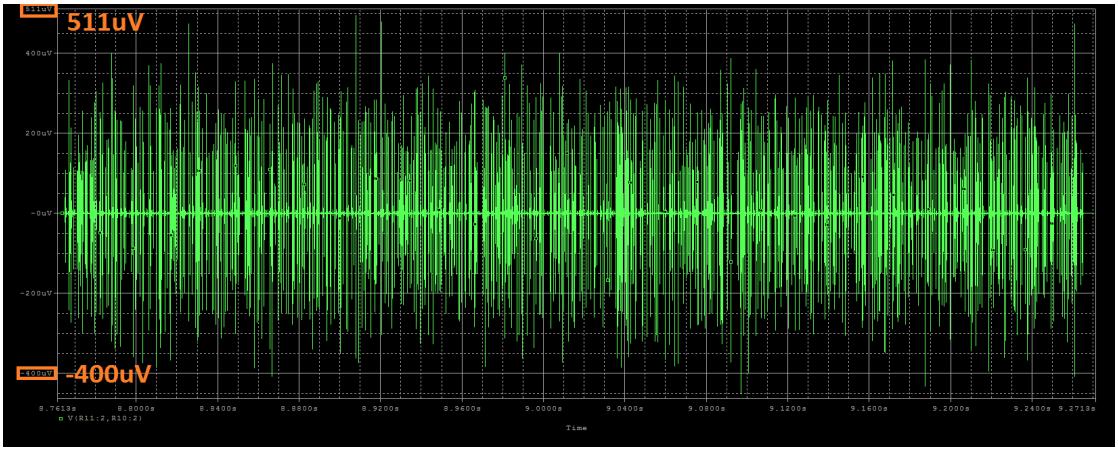

Figure D16: Case 1: Absolute maximum voltage around 511 µV.

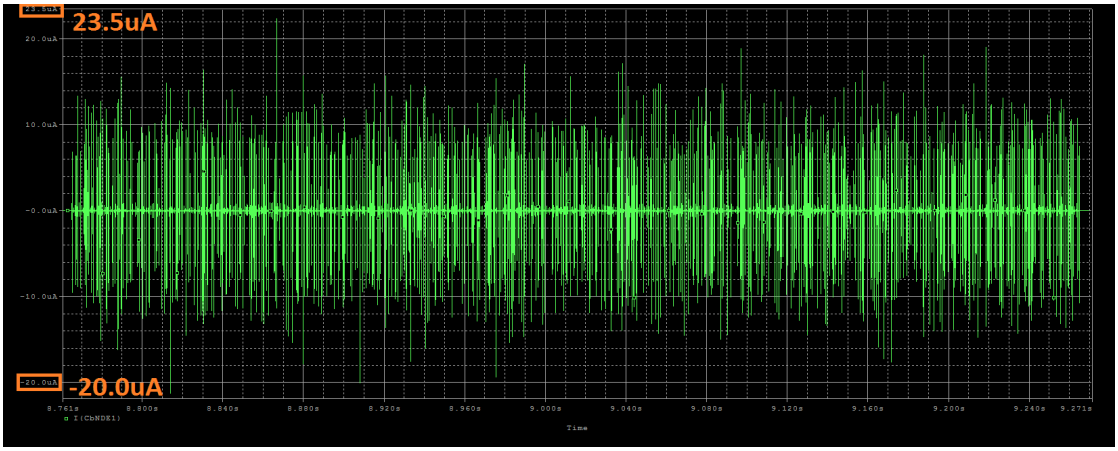

Figure D17: Case 1: Absolute maximum current around 21 µA.

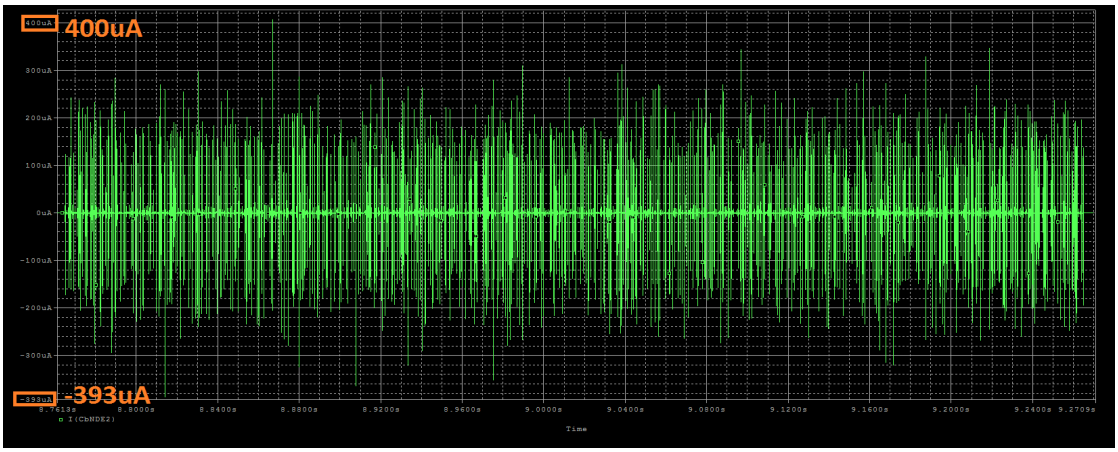

Figure D18: Case 1: Absolute maximum current around 393 µA.